Additively Manufactured Electronic Devices and Antennas for Microwave and Millimeter-Wave 5G Applications

By Mengze Li

Thesis submitted in fulfilment of the requirements for the degree of Doctor of Philosophy

under the supervision of
Principal Supervisor: A/Prof. Yang Yang
Co-Supervisor: Prof. Francesca Iacopi

University of Technology Sydney
Faculty of Engineering and Information Technology

March 2023

CERTIFICATE OF ORIGINAL AUTHORSHIP

I, Mengze Li declare that this thesis, is submitted in fulfilment of the requirements award of the Doctoral Degree, in the School of Electrical and Data Engineering, Faculty of Engineering and Information Technology at the University of Technology Sydney.

This thesis is wholly my own work unless otherwise referenced or acknowledged. In addition, I certify that all information sources and literature used are indicated in the thesis.

I certify that the work in this thesis has not previously been submitted for a degree nor has it been submitted as part of the requirements for a degree at any other academic institution except as fully acknowledged within the text.

This research is supported by the Australian Government Research Training Program. It is also supported by Nano Dimension under a Ph.D. scholarship agreement.

Signature: Production Note:
Signature removed prior to publication.

Date: 15/03/2023

Acknowledgement

Throughout the writing of this dissertation and my PhD studies in Sydney, Australia, I have received a great deal of support and assistance. I'm so glad to indicate my gratitude to everyone here.

I would first like to express my sincere thanks to my funding body, Nano Dimension, for supporting me with a PhD scholarship agreement.

I would particularly like to thank my supervisor, Yang Yang, for offering valuable guidance throughout my studies. You provided me with the opportunities that I needed to choose the right direction and successfully complete my dissertation. I am thankful for your guidance at all stages of my research at UTS both at the academic and personal level.

I would also like to express my warmest gratitude to my co-supervisor, Prof. Francesca Iacopi, for her support and guidance in my academic research. I am also grateful to Prof. Iacopi for her help in polishing my papers and improving my writing skills.

I would like to thank the R&D team at Nano Dimension (Israel, Hong Kong, and the U.S.A.) for the technical support provided. Special thanks to Dr. Jaim Nulman for his strong advice and to Mr. Minoru Yamada and Joseph Samuya for their technical advice during prototyping and fabrication. I would also like to thank the UTS ProtoSpace for help with the relevant devices.

I would like to thank my group members, Jianfeng Zhu, Jinxu Xu, Ting Zhang, Zongqi Cai, Jiexin Lai and Jingyu Lin, who generated stimulating discussions as well as happy distractions to rest my mind away from my research when it was most needed.

I would also like to thank Prof. Li Deng and Miss Xiaoyuan He from Beijing University of Posts and Communications (BUPT) and for their full support for my research career pathway.

Finally, I would like to thank my parents and family members for their everlasting love, patience, and help in my studies.

Published and Under Review Papers Related to this Thesis:

[P1] **M. Li,** Y. Yang, "Multi-material additive manufacturing - a further step from microwave to terahertz regime," *IEEE Microwave Magazine*, vol. 24, no. 1, pp. 30-45, Jan. 2023. **[Chapter 2, Section 2.3]**

[P2] **M. Li,** Y. Yang, F. Iacopi, J. Nulman and S. Chappel-Ram, "3D-printed low-profile single-substrate multi-metal layer antennas and array with bandwidth enhancement," *IEEE Access,* vol. 8, pp. 217370-217379, 2020. doi: 10.1109/ACCESS.2020.3041232. **[Chapter 3, Section 3.2]**

[P3] **M. Li**, Y. Yang, F. Iacopi, M. Yamada and J. Nulman, "Compact multilayer bandpass filter using low-temperature additive manufacturing solution," *IEEE Transactions on Electron Devices,* vol. 68, no. 7, pp. 3163-3169, July 2021. doi: 10.1109/TED. 2021.3072926 (Published as journal front cover artwork) **[Chapter 4, Section 4.2]**

[P4] **M. Li,** Y. Yang, F. Iacopi, M. Yamada, Y. Zhang, and J. Nulman, "Vertically integrated multi-layer composite right/ left-handed broadband devices using additively manufactured electronics solution," *IEEE Transactions on Microwave Theory and Techniques,* in submission. **[Chapter 4, Section 4.3]**

[P5] **M. Li,** Y. Yang, L. Deng, X. He, F. Iacopi and J. Nulman, "3D printed multi-material conductive and dielectric metasurfaces for independent manipulation of broadband orbital angular momentum," *ACS Applied Materials & Interfaces,* in submission. **[Chapter 5]**

Abstract

Additive manufacturing (AM) technology has been changing our daily lives. As one of the fundamental manufacturing methods in what is known as the Industry 4.0 concept, AM technology is now a driving force for revolutionary manufacturing microwave components with high-performance, high-accuracy, low-cost, and short production cycles. The materials utilized in additive manufacturing have been developed from single-dielectric/metal-only materials to multi-material printing (dielectric and conductive materials), extending the possibility of AM-inspired designs from microwave to terahertz regime. An overview from single-material to multi-material AM printing systems and their applications in microwave, millimeter-wave and terahertz designs are presented.

This thesis focuses on designing electronic devices and antennas for 5G applications based on additive manufacturing technology. In this research, electrical characteristics of the dielectric materials used by the 3D printing machine, including its dielectric constant and loss tangent, are investigated and measured. Taking advantage of the AM technology, multi-layer devices, including transmission lines, antennas, bandpass filters, couplers, and reflectarrays, which perform well and have compact sizes, are proposed and fabricated for 5G applications. The main contents are as follows:

Chapter 1: Introduction to multi-material integrated additively manufactured electronics (AME) solution, which plays an essential role in the fabrication of the designs.

Chapter 2. Literature review from single material to multi-material additive manufacturing technology. This chapter introduces the development history of additive manufacturing technology. Relevant content has been published in the journal of *IEEE Microwave Magazine* [P1].

Chapter 3. 3D-printed low-profile single-substrate multi-metal layer devices with compact size. This chapter demonstrates additively manufactured low-profile single-substrate multi-metal layer antennas and array with an ultralow profile and broad operational band. Successfully devising multi-layer patch antennas proves that the AME solution can serve as a revolutionary approach to the increasing number of 5G

consumer mobile electronics. Related content has been published in the journal of *IEEE Access* [P2].

Chapter 4. 3D-printed compact transmission lines, and multi-layer bandpass filters. This chapter proposed a compact additively manufactured bandpass filter (BPF) with good out-of-band rejection. Related content has been published in *IEEE Transactions on Electron Devices* [P3]. Next, a novel compact vertically integrated multi-layer composite right/left-handed (CRLH) BPF with low loss and the wide operational band is proposed. Related content is being submitted to the journal of *IEEE Transactions on Microwave Theory and Techniques* [P4].

Chapter 5. 3D-printed metasurfaces for independent manipulation of broadband orbital angular momentum. This chapter demonstrates a 3D-printed metasurface generating orbital angular momentum (OAM) states with different topological charges at two operational broadbands for high-information capacity and high-security applications. Related content has been submitted to the journal of *ACS Applied Materials & Interfaces* [P5].

Chapter 6. Conclusion

Keywords: Additively manufactured electronics, 3D printing, Millimeter-wave, Microwave, Antennas, Antenna array, Reflectarray, Bandpass filter, Coupler, Composite right/ left-handed structures.

Contents

Chapter 1 Introduction

1.1 Research Background

The fifth generation (5G) is a technology that is already changing our lives. The 5G rollout strategy has become a driving force for revolutionary fabrication methods that can construct electronics with high accuracy, low cost, and a short production cycle.

5G wireless system is envisioned for 2020 to meet the higher data rate requests and a larger number of mobile phone users. 5G communication is expected to handle data rates up to multiple gigabits per second. To meet this need, most countries selected bands within the frequency range 26.5-29.5 GHz (28 GHz) for the early deployments of 5G. Millimeter-wave communication is also a wise choice. The millimeter-wave communication holds outstanding advantages, such as sufficient bandwidth, high transmission efficiency, and compact components for highly integrated systems. However, due to high oxygen absorption, millimeter-wave is not suitable for long-range communication. Sub-6GHz spectrum has been established as the key band for 5G services in the last decades. Efficient fabrication methods to prototype consumer electronics, operating at sub-6 GHz, become more and more important. Antennas, the most important component of a communication system, play a critical role in wireless data transmission, especially where the high-gain antenna helps to compensate for the free-space propagation loss and reduce the multipath effect. For many scenarios, those antennas with the properties of high gain, non-squint radiation patterns, and bandwidth are desired. Besides, to adapt the antenna to more industrial applications, additive manufacturing technology is needed to: firstly, downscale novel antenna array systems; secondly, equip more functions to realize further development of antenna design; and thirdly, enrich its application in some cutting-edge research areas. Examples are security scan systems in an airport and crewless vehicles using the millimeter-wave sensing system.

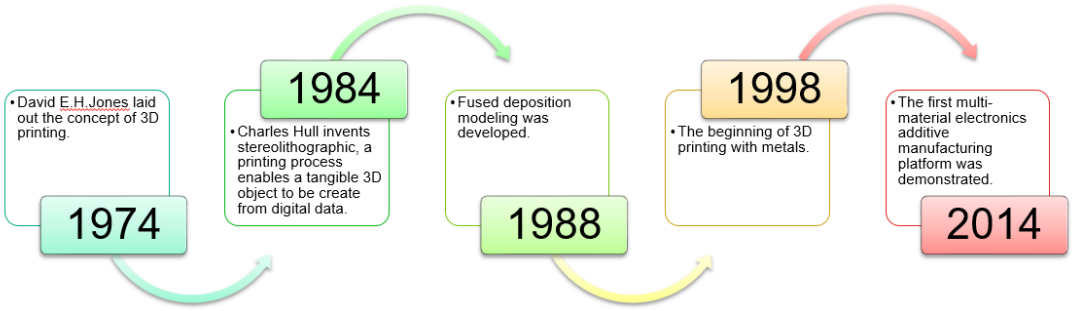

Fig. 1.1. Development history of additive manufacturing technology

Many complex constructions, which are difficult to implement by means of conventional methods, can be prototyped, and realized by additive manufacturing technology. Fig. 1.1 summarizes the history of additive manufacturing technology. In 1974, David E.H. Jones laid out the concept of additive manufacturing in his regular column called Ariadne in the journal *New Scientist* [1]. By 1984, Charles Hull, who went on to found 3D Systems, dubbed the process stereolithography, began to experiment with printing materials instead of ink. Stereolithographic is a printing process that enables a tangible 3D object to be created from digital data and plays an important role in the rise of additive manufacturing technology [2]. Then, fused deposition modeling was developed in 1988. It is still a major method widely applied in 3D printing facilities. 1998 marked the beginning of 3D printing with metals [3], which is a huge breakthrough in the history of additive manufacturing technology, especially in certain aspects of materials. In the 21st century, even multi-material electronics additive manufacturing platform is now demonstrated.

Fig. 1.2. Application of 3D printing technology in daily life.

As depicted in Fig. 1.2, 3D printing has been used in manufacturing, medical, food, clothing industries and various sociocultural sectors, which facilitates 3D printing becoming a successful commercial technology [4]. The earliest application of additive manufacturing was on the toolroom end of the manufacturing spectrum [5]. Furthermore, NASA is looking more at the technology to create 3D-printed food to limit food waste and can be designed to fit an astronaut's dietary needs [6]. Large varieties of foods are appropriate candidates, such as chocolate, candy, meat and flat foods such as crackers, pasta, and pizza [7-10]. In the 2010s, 3D printing technology entered production to a much greater extent. 3D printing has entered the world of clothing, with fashion designers experimenting with 3D-printed bikinis, shoes, and dresses. For instance, Nike uses 3D printing to prototype and manufacture the 2012 Vapor Laser Talon football shoe for players of American football, and New Balance is 3D manufacturing custom-fit shoes for athletes [11-12]. In cars, trucks, and aircraft,

additive manufacturing is beginning to transform both unibody and fuselage design and production and powertrain design and production [13-15]. In terms of firearms, in 2012, the US-based group Defence Distributed disclosed plans to design a working plastic 3D-printed firearm. This plan raised concerns regarding the effects that 3D printing may have on gun control effectiveness [16-18]. Virtual planning of surgery using 3D-printed personalized instruments have been applied to many areas of surgery, including rebuilding the face of a motorcyclist who had been seriously injured in a road accident [19] and printing a kidney transplant to save a three-year-old boy's life [20]. As well, 3D printing has been applied to the field of cultural heritage for preservation, restoration, and dissemination purposes [21]. The museum souvenirs manufactured by 3D printers are available in some shops, such as the Metropolitan Museum of Art and the British Museum [22-23].

1.2 Multi-Material Integrated Additively Manufactured Electronics

1.2.1 Composition of the Additive Manufacturing System

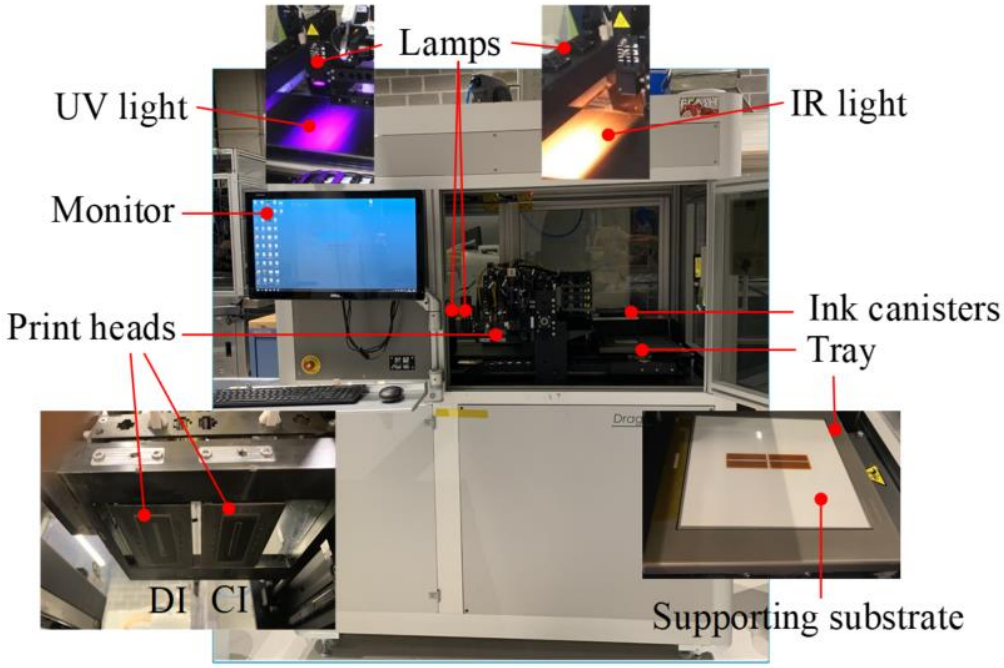

Fig. 1.3. Composition of the one-stop additive manufacturing system.

This thesis describes a novel conductor and dielectric one-stop additive manufacturing technology for manufacturing purposes. Models consist of metal and dielectric materials that can be fabricated in a single process in a short time and at a low cost using this new technology. The complete printing process can be carried out at a normal temperature and standard atmospheric pressure. As shown in Fig. 1.3, the printer dimensions are 810×1180×2000 (mm), which is convenient for in-house design requirements. A monitor is utilized to control the 3D printer. Significantly, this conductor & dielectric one-stop 3D printer comprises two print heads. Silver and acrylic ink with nano-dimension sizes can be printed simultaneously from these nozzles. After each dielectric and conductive ink layer is printed on the substrate, Ultraviolet (UV) light and infrared radiation (IR) lamps are turned on to solid the inks, respectively. When the printing process finishes, we can easily remove the samples from the substrate.

1.2.2 Fabrication Process

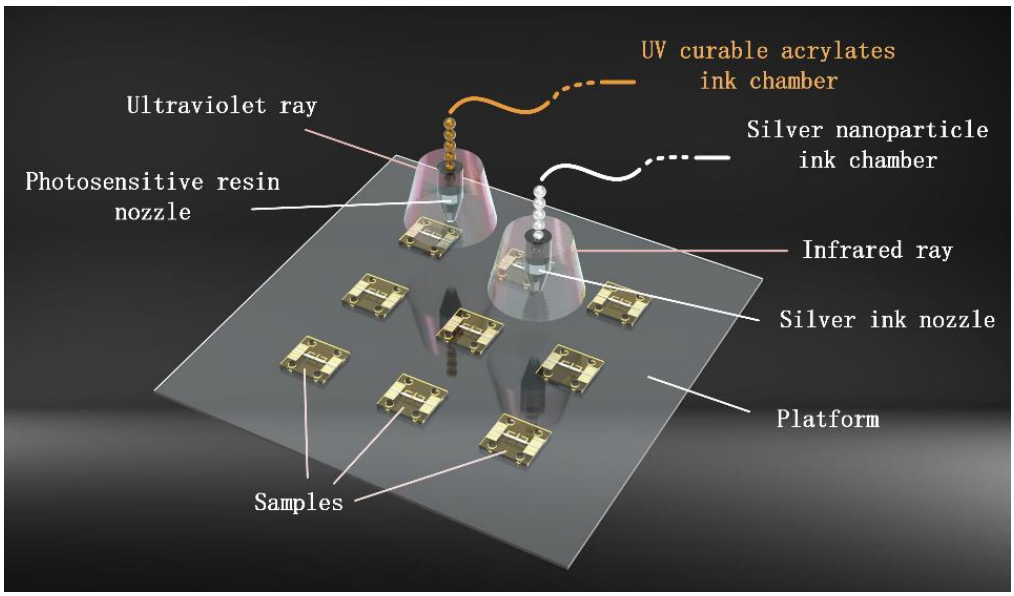

Fig. 1.4. Vertically integrated multi-layer bandpass filters under fabrication using additively manufactured electronics solution.

Fig. 1.4 illustrates nine vertically integrated multi-layer bandpass filters under

fabrication using the additively manufactured electronics solution. According to the dimensions of these samples, several bandpass filters can be fabricated at one time. Each printing head of the 3D printing system comprises 256 piezoelectric-based nozzles connecting to the chambers filled with silver nanoparticles and acrylate inks, respectively. The proposed AME solution uses piezoelectric-based nozzles with deposition of liquid inks. For the piezoelectric additive manufacturing technology, an applied voltage can generate a pressure pulse in the fluid to force a droplet of ink from the nozzle. When the applied voltage magnitude rises to a threshold voltage, the ink will be fed from the nozzles. The complete printing process can be carried out in a standard ambient atmosphere at a typical temperature of 140°C in a standard ambient atmosphere, which makes the fabrication easy and flexible. With this additive manufacturing technology, a seamless multi-metal-layer bandpass filter can be fabricated in a single substrate with accurate traces positioning, contributing to an ultra-thin profile.

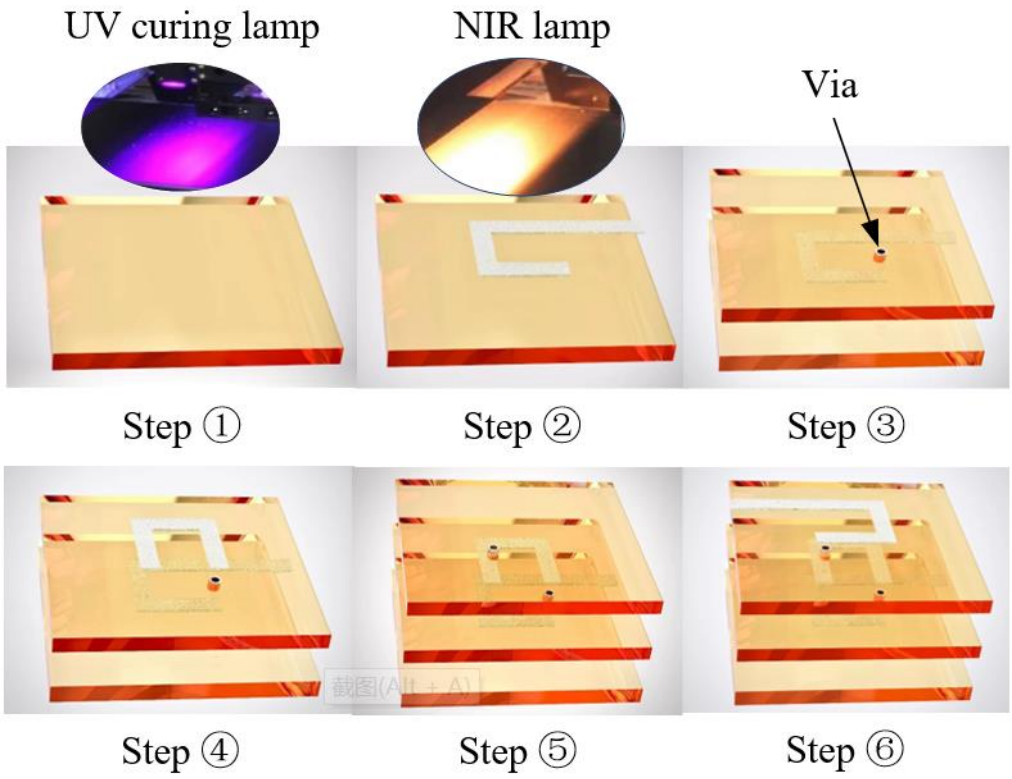

Fig. 1.5. The proposed low-temperature additive manufacturing electronics (AME) process.

More details of the fabrication procedure of a 3D spiral component are demonstrated using the proposed AME process in Fig. 1.5. During the manufacturing process, as shown in Fig. 1.5, silver nanoparticles and acrylate inks are used for the conductor and dielectric layer, respectively. They are printed layer by layer, according to the predesigned patterns. For Step 1, an ultraviolet (UV) lamp with a wavelength of 395 nm is used for curing the acrylate inks after they are ejected from the nozzles. Step 2 prints a metal strip line on the acrylate layer. A near-infrared radiation (NIR) lamp with a wavelength of 0.75-1.4 μm and 140°C to 170°C process temperature is used to sinter the conductive inks. In Steps 3-6, acrylate and conductive inks are printed layer by layer to construct the 3D spiral inductor. Vias can be printed simultaneously in the acrylate layer to connect metal strip lines in different layers, as depicted in Step 3. Where a via is desired, no dielectric ink is deposited. The fabrication is done layer by layer.

Consequently, the silver is positioned in the area where the filled via is being built, and the dielectric is around it. Compared with LTCC and semiconductor technologies, the AME solution is flexible for electronic device fabrication with design freedom adjusting the interlayer distance. Taking advantage of the AME solution, designing 3D components and devices would be a flexible proposition.

1.2.3 Materials and Precision

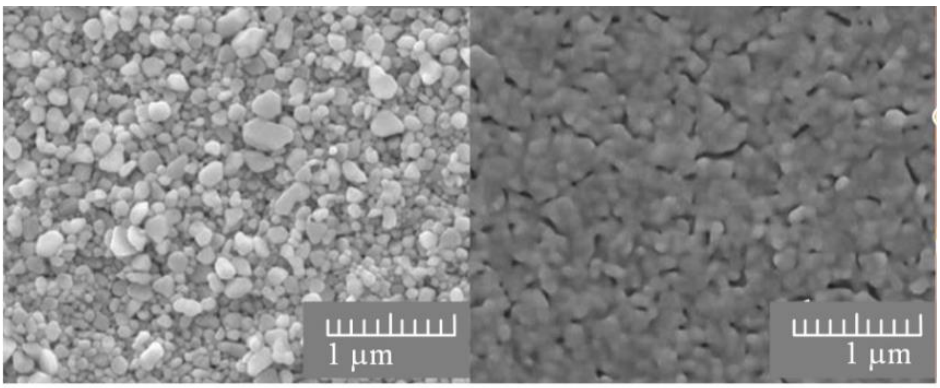

(a) (b)

Fig. 1.6. Microscopic view of inks (a) AgCiteTM nano-silver for conductor and (b) Acrylate

for dielectric

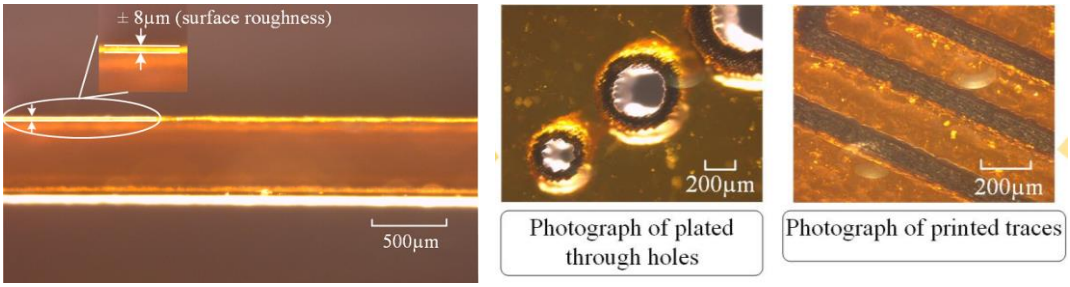

Fig. 1.7. Photograph of (a) printed substrate - cross-sectional view. (b) plated through holes and (c) printed traces.

As illustrated in Figs. 1.6(a) and (b), the conductive ink (AgCiteTM nano-silver), and the dielectric ink (acrylates) used by the inkjet system have tightly controlled particle size and excellent stability for precision AM tasks. In particular, the inks have unique and compatible sintering and curing properties. Fig. 1.7(a) is a photograph of the printed substrate in a cross-section view, plated through holes and printed traces. The variation of surface smoothness is ± 8 µm within the scan range of 1 mm length. The printer can print boards up to 160 × 160 × 3 mm^3. According to the design rules, the minimum recommended plate through hole diameter and via diameter are 400 and 200 μm, respectively. Meanwhile, the minimum recommended trace width and minimum recommended electrical clearance between traces are 110 μm. Trace thickness is suggested to be bigger than 17 um. This specification enables the machine to meet the demanding design and quality requirements of industries, such as healthcare and aerospace, where microscale precision manufacturing is expected.

1.3 Conclusion

In summary, we first introduced the background to additive manufacturing technology based on the different types and amounts of materials used in the printing system. This introduction helps readers to understand the context of additive manufacturing technology. Specifically, a novel conductor and dielectric one-stop additive manufacturing technology used for the fabrication of models in this thesis has been

introduced. With this advanced additive manufacturing technology, seamless multi-metal-layer devices can be fabricated in a single substrate with accurate positioning of traces, which helps make an ultra-thin profile possible. The advanced 3D printing technology proves that a low-cost, high-performance, time-saving manufacturing technique can be revolutionary for the upcoming 5G consumer mobile electronic systems.

The thesis is organized as follows:

Chapter 2: Literature review from single material to multi-material additive manufacturing technology. In this dissertation, we first described the background of additive manufacturing technology based on different types and amounts of materials used in the printing system. The relevant studies from single material to multi-material additive manufacturing technology were introduced here. Specifically, a multi-material additive manufacturing technology called AME solution has been introduced to fabricate the designs posited in this dissertation. This introduction helps readers to understand the context of additive manufacturing technology.

Chapter 3: 3D-printed low-profile single-substrate multi-metal layer devices with compact size. First, we proposed multi-layer patch antennas with stacked patches to increase the operational bandwidth. Broadbands can be obtained with a low-profile multi-layer patch antenna, and the extended antenna arrays are also designed and fabricated. AME solutions with tunable interlayer distance can help to realize constant inductance and capacitance in a smaller area with a thinner interlayer distance, which has great potential for designing devices with minimal effort.

Chapter 4: Vertically integrated multi-layer composite right/left-handed broadband devices. Diminishing the energy loss of the signal during propagation is always a significant issue for electronics design. Especially for the AME solution, it is a challenge to reduce the loss with a high loss tangent of 0.013. Therefore, a BPF composed of the multi-layer 3D inductance and capacitance components and a vertically integrated multi-layer composite right/left-handed devices with the broad operational band have been designed and fabricated. Good performance with compact

size and low insertion loss can be obtained by introducing the vertically integrated CRLH structure into the designs of transmission lines, BPFs, and couplers.

Chapter 5: 3D-printed metasurfaces for independent manipulation of broadband orbital angular momentum. This dissertation demonstrates two additively manufactured (AM) metasurfaces. First, an AM multi-material conductive and dielectric multifunctional metasurface is presented, generating orbital angular momentum (OAM) states at two operational broadbands with different topological charges for high-information capacity and high-security applications. Second, digitalization-coding of meta-atoms is realized in this metasurface, the objective being to simplify the design and optimization procedures. Finally, a reflective metasurface for pencil beam generation at two operational bands is designed and fabricated to verify the isolation effects of the FSS; and the possibility of developing other functional devices with the proposed meta-atoms. The design of multifunctional metasurfaces can satisfy the requirement of next-generation wireless communication systems.

References

[1] Ariadne, “Information, reed business,” New Scientist, vol. 64, no. 917, pp. 80, October 1974, ISSN 0262-4079.

[2] Freedman, H. David, “Layer by layer,” Technology Review, vol. 115, no. 1, pp. 50–53, 2012.

[3] F. Ribeiro, “3D printing with metals,” Computing & Control Engineering Journal, vol. 9, no. 1, pp. 31-38, Feb. 1998.

[4] M. Taufik, P. K. Jain, “Additive manufacturing: current scenario”. Proceedings of International Conference-ICAPIE 2016, pp. 380–386, December 2016.

[5] Vincent, A. R. Earls, “Origins: a 3D vision spawns strategy, Inc.,” Today's Machining World, vol. 7, no. 1, pp. 24–25. March 2012.

[6] “3D printed food system for long duration space missions,” sbir.gsfc.nasa.gov.,

retrieved 24 April 2019.

[7] “Did BeeHex just hit ‘print’ to make pizza at home?” huffingtonpost.co.uk, retrieved 28 May 2016.

[8] “Foodini 3D printer cooks up meals like the star trek food replicator,” pinterest.com, retrieved 27 January 2015.

[9] P. G. Bejerano, “Barcelona researcher develops 3D printer that makes ‘steaks’,” El País. retrieved 21 June 2019.

[10] L. M. España, R. Moynihan, “A researcher has developed a plant-based meat substitute that's made with a 3D printer”. Business Insider. retrieved 21 June 2019.

[11] “3D printed clothing becoming a reality,” Resins Online. archived on 1 November 2013

[12] M. Fitzgerald, “With 3-D printing, the shoe really fits,” MIT Sloan Management Review, retrieved 30 October 2013.

[13] A. Davies, “Koenigsegg one: 1 comes with 3D printed parts,” Business Insider, retrieved 14 May 2014.

[14] M. Eternity, “The ‘urbee’ 3D-printed car: coast to coast on 10 gallons?” truthout.org, 23 November 2014.

[15] P. Barker, “The local motors strati is the first four wheeler ever made by printer,” redbull.com, 21 November 2016.

[16] “Making guns at home: ready, print, fire,” The Economist, retrieved 30 October 2013.

[17] A. Rayner, “3D-printable guns are just the start, says Cody Wilson,” The Guardian, 6 May 2013.

[18] F. Manjoo, “3-D-printed gun: Yes, it will be possible to make weapons with 3-D printers. No, that doesn't make gun control futile,” slate.com, retrieved 30 October 2013.

[19] K. Perry, “Man makes surgical history after having his shattered face rebuilt using 3D printed parts,” The Daily Telegraph, retrieved 12 March 2014.

[20] “Boy gets kidney transplant thanks to 3D printing,” Sky News, retrieved 11 June

2018.

[21] R. Scopigno, P. Cignoni, N. Pietroni, M. Callieri, and M. Dellepiane, “Digital fabrication techniques for cultural heritage: a survey,” Computer Graphics Forum, vol. 36, no. 1, pp. 6-21, 2017, doi: 10.1111/cgf.12781

[22] Alec, “Museum uses 3D printing to take fragile maquette by Thomas Hart Benton on tour through the States,” 3ders.org, 14 July 2015.

[23] “British Museum releases 3D printer scans of artefacts,” pinterest.com, 4 November 2014.

Chapter 2 Literature Review- From Single-Material to Multi-Material Additive Manufacturing Technology

2.1 Introduction

Additively manufactured electronics (AME) technology is a game-changer that could completely disrupt the electronics manufacturing value chain in Industry 4.0. AME technology has featured the advantages of low cost, fast prototyping, 3D customized design freedom, and a distributed manufacturing cycle in the electronics industry. The 3D printing technique has great potential to complement or replace traditional manufacturing in some areas, such as the space and defense industries. Many complex systems that are difficult to implement using conventional fabrication methods can be prototyped, realized, and eventually produced by taking advantage of AME techniques. According to the available literature, AME-inspired electronic components have been achieved in transistors [1-2], interconnects [3], transmitarrays [4-5], microwave circuits [6-7], electromagnetic (EM) lenses [8-11], reflectarrays [12], frequency selective surfaces (FSS) [13-14], antennas [15-23], waveguides [24-25], and metamaterials [26-32]. Most of these applied AME approaches are based on printing the entire geometry with a single material process, through either a metal-only or a dielectric-only AME system [4-9], [12-13], [26-28], or by loading metallic paint with metal casting 3D printers on different kinds of substrates [14-17]. Examples here are Kapton [14], textile [15], or paper [16-17]. Printing the dielectric parts with metal coating or tape is also a popular choice [18-20], [29].

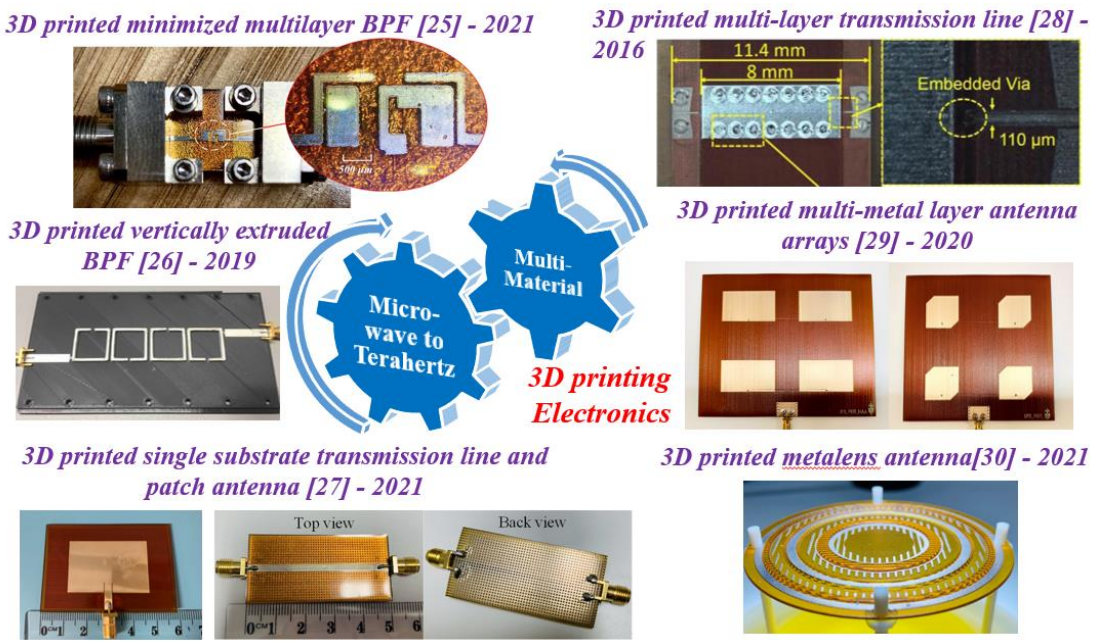

Fig. 2.1. Emerging 3D printing technologies in microwave components and radio frequency electronics - a game changer in the manufacturing value chain in Industry 4.0.

As demonstrated in Fig. 2.1, advances in integrated printing of conductive and dielectric materials have enabled a new generation of additively manufactured microwave components and radio frequency electronics to emerge [33-38]. With high-conductivity metallic ink and low-loss dielectric ink materials, the emerging multi-material AME technique can be exploited to design and implement multi-layer microwave and terahertz components that function exceptionally well.

Compared with traditional fabrication methods, AM has unique advantages. For example, conventional computer numerical control (CNC) requires a post-processing/assembling procedure for prototyping. However, metal 3D printers can fabricate microwave components without post-processing to avoid additional loss (e.g., interconnection). In addition, compared with low-temperature cofired ceramic (LTCC) and semiconductor technologies, the AME solution provides flexible design freedom by adjusting the interlayer distance. In contrast, traditional fabrication methods have strict design rules (e.g., the space between metal layers), which cannot be breached. Added to the above-mentioned advantages, AM can adjust the substrate permittivity by changing the deposit density (or infill percentage) [18], [34]. Further, anisotropy can be

created when a substrate made of polylactic acid (PLA), an almost isotropic material, is printed with periodic patterns in its internal structure [39]. The substrate anisotropy is related to the infilled percentage and the geometric patterns of air spaces. In some cases, the anisotropy caused by 3D printing techniques can be used to design specific metamaterials. As mentioned in [27], a uniaxial anisotropic metamaterial has been proposed utilizing the artificial anisotropy created by 3D printing techniques.

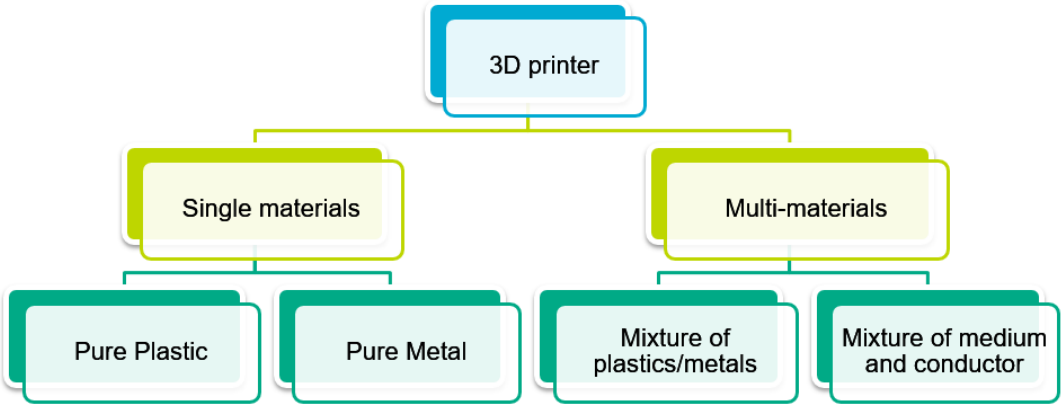

Fig. 2.2. Emerging 3D printing technologies in microwave components and radio frequency electronics - a game changer in the manufacturing value chain in Industry 4.0.

In today's environment, with countless research and engineering efforts, a system of 3D printing technology has emerged. Fig. 2.2 depicts the classification of 3D printer recording to materials. With the development of technology, more and more materials are introduced to 3D printing technology. Even a multi-material 3D printer is available.

2.2 Commercial Additive Manufacturing Facilities

There are three leading manufacturing technologies employed in 3D printing [40]: continuous liquid interface production (CLIP), material jetting (PolyJet), and selective laser sintering (SLS). CLIP is a proprietary photopolymerization method to create smooth-sided solid objects with resins. The CLIP process is based on a pool of liquid photopolymer resin whose bottom ranges from transparent to ultraviolet light. Then, the printed precise cross-section of the object is illuminated by an ultraviolet light beam that shines through the transparent bottom. Compared with earlier commercial 3D printing techniques, CLIP can produce objects with smoother sides. The PolyJet process

jets curable liquid photopolymer onto a build tray layer by layer, followed by applying a UV source to cure the material. It can produce features in the 100s of microns.

Due to its underlying digital technology, PolyJet can be more efficient and accurate for model designing and fabricating, which curtails costs. However, the size and viscosity of the jetted material must be compatible with the printer head. SLS is an AME technique that sinters powdered material with a laser power source. The space-point defined by a 3D model is sintered by laser automatically, which binds the material together to create a desired solid structure. Because the process of SLS is entirely self-supporting, it makes possible a process called nesting that builds parts within other parts. It means that the SLS process can produce highly complex geometries that other techniques cannot reach without trapping material inside or altering the surface.

Table 2.1 lists the industry-level commercial additive manufacturing (AM) facilities widely used by global customers. As seen in the table, the manufacturing methods of these 3D printers have been updated based on traditional additive manufacturing methods. PolyJet is still a popular additive manufacturing process due to its high accuracy and high efficiency for design and fabrication. After the PolyJet method, fused filament fabrication is the most commonly utilized technology today. It is a process of feeding a continuous filament from a large spool through a moving, heated printer extruder head. Depositing it on the top of growing product, this technology can effectively reduce costs, and a wide variety of filament materials can be extruded using this technology.

Nowadays, the single-material printing technique is still the dominant force. According to Table 2.1, Stratasys F270, Stratasys Fortus 450mc, and Markforged X7 can fabricate models with different kinds of dielectric materials. The fused filament fabrication method is utilized in the process. These three types of 3D printers are suitable for fabricating medium-sized models. Different dielectric materials can be printed with high accuracy. In particular, the accuracy of Stratasys Fortus 450mc can reach 70 μm at the x/y axis, which is suitable for precision prototyping small models with fine printing. The BigRep ONE can fabricate models from 350 mm × 350 mm × 300 mm to 1005 mm × 1005 mm × 1005 mm. It is more suitable for manufacturing big

models like furniture. However, the printing resolution of the BigRep ONE is not high and may not be ideal for high-frequency microwave circuits and antenna designs. The Stratasys J750 uses the PolyJet method. It can be used to fabricate multi-colored models and ones with varying levels of transparency with different dielectric materials.

TABLE 2.1. 3D PRINTING FACILITIES

No.	Machine	Process	Size (mm3)	Material/s	Accuracy (x/y)	Layer thickness	Printing capability
1	Stratasys F270	Fused Filament Fabrication	305 ×254 × 305 (max)	Acrylonitrile styrene acrylate copolymer, Polylactic acid.	±100 µm	127-330 µm	Dielectric only
2	Stratasys Fortus 450mc	Fused Filament Fabrication	406 × 355 × 406 (max)	Acrylonitrile styrene acrylate copolymer, Acrylonitrile butadiene styrene.	70 µm	127-330 µm	Dielectric only
3	Markforged X7	Fused Filament Fabrication	330 ×270 × 200 (max)	Nylon /Onyx (main thermoplastic) carbon fiber/Kevlar/Fiberglass (reinforcement)	±100 µm	50-100 µm	Dielectric only
4	Markforged Metal X	Atomic Diffusion Additive Manufacturing	235 × 68 × 66 (max)	Stainless steel	±125 µm	50-200 µm	Metal only
5	BigRep ONE	Fused Filament Fabrication	350×350 × 300 (min) 1005 ×1005×1005 (max)	Polylactic acid, Nylon, Polycarbonate.	100-1000 µm	100-1400 µm	Dielectric only, suitable for manufacturing of huge size model.
6	Stratasys J750	PolyJet	500 x 400 x 200 (max)	Vero (white, clear) Agilus30 (elastomer-like)	<200 um	14 µm	Dielectric only, multi-color, accuracy is affected by model size
7	Formlabs Form 2	Stereolithography	145 × 145 × 175 (max)	Clear photopolymer resin	200 µm	25-200 µm	Dielectric only
8	HP Jet Fusion	Multi-jet Fusion	406 × 305 × 406 (max)	PA-12GB (Nylon 12 with glass bead reinforcement)	±200 µm	80-100 µm	Dielectric only
9	nScrypt 3-Dn-600	Aerosol jet printing	600 × 600 × 150 (max)	DuPont CB028 conductive paste and Acrylonitrile butadiene styrene	10 µm	0.65 µm	Dielectric and conductive
10	Dragonfly additively manufactured system	PolyJet (piezoelectric inkjet)	160 × 160 × 3 (max)	Acrylates and AgCite	110 µm	0.3 µm for AgCite and 2.5 µm for Acrylates	Dielectric and conductive

HP Jet Fusion processes use the multi-jet fusion technology. Unlike the other 3D printing technologies, multi-jet fusion prints each layer of new material and agent on top of a previous layer that is still molten so that both layers fuse completely and polymers can lock into each other across the layer boundary. In addition, HP Jet Fusion 3D printing solutions using 3D high reusability PA 12 provide up to 80% powder reusability, producing functional parts batch after batch. Thus, the HP Jet Fusion 3D printer has the advantages of being low-cost and environmentally friendly. However, it can only fabricate using a single dielectric material. Formlabs Form 2 is another single dielectric material 3D printer. Stereolithography and clear photopolymer resin are the

process method and materials of the Formlabs Form 2, respectively. The maximum model size that can be fabricated is 145 mm × 145 mm × 175 mm, which means this machine is more suitable for prototyping small models.

In recent years, metal printers (for example, Markforged Metal X) have been introduced and are available to many researchers and engineers. Metal printers can prototype microwave devices without the need for assembling, thus avoiding interconnection loss. However, 3D-printed prototypes are expensive, which is its major disadvantage. In comparison, nScrypt 3-Dn-600 and DragonFly LDM are two representative facilities that can simultaneously print conductive and dielectric inks for prototyping. nScrypt 3-Dn-600 is good at precision prototyping electronic devices with extremely high accuracy. The printer can reach 600 mm × 600 mm × 150 mm to fabricate models with high profiles. DragonFly LDM is suitable for the seamless printing of electronic components with multiple metal-layer structures, a type of structure that has attracted significant interest from the space and defense industry, which requires low-volume production but exceptional performance for electronic devices. Up to 30 metal layers can be fabricated in a single substrate with a low profile. Nonetheless, the materials used by the DragonFly LDM are single-use.

2.3 Design Examples: Additively Manufactured Devices from Single-Material to Multi-Material

2.3.1 Single-Material (Dielectric/Conductive) 3D-Printed Designs

At the beginning of the 3D printing era, 3D printers could only prototype models with a single dielectric material. Compared with the multi-material 3D printer, the single-material 3D printer is easy to fabricate. The machine only needs to meet the processing requirements of a single material, such as temperature or pressure, and only needs one printhead. Over the last decade, dielectric 3D printing technology has been developed that can manufacture a wide range of microwave and antenna components such as polarizer lenses [8-9], reflectarrays [12], frequency selective surfaces (FSS)

[13-14], metamaterials [26-27], and transmission lenses [41]. Most of these components are involved in beam shaping. For instance, J. Zhu et al. presents a 3D-printed dielectric circular polarized beam-shaping lens with a boresight pencil beam based on a linear-to-circular polarization conversion coding unit [8]. Zhou et al. have proposed an all-dielectric multi-layered and broadband radar absorbing metamaterial (RAMM) with different structures designed in each layer using the selective laser sintering (SLS) method [26]. Taking advantage of additive manufacturing technology, the RAMM is fabricated with high accuracy and a wide operational band (8 to 18 GHz). Their dispersion and anisotropy are cleverly engineered to increase design freedom, leading to structures with very complex geometries.

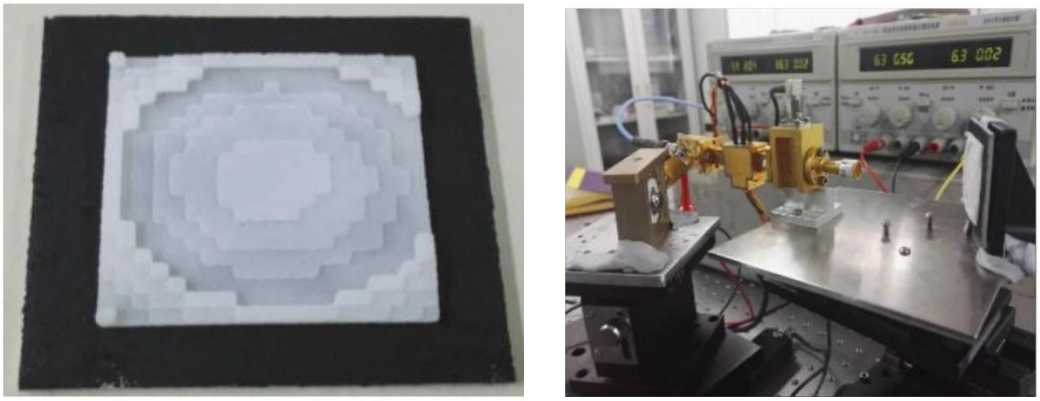

(a) (b)

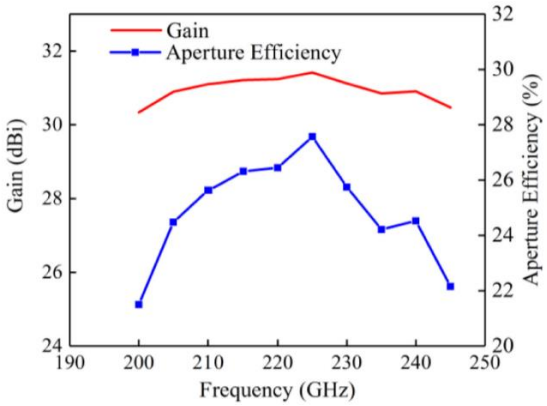

(c)

Fig. 2.3 (a) 3D-printed prototype and (b) Testbed of the 220 GHz dielectric reflectarray, and (c) Gain and aperture efficiency [12].

The dielectric-only 3D printing technique has also been applied to prototyping

terahertz components. J. H. Barton et al. demonstrated a wideband high-gain terahertz dielectric reflectarray working at 220 GHz [13]. The reflectarray unit cell consists of a ground plane and a dielectric block, whose height is utilized to adjust the reflection phase. Since the structure of the unit cell is simple, a low-precision manufacturing method is acceptable. As shown in Figs. 2.3(a), (b), and (c), a dielectric reflectarray composed of 40 × 40 elements and occupying an area of 28 × 28 mm² is designed at 220 GHz with a maximum gain of 31.3 dBi and an aperture efficiency of 27.6%. A wide 1-dB gain bandwidth of 20.9% can be obtained for 220–246 GHz.

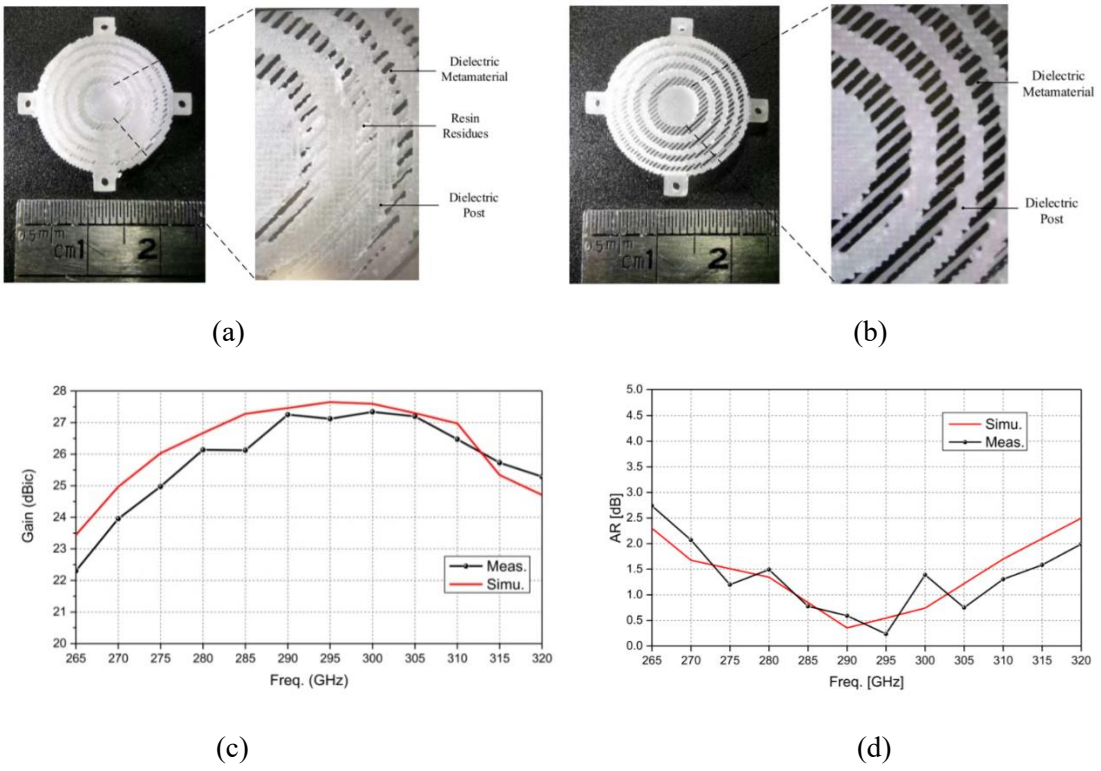

Fig. 2.4 Photograph of the fabricated modified Fresnel lens using (a) Formlabs-recommended and (b) in-house-developed approaches. Measured and simulated (c) gains and (d) ARs of the CP modified Fresnel lens at different frequencies [9].

Additionally, G. B. Wu et al. introduces a novel 3D-printed high-gain circularly polarized (CP) modified Fresnel lens antenna operating at THz frequencies [9]. A raft and supports were used during the fabrication to avoid adhesion between the printed object and the build platform, where the lens was printed slanted. The fabricated CP lens prototype is shown in Fig. 2.4(a). The fabricated lens suffered from limited printing

accuracy and uniformity using the printing method recommended by Formlabs. To push the performance envelope of the 3D printer to realize the proposed CP THz lens, an improved “in-house developed 3D printing method” was offered. The CP lens was printed horizontally, and thin struts with a diameter of 0.25 mm were added to support the weight of the lens. The fabricated CP lens prototype using this printing method is shown in Fig. 2.4(b). This method's printing accuracy is much higher, and the uniformity problem was subsequently resolved. Finally, as shown in Figs. 2.4(c) and (d), the experimental results confirm that the 3D-printed CP lens can realize RHCP with a 3-dB gain in bandwidth over 15.1% (from 275 to 320 GHz) and 3-dB AR bandwidth over 18.8% (from 265 to 320 GHz).

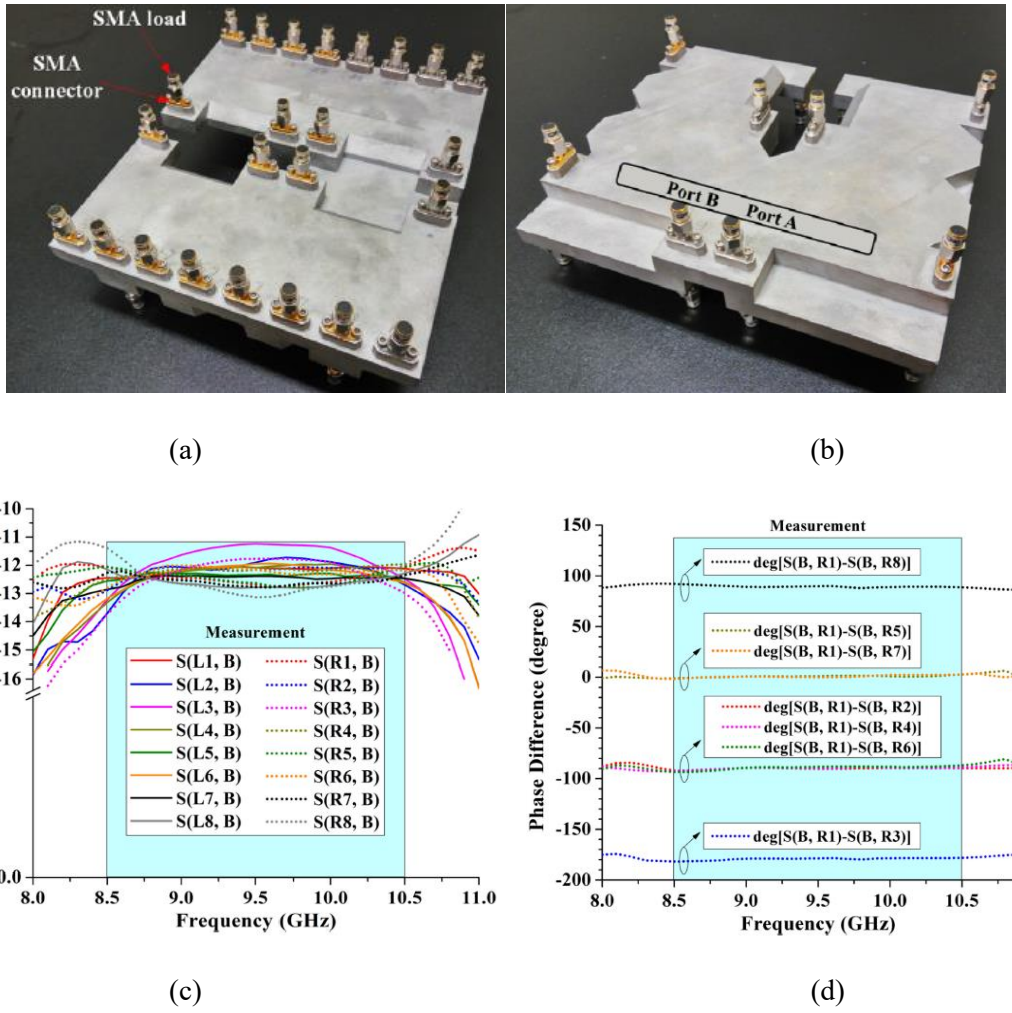

Fig. 2.5. Photographs of the manufactured 16-way power combiner. (a) Front view. (b) Rearview and the (c) RF-measured power division of the 16-way power combiner (d) RF-measured phase differences between different output [6].

There is even more possibility of applying 3D printing technology in microwave communication with a metal-only printer. Since metal materials can restrain electromagnetic waves, 3D-printed devices based on metal waveguides have been discussed in the literature [6], [22]. For example, a 16-way power combiner featured a compact geometry with good isolation (>20 dB) among the input ports, suitable amplitude imbalances (within ±1 dB), and small phase deviations (within ±1°) in a wide operational bandwidth (BW) of 8.5-10.5 GHz has been fabricated with a metal printer [6]. Fig. 2.5 depicts photographs of this power combiner, its radio frequency (RF)-measured power division, and phase differences. The one-stop direct metal printing technology can fabricate complex metallic models in a single piece, avoiding inevitable adjacent gaps and alignment errors among the metal layers, which may cause wave leakages and multi-reflections.

In addition, a highly efficient and compact monopulse system has been proposed, one that integrates both a frontend antenna array and a backend comparator network in [22]. Due to its complex structure, this compact monopulse system could not be fabricated in a single piece of metal using traditional machining methods. For this reason, the direct metal laser sintering (DMLS) technique was chosen for fabrication, after considering cost, printing precision, material availability, and the desired properties.

These single-material (dielectric/conductive) 3D-printed designs reveal the possibility of fabricating electronic products with AM technology. It is also apparent that the single-material printing process hinders the development of microwave devices with exceptional performance, which often requires prototyping with conductive and dielectric materials.

2.3.2 Prototyping Microwave Devices by Plating Metal on 3D-Printed Dielectric Models

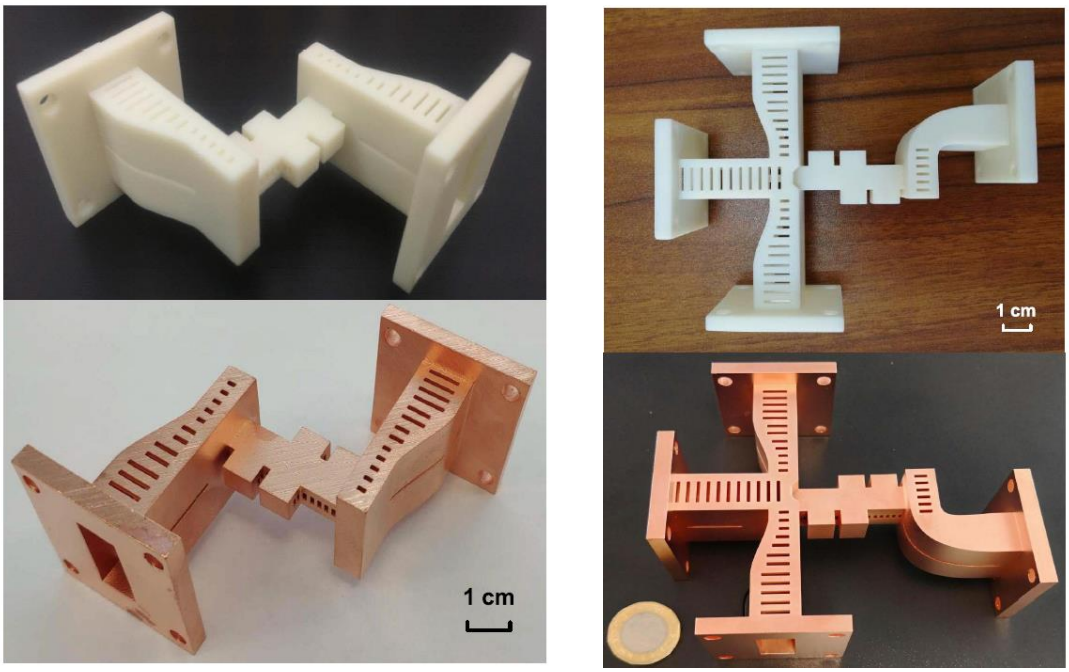

(a) (b)

Fig. 2.6. Photographs of the SLA-printed prototypes before and after surface metallization. (a) Waveguide-coax-waveguide transition. (b) Magic-T [24].

Many microwave components are composed of both dielectric and metal materials. Compared with single-metal 3D-printed models, the method of plating metal on 3D-printed dielectric models has the advantages of lower cost and lighter weight [23-24], [42-45]. For example, in [23], a new class of broadband transition and a monolithic waveguide magic-T is fabricated using polymer-based additive manufacturing and copper electroplating techniques. As shown in Figs. 2.6(a)-(b), the devices were SLA-printed in a vertical resolution of 70 μm with the ceramic-filled photosensitive resin Somos PerForm. Then, in the metallization process, a 10-μm-thick conductive layer of copper was electroplated onto the transition model on a seed layer of electroless plated nickel. For the magic-T, the copper layer was further increased to at least 30 μm to enhance the thermal handling capability. Photographs of the fabricated prototypes are shown in Fig. 2.6. In addition, a dual-band bandpass filter with a high-quality factor

and wider stopband was realized using the SLS 3D-printing technology with the PA12 (nylon material) as a structure. Then a 10-μm thick copper layer was metalized on the surface [24].

In addition to plating the whole surface of the printed model to construct lightweight samples, adhering the shaped copper tape to the models through the cutting-plotter-based technique is another popular way to apply 3D printing technology. Researchers usually cut the desired shapes out of tape and apply them at specific locations on the 3D-printed models. It is a low-cost and flexible way to fabricate devices. However, the accuracy of the cutting and adhesion steps is difficult to guarantee, especially for high-frequency designs, and the fabrication process is complicated.

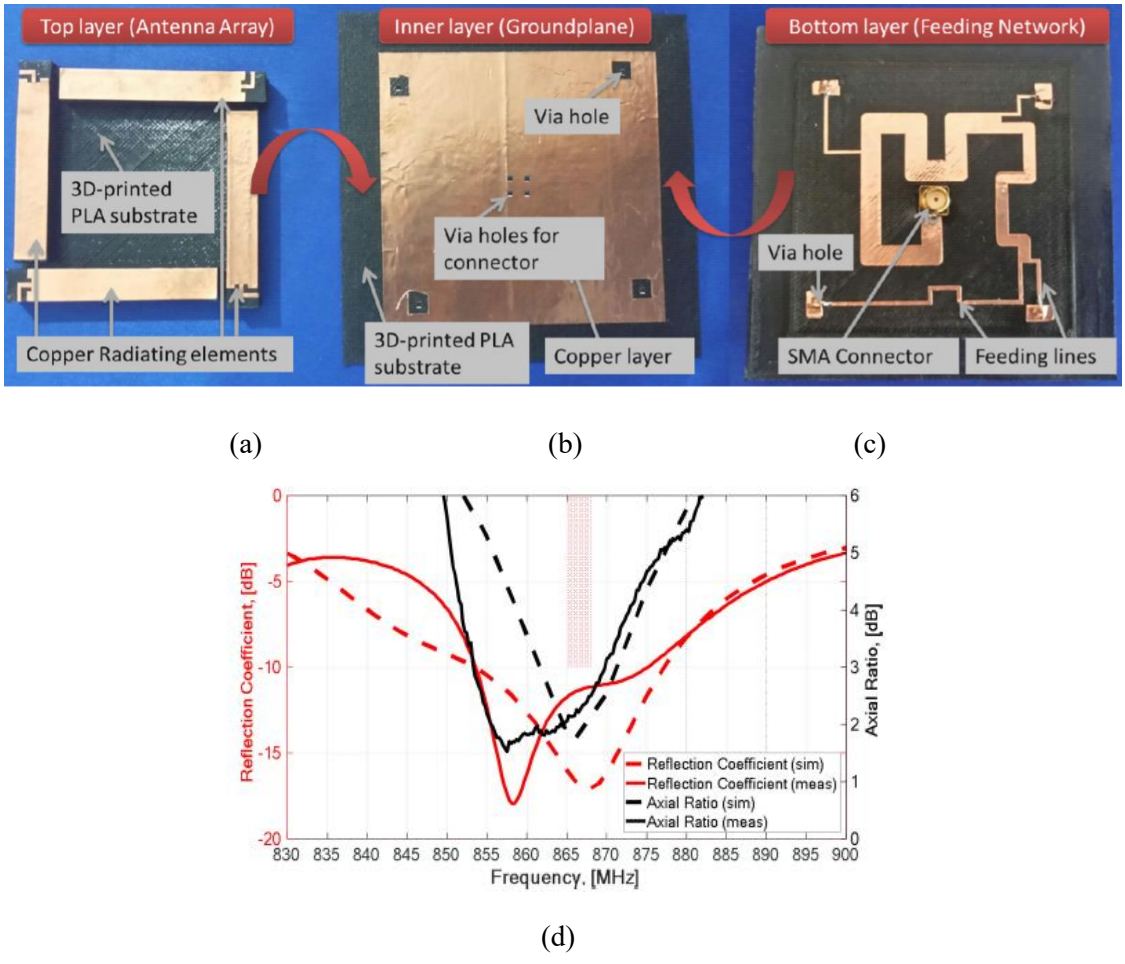

Fig. 2.7. Components of the designed 3D-printed antenna for a handheld UHF RFID reader. (a) Front view, (b) Ground plane, (c) Bottom view, and (d) Simulated and measured reflection coefficients and axial ratios [20].

In [20], a compact and low-profile circularly polarized antenna is presented for a handheld ultra-high frequency (UHF) RFID reader. The proposed antenna realizes an improved gain and appreciable size reduction by taking advantage of the low-loss and moldability of the 3D printing materials combined with a specific design strategy. As seen in Figs. 2.7(a)-(c), the antenna top view shows four radiating elements placed over a 3D-printed annular square polylactic acid low-loss support. The bottom view picture depicts the feeding network; a common ground plane is shared between the radiating elements and the feeding network. The two PLA parts were manufactured using a dielectric 3D printer. The conductive parts (i.e., radiating elements, feeding network, feeding lines, and ground plane) were realized using adhesive copper tape-shaped through the cutting-plotter-based technique. Fig. 2.7(d) shows simulated and measured reflection coefficients and axial ratios. Since all the copper tape is manually applied to the 3D-printed substrates, errors and complexity in the manufacturing process may actually increase.

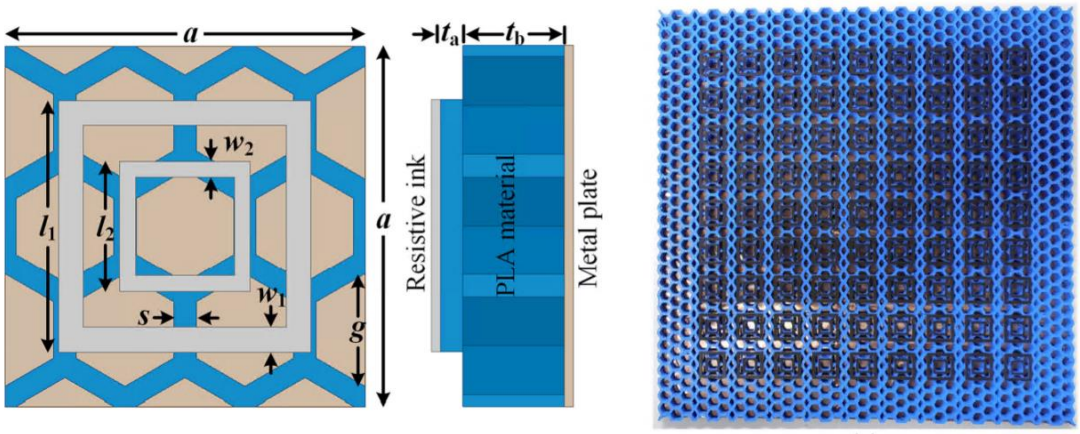

(a) (b)

Fig. 2.8. (a) Unit cell geometry of the proposed broadband absorber. (b) Photograph of the fabricated prototype [29].

In [29], a broadband metamaterial absorber prototyped by a resistive conductor on 3D-printed dielectric models is proposed. As shown in Figs. 2.8(a)-(b), this design comprises periodic arrays of honeycomb core as the constituent dielectric, onto which resistive paint has been deposited to realize broadband absorption. A screen-printing technique is applied to deposit the Y-shield resistive ink uniformly. Moreover, a

negative mask made from polydimethylsiloxane substrate was utilized to paint the ink on the square loop patterns accurately. This technology can simplify fabrication and reduce size and position errors caused by manually applying the tape.

2.3.3 Prototyping Microwave Devices by Printing Conductive Inks on Existing Substrates

Printing conductive inks on existing substrates (such as textiles and papers) is a good prototyping choice. This method can print a specific metallic shape on a substrate without size and position errors caused by manually applying the tape. Inkjet printing is the most common method of printing conductive inks on existing substrates. This additive electronic fabrication method is gaining interest in consumer and industrial applications as a low-cost, highly scalable, and environmentally friendly alternative to typical laminate-based fabrication.

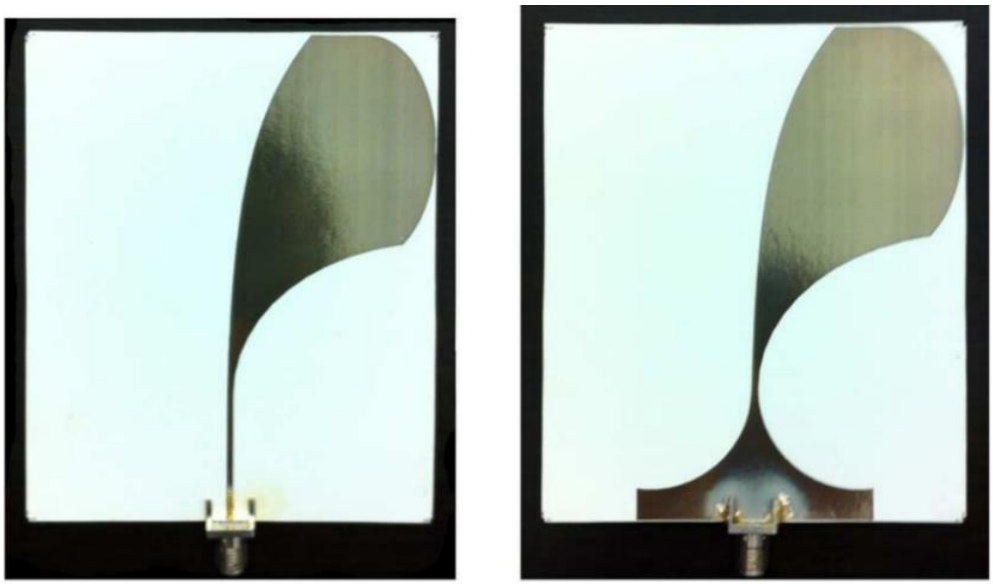

(a) (b)

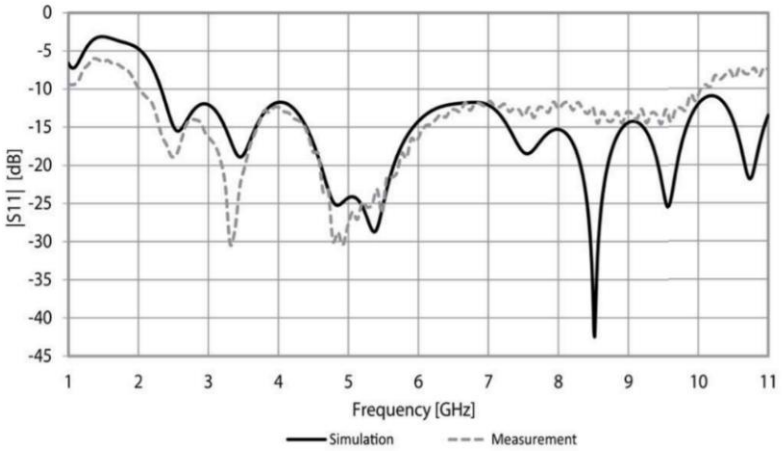

(c)

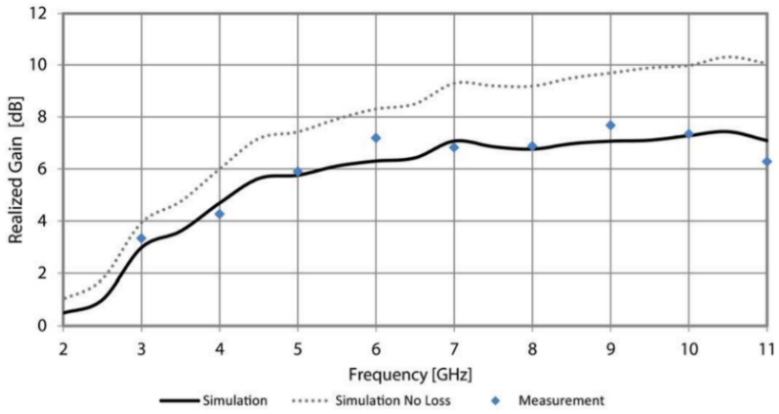

(d)

Fig. 2.9. Fabrication of the antipodal Vivaldi antenna with (a) front and (b) back views. Measurement of the antipodal Vivaldi antenna with (c) S_{11}, and (d) gain versus frequency [17].

In [16], a novel electromagnetic band-gap structure (EBG) with single-ring resonators is inkjet printed on commercially available photo paper using conductive nano-silver ink. However, the realized gain of the EBG array is not desirable; in fact, it is only 0.95 dBi. The paper is revealed to be a lossy substrate with a loss tangent near 0.06. Subsequently, producing high gain antennas on paper is challenging due to the relatively high loss tangent paper exhibits at microwave frequencies. For example, a Vivaldi antenna was designed on a paper substrate for wideband and high gain [17]. Traveling or leaky wave antennas demonstrate much less substrate dependence and have higher directivities than resonant antennas. Vivaldi is a traveling wave antenna where the maximum separation of the arms limits the lowest operating frequency and the maximum frequency by the match at the feed. As seen in Figs. 2.9(a) and (b), each

antenna side is printed separately along with alignment marks to fabricate the Vivaldi. The Vivaldi is laser sintered, while holes are laser cut through the alignment marks to allow alignment pins to align the two layers during bonding. A light spray adhesive is used to bond the two layers. Fig. 2.9(c) shows the corresponding simulated and measured return losses, which are in good agreement over the entire operating band. The inkjet-printed Vivaldi antenna exhibits a significantly high gain of up to 8 dBi and a wideband from MHz frequencies to pass 10 GHz in Fig. 2.9(d). The measured results of this antenna verify that high gain can be attained using inkjet printing on a lossy paper substrate. It lays a strong foundation for low-cost, high gain, and wideband antenna fabrication with environmentally friendly substrates using an inkjet printing process.

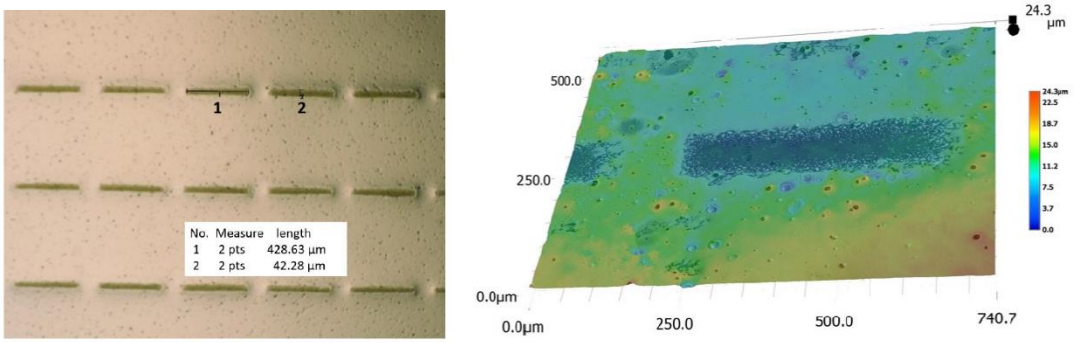

(a) (b)

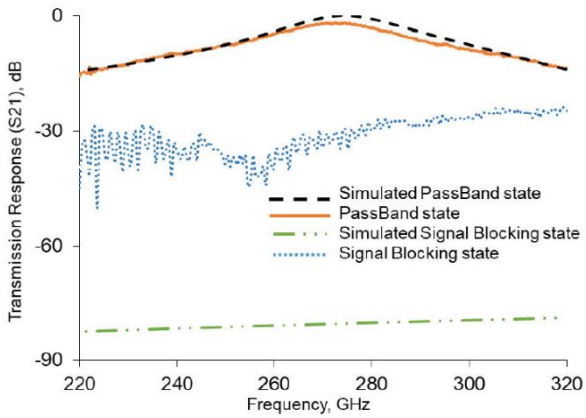

(c)

Fig. 2.10. (a) 280 GHz slot bandpass printed FSS layout. (b) 3D surface profile measurements of a single slot and (c) transmission response of the proposed FSS at 280 GHz [14].

In addition, bandpass frequency selective surfaces (FSS) operated at low-THz frequency regions can be precisely and accurately fabricated with aerosol jet printing on Kapton substrates [14]. Kapton is a polyimide film with excellent flexibility over a wide temperature range which can be deployed to improve communications in space and terahertz applications. The bandpass FSS operated at 280 GHz consists of simple slot elements arranged in a square. The bandpass FSS in [14] consisted of an array of 83×83 elements over an area of 6.35 cm × 6.35 cm with 0.05 mm thickness. Fig. 2.10(a) depicts the layout of the printed 280 GHz slot bandpass FSS. The 3D surface profile of a single slot under a microscope is shown in Fig. 2.10(b); it has dimensions of 0.43 mm ×0.045 mm. An average tolerance of 5% was measured. Fig. 2.10(c) shows the measured and simulated transmission responses. A wideband transmission response was observed, -10 dB passband ranging from 240 GHz up to 310 GHz with a bandwidth of 25%. Measured and simulated transmission responses demonstrated a gap of about 20 dB between the passband and signal-blocking states.

3D printing of wearable electronics is promising. However, the fabric has elastic physical properties that make inkjet-printing-based deposition difficult. The pattern tends to dissipate when printing tracks on textiles and the process cannot produce a continuous conducting track without many layers being printed. Added to this, a high solvent content (around 85%) of the inks is always required to improve inkjet printability. The temperature it can withstand is challenging, meaning that a sufficiently low curing temperature for inks is required. With this in mind, surface pre-treatment of the fabric is usually necessary for wearable printing to function well. In [15], to reduce the cotton fabric surface roughness, the fabric is pre-treated using a screen-printed interface layer before further inkjet printing, which is a UV-curable polyurethane acrylate-based interface paste. Meanwhile, in the end, dipole antennas operating at around 1.89 GHz on different substrates were fabricated and measured successfully. The surface pre-treatment adds further complexity to the printing process of manufacturing on fabric.

Constructing devices by printing conductive inks on existing substrates reduces the errors of size and position that can occur during the manual application of tape.

However, dielectric substrates with appropriate electric characteristics are difficult to find, and the necessary surface pre-treatment adds complexity to the fabrication process. Therefore, it is necessary to develop multi-material 3D printing technology with conductive and dielectric inks.

2.3.4 Multi-Material Additively Manufactured Devices using Conductive and Dielectric Inks

It is challenging to handle advanced designs with complex structures composed of conductive and dielectric parts in a single unit. Multi-material additive manufacturing technology can simplify the fabrication process and reduce the chance of making errors during post-processing.

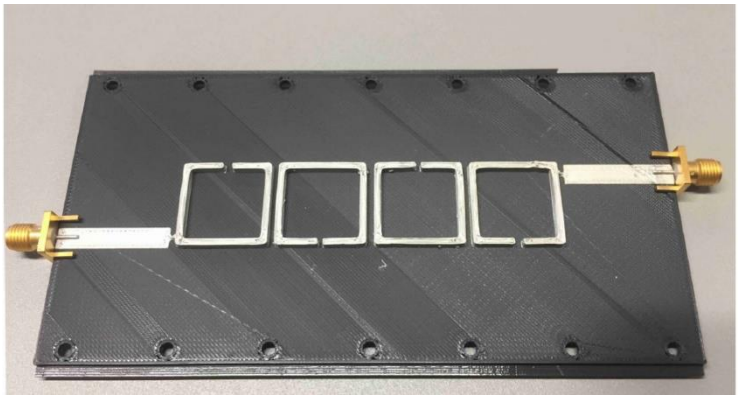

(a)

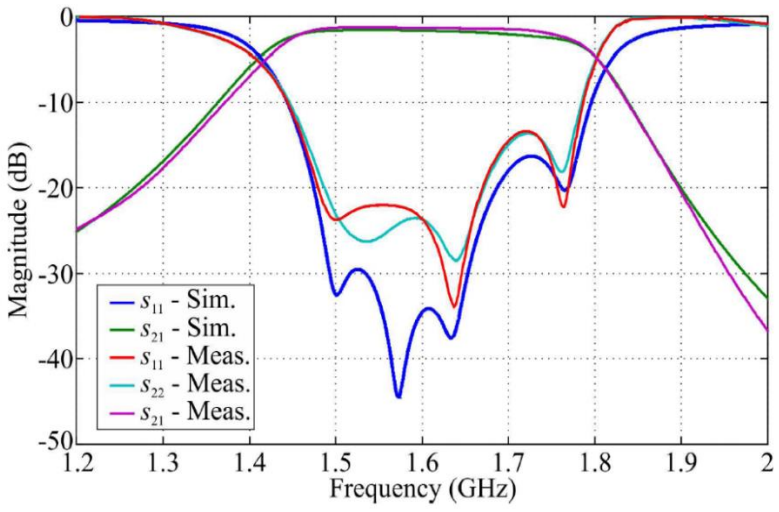

(b)

Fig. 2.11. (a) 3D-printed prototype of the 2 mm-high SRR bandpass filter with center frequency at 1.6 GHz. (b) Measured and simulated reflection and transmission coefficients of the filter [34].

In [34], 3D-printed bandpass filters with coupled vertically extruded split ring resonators were fabricated on the V8 DDM printing platform that can print thermoplastics and conductive ink together at the same time. The V8 DDM printing platform contains two print nozzles. One nozzle deposits the V8 amphiphilic silver ink, whose flow is controlled by an onboard pneumatic system. The second nozzle is used for standard FDM of polymer filaments. In addition, the permittivity and loss tangent of the FDM substrate can be determined by controlling the infill density (i.e., the amount of filament printed inside the object). As a result, as seen in Fig. 2.11(a), a 3D-printed prototype of a 2 mm-high SRR bandpass filter with a center frequency at 1.6 GHz is possible. The dielectric substrate of the filter was printed with PLA filament with an infill density of 70% to target the desired design permittivity of 2.26, with the resulting loss tangent estimated to be 0.01. The ground plane for the filter is formed with conductive aluminum tape to reduce printing time and the amount of silver ink; however, it adds complexity to the fabrication process. The simulated and measured S-parameters of the 2 mm-high SRR bandpass filter are shown in Fig. 2.11(b), and they agree well. Compared with a planar microstrip filter with the same footprint, the 3D-printed SRR bandpass filter has the advantage of more than two times wider bandwidth.

This V8 DDM printing platform successfully realized the printing of both conductive and dielectric materials. However, the size of the nozzle, which is 0.25 mm, limits the printing resolution to no smaller than 0.25 mm. In addition, some frequency shifts also resulted from fabrication errors. For example, the sizes of the gaps of all the resonators were found to be approximately 18% larger on average than the nominal value. Therefore, improving the accuracy is still a challenge of printing thermoplastics and conductive ink with a V8 DDM printing platform.

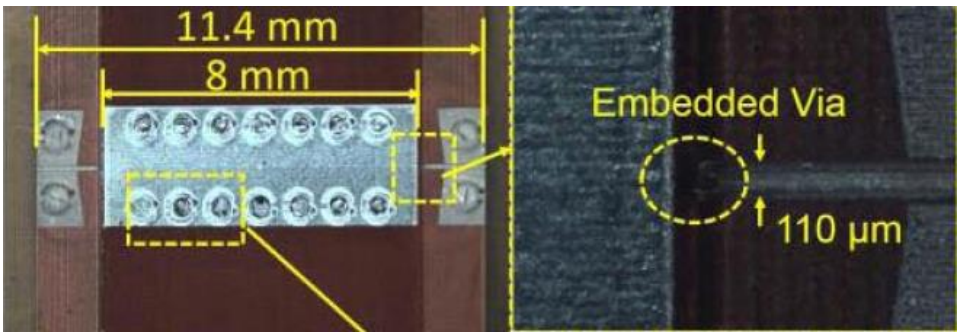

(a) (b)

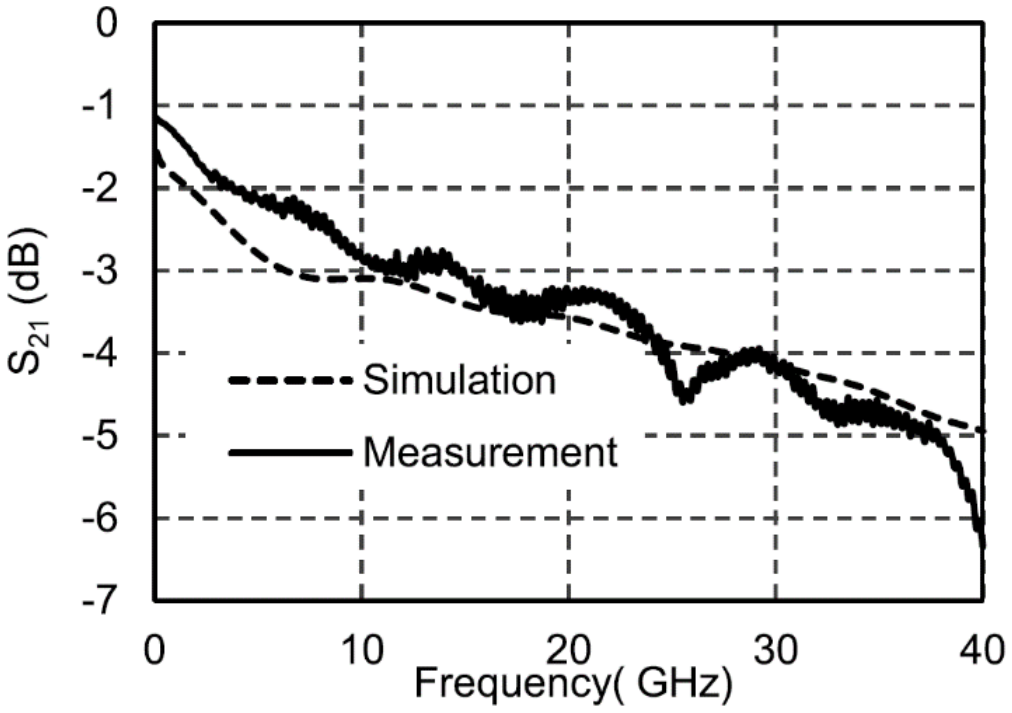

(c)

Fig. 2.12. (a) Fabricated prototypes and (b) details of the vias. (c) Measured and simulated S-parameters of the interconnect with a total length of 11.4 mm [36].

In [36], an nScrypt 3-Dn-600 print system serves to fabricate multi-layer interconnects with vertical transitions. The nScrypt 3-Dn-600 print system can realize a single line as small as 10 μm for silver ink and 80 μm for polyimide. Figs. 2.12(a) and (b) depict the fabricated prototype and details of the vias. Fig. 2.12(c) illustrates the simulated and measured results of the interconnect. Good matching is achieved below 40 GHz, and the measurements show an IL of 1.2 dB at 1 GHz and 6.3 dB at 40 GHz for the 11.4 mm sample.

2.3.5 Recent Advances in 3D-Printed Multi-Material Non-Planar Components in the Sub-Terahertz Regime

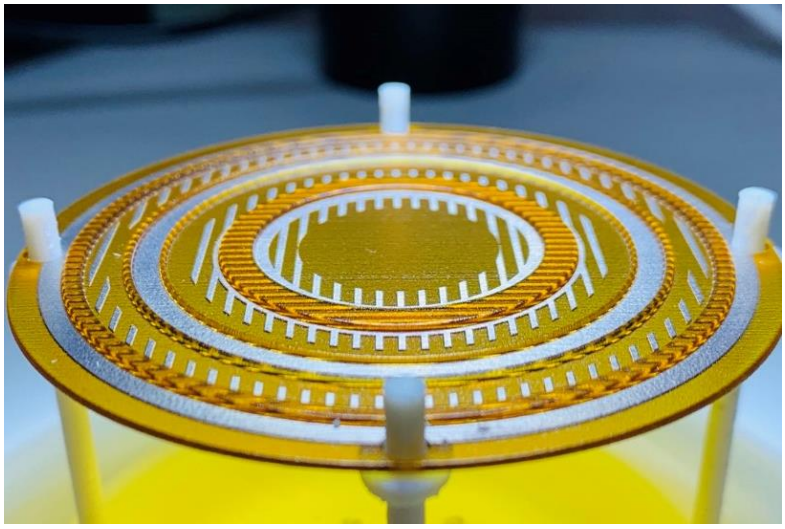

(a)

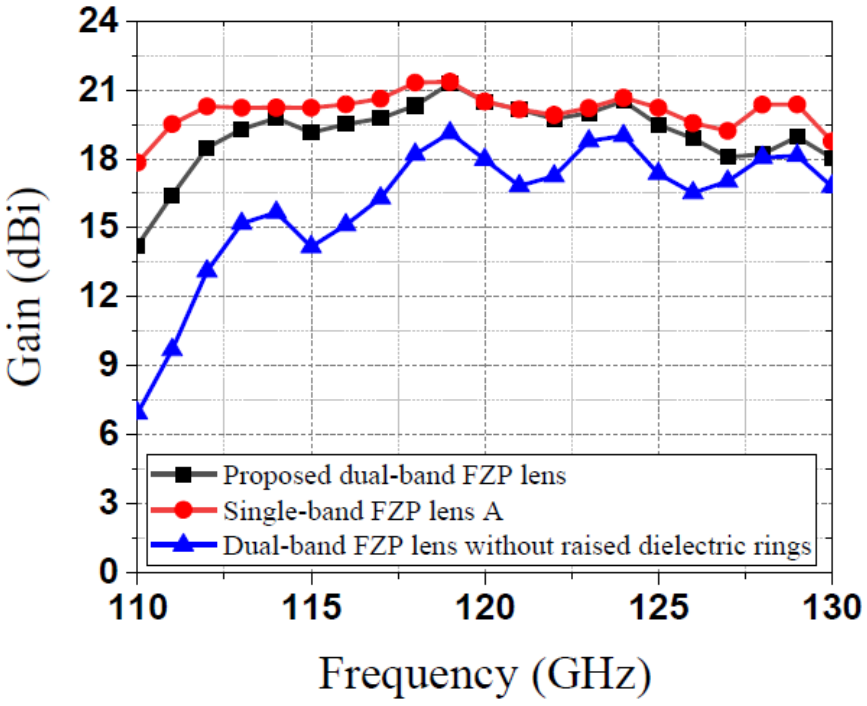

(b)

Fig. 2.13. (a) Photographs of the 3D-printed metalens antenna, (b) Boresight gain comparison at high-band [38].

Besides printing multi-layer constructions, AME enables fabricating of non-planar electronic models. In [38], a shared-aperture dual-band Fresnel zone plate (FZP) metalens antenna operating at 75GHz and 120 GHz is proposed and experimentally verified. The concentric rings of two FZP metalens antennas made of different grid polarizers merge seamlessly, forming the dual-band FZP metalens antenna in a shared aperture, as shown in Fig. 2.13(a). Fig. 2.13(b) illustrates the gain of the dual-band FZP with/without raised dielectric rings. After adding the phase compensating rings, the sidelobe levels of the radiation patterns were improved from -6 dB to -12 dB. Meanwhile, after adding the phase compensating rings, the boresight gain was improved by 2.4 dB at 120-GHz. Furthermore, the raised dielectric rings improve the realized gain of the higher working band. Finally, high directional radiation is achieved at two bands with measured peak gains of 20.3 dBi and 21.9 dBi at 75 GHz and 120 GHz, respectively. The proposed FZP metalens antenna has the merits of a lightweight and low profile, and it was fast-prototyped using a conductive/dielectric integrated AME technique. Potential applications of the FZP metalens antenna include multi-band mm-wave/terahertz communications, sensing, and imaging.

2.4 Conclusion

In summary, an overview of a series of additively manufactured (AM) microwave components and devices from single-material to multi-material processes has been presented in this chapter. According to the open literatures, the fabrication of conductive and dielectric materials simultaneously is very challenging if we use the 3D printing technology to fabricate electronic devices. For example, as mentioned above, plating metal on 3D- printed dielectric models will add additional machining steps and reduce the manufacturing accuracy, especially for the complex electronic devices with multi-layer structures. Therefore, finding a perfect multi-material 3D printing technology and applying it to the fabrication of complex electronic devices will contribute to the development of AM microwave circuit designs.

In this thesis, we proposed a new group of electronic devices with good

performances, compact size, and multilayer structures, including transmission lines, bandpass filters, couplers, and metasurfaces. Taking advantage of the multi-material AM technology, complex microwave devices are achieved with exceptional performance. Undoubtedly, multi-material AM technologies will play a significant role in microwave component design, from the microwave to the terahertz regimes.

2.5 References

[1] J. Kwon, Y. Takeda, R. Shiwaku, S. Tokito, K. Cho and S. Jung, “Three-dimensional monolithic integration in flexible printed organic transistors,” *Nat. Commun*., vol. 10, no. 54, pp. 1-10, Jan. 2019.

[2] N. Karim, S. Afroj, S. Tan, K. S. Novoselov, and S. G. Yeates, “Three-dimensional monolithic integration in flexible printed organic transistors,” *Sci. Rep.,* vol. 9, no. 8035, pp. 1-10, May 2019.

[3] H. Yoo, H. Park, S. Yoo, S. On, H. Seong, S. G. Im and J.-J. Kim, “Highly stacked 3D organic integrated circuits with via-hole-less multilevel metal interconnects,” *Nat. Commun*., vol. 10, no. 2424, pp. 1-10, May. 2019.

[4] A. Massaccesi, P. Pirinoli, V. Bertana, G. Scordo; S. L. Marasso, M. Cocuzza and G. Dassano, “3D-printable dielectric transmitarray with enhanced bandwidth at millimeter-waves,” *IEEE Access*, vol. 6, pp. 46407-46418, 2018.

[5] X. Liu, L. Peng, Y. Liu, W. Yu, Q. Zhao, X. Jiang, S. Li, and C. Ruan., “Ultra-broadband all dielectric transmitarray designing based on genetic algorithm optimization and 3D print technology,” *IEEE Trans. Antennas Propag.*, vol. 69, no. 4, pp. 2003-2012, April 2021.

[6] G. Huang, C. Han, W. Xu, T. Yuan and X. Zhang, “A compact 16-way high-power combiner implemented via 3-D metal printing technique for advanced radio-frequency electronics system applications,” *IEEE Trans. Ind. Electron*., vol. 66, no. 6, pp. 4767-4776, Jun. 2019.

[7] G. L. Huang, S. G. Zhou, and T. Yuan, “Design of a compact wideband feed cluster with dual-polarized sum- and difference-patterns implemented via 3-D metal printing,” *IEEE Trans. Ind. Electron.,* vol. 65, no. 9, pp. 7353–7362, Sep. 2018.

[8] J. Zhu, Y. Yang, D. McGloin, R. R. Unnithan, S. Li, S. Liao, and Q. Xue, “3-D printed planar dielectric linear-to-circular polarization conversion and beam shaping lenses using coding polarizer,” *IEEE Trans. Antennas Propag*., vol. 68, no. 6, pp. 4332-4343, June 2020.

[9] G. B. Wu, Y. S. Zeng, K. F. Chan, S. W. Qu and C. H. Chan, "3-D printed circularly polarized modified Fresnel lens operating at terahertz frequencies," *IEEE Trans. Antennas Propag.,* vol. 67, no. 7, pp. 4429-4437, July 2019.

[10] G. B. Wu, K. F. Chan and C. H. Chan, "3-D printed terahertz lens to generate higher order bessel beams carrying OAM," *IEEE Trans. Antennas Propag*., vol. 69, no. 6, pp. 3399-3408, June 2021.

[11] H. Yi, S. Qu, K. Ng, C. H. Chan and X. Bai, "3-D printed millimeter-wave and terahertz lenses with fixed and frequency scanned beam," *IEEE Trans. Antennas Propag*., vol. 64, no. 2, pp. 442-449, Feb. 2016.

[12] M. D. Wu, B. Li, Y. zhou, D. L.Guo, Y. Liu, F. Wei and X. Lv, "Design and measurement of a 220 GHz wideband 3-D printed dielectric reflectarray," *IEEE Antennas Wirel. Propag. Lett.*, vol. 17, no. 11, pp. 2094-2098, Nov. 2018.

[13] J. H. Barton, C. R. Garcia, E. A. Berry, R. Salas and R. C. Rumpf, "3-D printed all-dielectric frequency selective surface with large bandwidth and field of view," *IEEE Trans. Antennas Propag*., vol. 63, no. 3, pp. 1032-1039, March 2015.

[14] A. Shastri, B. Sanz-Izquierdo, E. A. Parker, S. Gao, P. Reynaert, Z. Chen and L. Winchester, "3D Printing of millimetre wave and low-terahertz frequency selective surfaces using aerosol jet technology," *IEEE Access*, vol. 8, pp. 177341-177350, 2020.

[15] A. Chauraya, W.G. Whittow, and J.C. Vardaxoglou, Y. Li, R.Torah, K. Yang, S. Beeby, and J. Tudor*,* "Inkjet printed dipole antennas on textiles for wearable communications," *IEEE Microw. Antennas Propag.,* vol. 7, no. 9, pp. 760–767, Apr. 2013.

[16] S. Kim, Y. Ren, H. Lee, A. Rida, S. Nikolaou and M. M. Tentzeris, "Monopole antenna with inkjet-printed EBG array on paper substrate for wearable applications," *IEEE Antennas Wirel. Propag. Lett.,* vol. 11, pp. 663–666, Jun. 2012.

[17] B. S. Cook, and A. Shamim, "Inkjet printing of novel wideband and high gain antennas on low-cost paper substrate," *IEEE Trans. Antennas Propag.,* vol. 60, no. 9, pp. 4148–4156, Sep. 2012.

[18] S. Moscato, R. Bahr, and T. Le *et al.*, "Infill-dependent 3-D-printed material based on ninjaFlex filament for antenna applications" *IEEE Antennas Wirel. Propag. Lett.,* vol. 15, pp. 1506–1509, 2016.

[19] X. Yu, M. Liang, and C. Shemelya *et al.*, "3-D printed parts for a multi-layer phased array antenna system," *IEEE Antennas Wirel. Propag. Lett.,* vol. 17, no. 11 pp. 2150–2154, Nov. 2018.

[20] R. Colella, A. Michel and L. Catarinucci, "Compact 3-D-printed circularly polarized antenna for handheld UHF RFID readers," *IEEE Antennas Wirel. Propag. Lett.,* vol. 17, no. 11, pp. 2021-2025, Nov. 2018.

[21] S. Wang, L. Zhu, Y. Li, G. Zhang, J. Yang, J. Wang and W. Wu, "Radar cross-section reduction of helical antenna by replacing metal with 3-D printed zirconia ceramic," *IEEE Antennas Wirel. Propag. Lett.,* vol. 19, no. 2, pp. 350-354, Feb. 2020.

[22] G. L. Huang, S. G. Zhou, and T. H. Chio, "Highly-efficient self-compact monopulse antenna system with integrated comparator network for RF industrial applications," *IEEE Trans. Ind. Electron*., vol. 64, no. 1, pp. 674–681, Jan. 2017.

[23] C. Gu, S. Gao, V. Fusco, G. Gibbons et al. "A D-band 3D-printed antenna," *IEEE Trans. Terahertz Science and Tech.*, vol. 10, no. 5, pp. 433-442, Sept. 2020.

[24] C. Guo, J. Li, Y. Yu, F. Zhang, Y. Zhu, Q. Yang, W. Zhu, S. Zhu, X. Shang, Y. Gao, Y. Wang, G.-L. Huang, Q. S. Cheng and A. Zhang, "A 3-D printed E -plane waveguide magic-T using air-filled coax-to-waveguide transitions," *IEEE Trans. Microw. Theory Techn.,* vol. 67, no. 12, pp. 4984-4994, Dec. 2019.

[25] Y. Chen, G. Zhang, J. Hong, Z. Sun, J. Yang, and W. Tang, "3-D printed dual-band filter based on spherical dual-mode cavity," *IEEE Microwave Wireless Comp. Lett.,* vol. 31, no. 9, pp. 1047 – 1050, Sep. 2021.

[26] D. Zhou, X. Huang and Z. Du, "Analysis and design of multilayered broadband radar absorbing metamaterial using the 3-D printing technology-based method," *IEEE Antennas Wirel. Propag. Lett.,* vol. 16, pp. 133-136, 2017.

[27] C. R. Garcia, J. Correa, D. Espalin, J. H. Barton, R. C. Rumpf, R. Wicker, and V. Gonzalez, "3D printing of anisotropic metamaterials," *Progress Electromagnetics Research Lett.*, vol. 34, pp. 75-82, 2012.

[28] C. Casarini, B. Tiller, C. Mineo, C. N. Macleod, J. F. C. Windmill and J. C. Jackson, "Enhancing the sound absorption of small-scale 3-D printed acoustic metamaterials based on helmholtz resonators," *IEEE Sensors Journal*, vol. 18, no. 19, pp. 7949-7955, 1 Oct.1, 2018.

[29] S. Ghosh and S. Lim, "Perforated lightweight broadband metamaterial absorber based on 3-D printed honeycomb," *IEEE Antennas Wirel. Propag. Lett.*, vol. 17, no. 12, pp. 2379-2383, Dec. 2018.

[30] C. Casarini, V. Romero-García, J. Groby, B. Tiller, J. F. C. Windmill and J. C. Jackson, "Fabrication and characterization of 3D printed thin plates for acoustic metamaterials applications," *IEEE Sensors Journal*, vol. 19, no. 22, pp. 10365-10372, 15 Nov., 2019.

[31] E. Dogan, A. Bhusal, B. Cecen, A. K. Miri, "3D printing metamaterials towards tissue engineering," *Applied Materials Today*, vol. 20, 2020.

[32] M. Kadic, G. W. Milton, M. v. Hecke and M. Wegener "3D metamaterials." *Nat Rev Phys*, Vol. 1, pp. 198–210, 2019.

[33] M. Li, Y. Yang, F. Iacopi, M. Yamada and J. Nulman, "Compact multi-layer bandpass filter using low-temperature additive manufacturing solution," *IEEE Trans. Electron. Devices*, vol. 68, no. 7, pp. 3163-3169, July 2021.

[34] A. Vallecchi, D. Cadman, W. G. Whittow, J. Vardaxoglou, E. Shamonina and C. J. Stevens, "3-D printed bandpass filters with coupled vertically extruded split ring resonators," *IEEE Trans. Microw. Theory Techn.,* vol. 67, no. 11, pp. 4341-4352, Nov. 2019.

[35] M. Li, Y. Yang, Y. Zhang, F. Iacopi, S. Ram and J. Nulman, "A Fully integrated conductive and dielectric additive manufacturing technology for microwave circuits and antennas," *50th European Microwave Conference (EuMC),* Utrecht, Netherlands, 2021, pp. 392-395, doi: 10.23919/EuMC48046.2021.9338141.

[36] F. Cai, Y. Chang, K. Wang, C. Zhang, B. Wang and J. Papapolymerou, "Low-loss 3-D multi-layer transmission lines and interconnects fabricated by additive manufacturing technologies," *IEEE Trans. Microw. Theory Techn.,* vol. 64, no. 10, pp. 3208–3216, Oct. 2016.

[37] M. Li, Y. Yang, F. Iacopi, J. Nulman and S. Chappel-Ram, "3D-printed low-profile single-substrate multi-metal layer antennas and array with bandwidth enhancement," *IEEE Access,* vol. 8, pp. 217370-217379, 2020.

[38] J. Zhu, Y. Yang, M. Li; D. McGloin, S. Liao, J. Nulman, M. Yamada and F. Iacopi., "Additively manufactured millimeter-wave dual-band single-polarization shared aperture Fresnel zone plate metalens antenna," *IEEE Trans. Antennas Propag*., vol. 69, no. 10, pp. 6261 – 6272, Oct. 2021.

[39] H.-N. Morales-Lovera, J.-L. Olvera-Cervantes, A. Corona-Chavez and T. K. Kataria, "Dielectric characterization of anisotropic 3D-printed biodegradable substrates based on polylactic acid [Application Notes]," *IEEE Microw. Magazine,* vol. 22, no. 9, pp. 18-100, Sept. 2021.

[40] A. C Paolella, C. Corey, D. Foster, J. Desjardins, C. Smith and L. Walters, "Broadband millimeter wave characterization of 3-D printed materials," *2018 IEEE/MTT-S International Microwave Symposium - IMS*, 2018, pp. 1565-1568.

[41] A. C. Paolella, C. D. Fisher, C. Corey, D. Foster and D. Silva-Saez, "3-D printed millimeter-wave lens systems at 39 GHz," *IEEE Microwave Wireless Comp. Lett.,* vol. 28, no. 6, pp. 464-466, June 2018.

[42] C. Guo, X. Shang, J. Li, F. Zhang, M. J. Lancaster and J. Xu, "A lightweight 3-D printed X-Band bandpass filter based on spherical dual-mode resonators," *IEEE Microwave Wireless Comp. Lett.,* vol. 26, no. 8, pp. 568-570, Aug. 2016.

[43] C. Guo, X. Shang, M. J. Lancaster and J. Xu, "A 3-D printed lightweight X-Band waveguide filter based on spherical resonators," *IEEE Microwave Wireless Comp. Lett.,* vol. 25, no. 7, pp. 442-444, July 2015.

[44] E. López-Oliver, C. Tomassoni, L. Silvestri, M. Bozzi, L. Perregrini, S. Marconi, G. Alaimo and F. Auricchio, "3-D-Printed compact bandpass filters based on conical posts," *IEEE Trans. Microw. Theory Techn.,* vol. 69, no. 1, pp. 616-628, Jan. 2021.

[45] G. Venanzoni, C. Tomassoni, M. Dionigi, M. Mongiardo and R. Sorrentino, "Design and fabrication of 3-D printed inline coaxial filters with improved stopband," *IEEE Trans. Microw. Theory Techn.,* vol. 68, no. 7, pp. 2633-2643, July 2020

Chapter 3 3D-Printed Low-Profile Single-Substrate Multi-Metal Layer Antennas and Array with Bandwidth Enhancement

3.1 Introduction

Additive manufacturing (AM) is a potential game-changer that may completely revamp the manufacturing value chain in Industry 4.0. In the electronics industry, AM technology has the advantages of low cost, fast prototyping, three-dimensional (3D) customized design freedom, and a distributed production circle. 3D printing is an alternative method to replace or complement traditional fabrication. Many complex systems, which are difficult to implement using conventional fabrication methods, can be prototyped and realized.

According to the open literature, 3D-printed electronic components have been achieved in certain types of waveguides [1], reflectarrays [2-3], lenses [4], transmitarray [5], frequency selective surfaces [6-7], transmission lines (TLs) [8-9], filters [10], and antennas [11-41]. Most of these applied AM approaches are based on printing the entire geometry with a single material printer, such as metal/dielectric 3D printers [1-2], or loading metallic paint with metal casting 3D printers on different kinds of substrates, for example, textiles [11] or papers [12], [14]. It is often difficult to utilize these single-material printing processes to handle advanced designs with complex structures composed of conductive and dielectric parts in a single substrate. Particularly challenging when the high-conductive and dielectric materials need to be fully integrated using a single-substrate 3D printer, which often requires more steps and additional processing time during fabrication [16]. Moreover, it is difficult to fabricate multi-layer structures using conventional single-material AM technology [17]. Fortunately, recent advances in AM technology have produced a new generation of 3D printing techniques and materials that can fabricate conductor and dielectric

simultaneously [9-10], [42-43].

In this chapter, two types of TLs are investigated to understand the electrical characteristics of the 3D printing materials. Then, multi-metal layer patch antennas and antenna arrays with ultralow profile and broad operational band are proposed. Multi-metal layers are seamlessly printed in a single substrate with additive manufacturing electronics (AME) solution to excite additional resonate modes that can be controlled independently. With the increase of stacked patches, the impedance bandwidth can rise from 5.9% (single layer) to 10.6% (three layers) and 83% (seven layers), respectively, without increasing the total profile of the antenna. Finally, a linear polarized (LP) antenna array and a circular polarization (CP) antenna array are demonstrated. The fabricated prototypes verify that multilayer antennas can be easily achieved in a 3D printed single PCB substrate (thickness less than 3 mm) with a low profile and versatile antenna performance. According to the open literature, the proposed designs are believed to be one of the lowest profiled patch antennas, with wideband performance.

3.2 Fabrication Technology and Materials

3.2.1 Multi-Material Additively Manufactured Electronics Solution

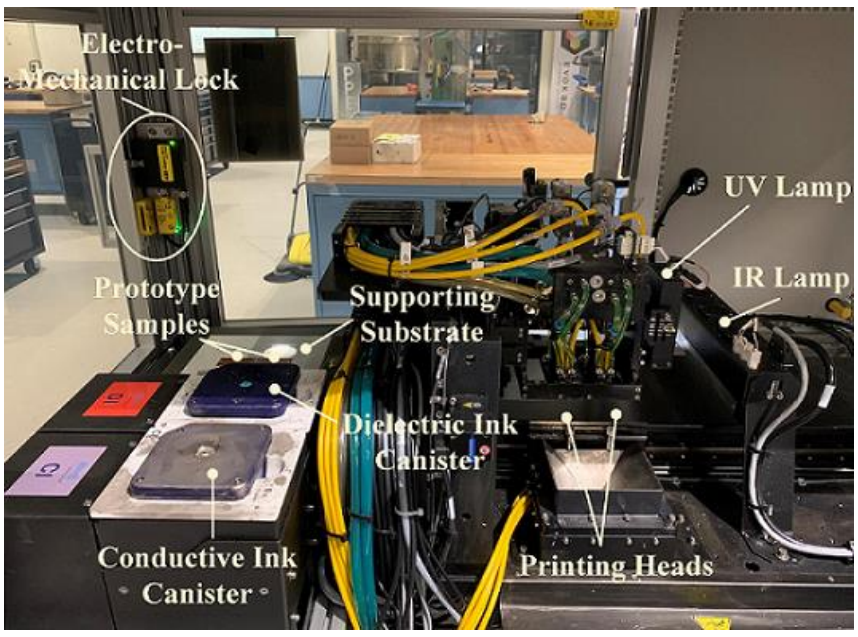

Fig. 3.1. 3D printing system using fully integrated dielectric and conductive inks.

This section presents novel single-substrate wideband antennas, and arrays with ultralow profiles and introduces an AME method for fabricating these multilayer models. Taking advantage of the AME method, multi-metal layers can be seamlessly printed in a single substrate to excite additional resonant modes that can be controlled independently. With the increase of stacked patches, the impedance bandwidth can rise from 5.9% (single layer) to 10.6% (three layers) and 83% (seven layers), respectively, without increasing the total profile of the antenna. Furthermore, taking advantage of AME, the feeding network is integrated into the antenna array elements' substrate without increasing the array's size and profile. The electrical properties of this 3D printing material are investigated at 3.6 GHz using an embedded transmission line (TL). Then, a three-layer LP antenna element and a 2×2 LP array are seamlessly printed into single-substrate, respectively. Furthermore, the multi-layer CP antennas are investigated for wide impedance bandwidth and 3-dB ratio axial by stacking patches in a single thin substrate. According to the open literature, the proposed designs are believed to be one of the lowest profiled patch antennas, with wideband performance.

3.2.2 Measurement of the complex permittivity

Dielectric properties of materials play an essential role in the design of 3D printing devices. The company provided the dielectric constant and loss tangent of the acrylates used by the 3D printing system from 1-20 GHz. It is observed in Fig. 3.2 that the dielectric constant is around 2.8 from 1 to 20 GHz. Meanwhile, the loss tangent is around 0.013.

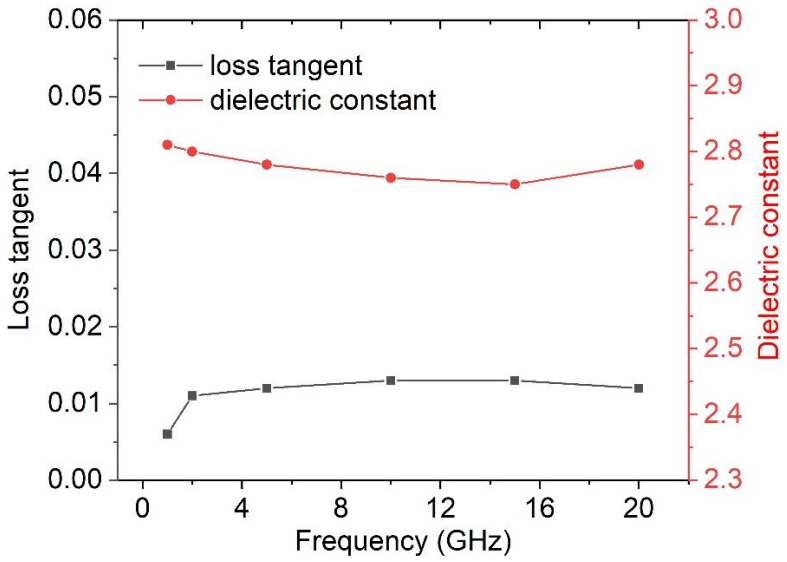

Fig. 3.2. Dielectric constant and loss tangent response of the updated acrylates used by the fully integrated additive manufacturing approach.

For measuring the complex permittivity of 3D printing material at higher operational bands, considering its low loss, the cavity resonant method with the highest possible accuracy of measurement is employed [44], which is categorized as the closed-cavity method and open-cavity method. The former method is mainly used in the centimeter-wave band, and the cavity includes coaxial cavity [45], cylindrical cavity [46], rectangular cavity [47], etc. For the millimeter-wave band, the closed-cavity needs to be designed with a smaller size to reduce interference modes, which leads to low cavity quality factor and difficult sample processing. Compared to the closed-cavity, the open-cavity represented by the quasi-optical cavity can maintain a very high-quality factor because there is no conductor loss from the metal side-wall. Moreover, the fundamental modes in the cavity are easily captured, and the sample size is moderate, making the widespread use of quasi-optical cavity in millimeter-wave band possible.

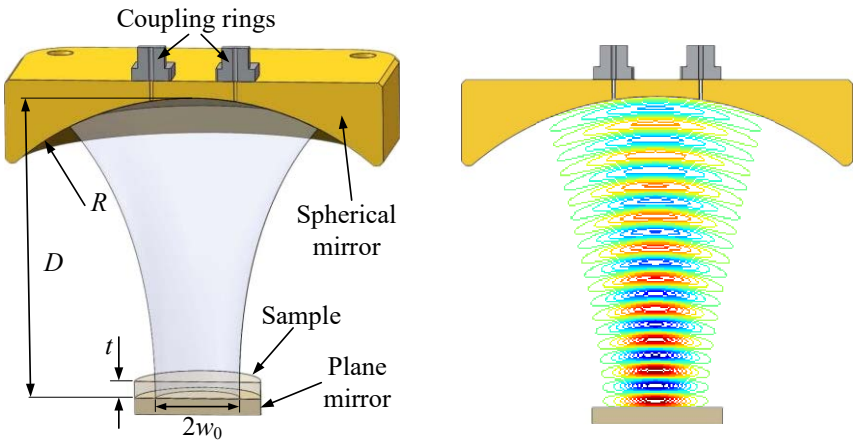

Fig. 3.3 Sectional drawing (a) and fundamental mode field distribution (b) of a semi-symmetric quasi-optical cavity.

Fig. 3.3(a) is the schematic diagram of a semi-symmetric quasi-optical cavity composed of a spherical mirror and a plane mirror. The plane mirror is usually a circular metal platform, which can move along the axis for adjusting the cavity length D. The spherical mirror has a curvature radius of R, and two coupling rings connected with the vector network analyzer (VNA) are symmetrically located in the middle of the mirror.

Under the paraxial approximation, the field distribution in the cavity exists in the form of the Gaussian beam, which is the quasi-TEMplq wave. For the empty cavity, resonance occurs when D satisfies the following conditions [48].

$$f_0 = \frac{c}{2D}\left[(q+1) + \frac{2p+l+1}{\pi}\arctan\sqrt{D/(R-D)}\right] \tag{3-1}$$

where f_0 is the cavity resonant frequency, p, l and q represent the radial, angular, and longitudinal modes, respectively. Among the different modes, the fundamental mode TEM_{00q} mode is the most suitable as the operating mode due to its concentrated electromagnetic energy distribution, as shown in Fig. 3.3(b).

When a sheet sample is loaded on the plane mirror, the cavity's resonant frequency and quality factor will change. The relative permittivity ε_r' of the sample can be solved by the following transcendental equation [48]:

$$\frac{1}{\sqrt{\varepsilon_r'}}\tan\left(\sqrt{\varepsilon_r'}kt - \varphi_t\right) = -\tan\left(kd - \varphi_d\right) \tag{3-2}$$

with

$$d = D - t \tag{3-3}$$

$$\varphi_t = \arctan\left(\frac{t}{\sqrt{\varepsilon_r'}z_0}\right) \tag{3-4}$$

$$\varphi_d = \arctan\left(\frac{d''}{z_0}\right) - \arctan\left(\frac{t}{\varepsilon_r' z_0}\right) \tag{3-5}$$

$$z_0 = \sqrt{d''\left(R - d''\right)} \tag{3-6}$$

$$d'' = d + t/\varepsilon_r' \tag{3-7}$$

where k=2π/λ is the wave number, t is the thickness of the sample.

The loss tangent tanδ of the sample is solved according to the change in the cavity quality factor before and after loading the sample, which is given by [31]:

$$\tan\delta = \frac{1}{Q_e}\frac{t\Delta + d}{t\Delta + \frac{1}{2k}\sin 2\left(kd - \varphi_d\right)} \tag{3-8}$$

with

$$\Delta = \frac{\varepsilon_r'}{\varepsilon_r'\cos^2\left(\sqrt{\varepsilon_r'}kt - \varphi_t\right) + \sin^2\left(\sqrt{\varepsilon_r'}kt - \varphi_t\right)} \tag{3-9}$$

$$\frac{1}{Q_e} = \frac{1}{Q_d} - \frac{1}{Q_0}\frac{D\left(\Delta + 1\right)}{2\left(t\Delta + d\right)} \tag{3-10}$$

where Q_0 and Q_d are the quality factors of the empty and loaded cavities, respectively. These quality factors can be characterized as the resonance frequency divided by the bandwidth under the empty and loaded cavity condition, respectively.

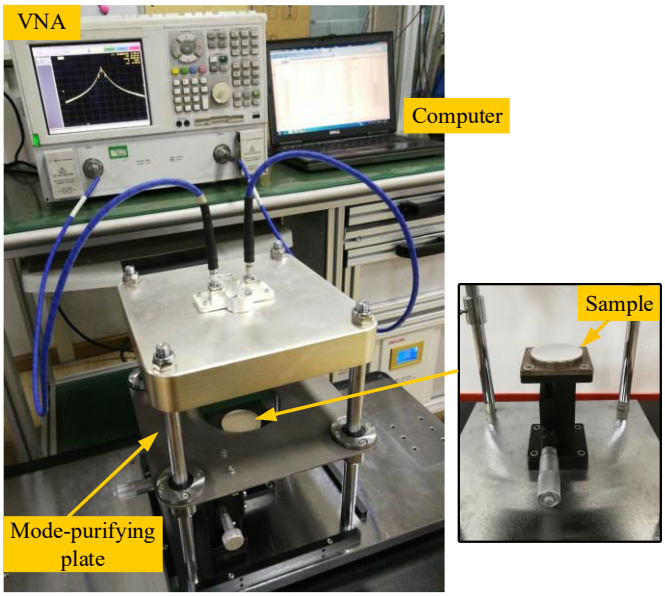

Fig. 3.4. Photograph of a quasi-optical cavity test system.

The quasi-optical cavity test system used in this thesis is shown in Fig. 3.4. The curvature radius and the aperture diameter of the spherical mirror are 180 mm and 220 mm, respectively. The diameter of the plane mirror is 50 mm, which is greater than the waist diameter of the fundamental modes. The coupling ring is adjustable in insertion depth, so the desired coupling corresponding to different frequency bands can be obtained. In order to suppress the non-TEM_{00q} interference modes, a mode-purifying plate with a hole in the middle is placed between two mirrors, as shown in Fig. 3.4. The plate is adjustable in height and sprayed with the absorbing coating for absorbing the interference mode without affecting the fundamental mode significantly.

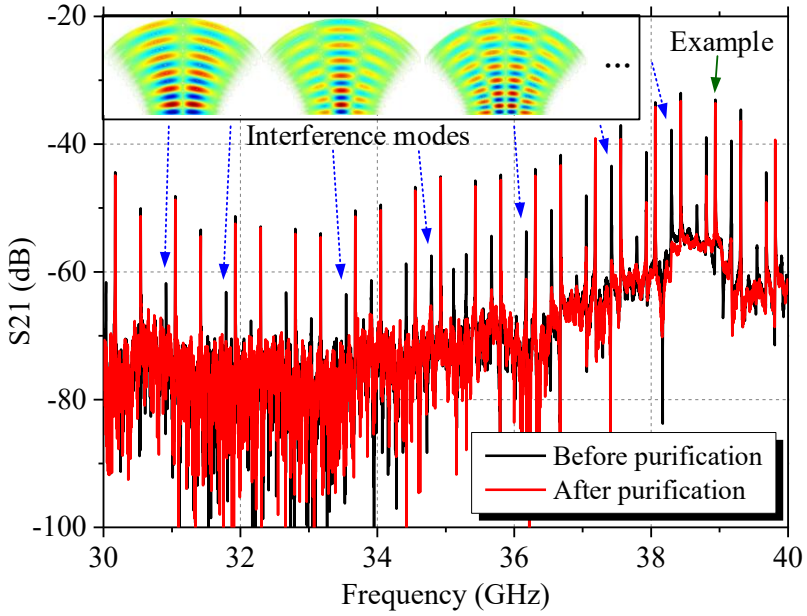

Fig. 3.5 Resonant peaks distribution of the quasi-optical cavity in the band of 30-40 GHz.

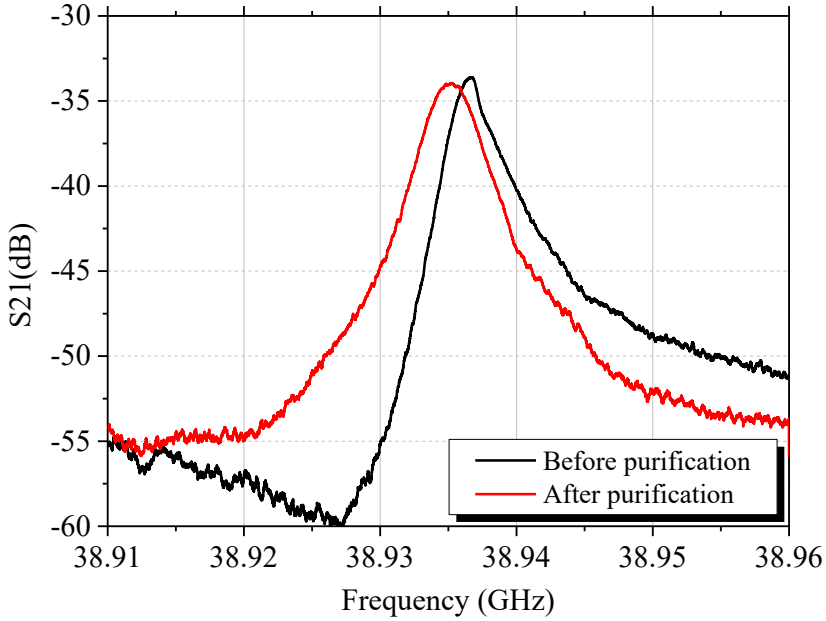

Fig. 3.6 A typical example of the resonant peak.

The measurement is based on Agilent E8363B vector network analyzer (VNA). The distribution of the resonant peaks in the band of 30-40 GHz is shown in Fig. 3.5. A typical example of the resonant peak is given in Fig. 3.6. It can be seen that the interference modes are effectively suppressed after introducing the mode-purifying plate. Some resonant peaks obtain better symmetry, which helps to improve the stability

and accuracy of the measurement.

3.2.3 Electrical Characteristics of Dielectric Materials

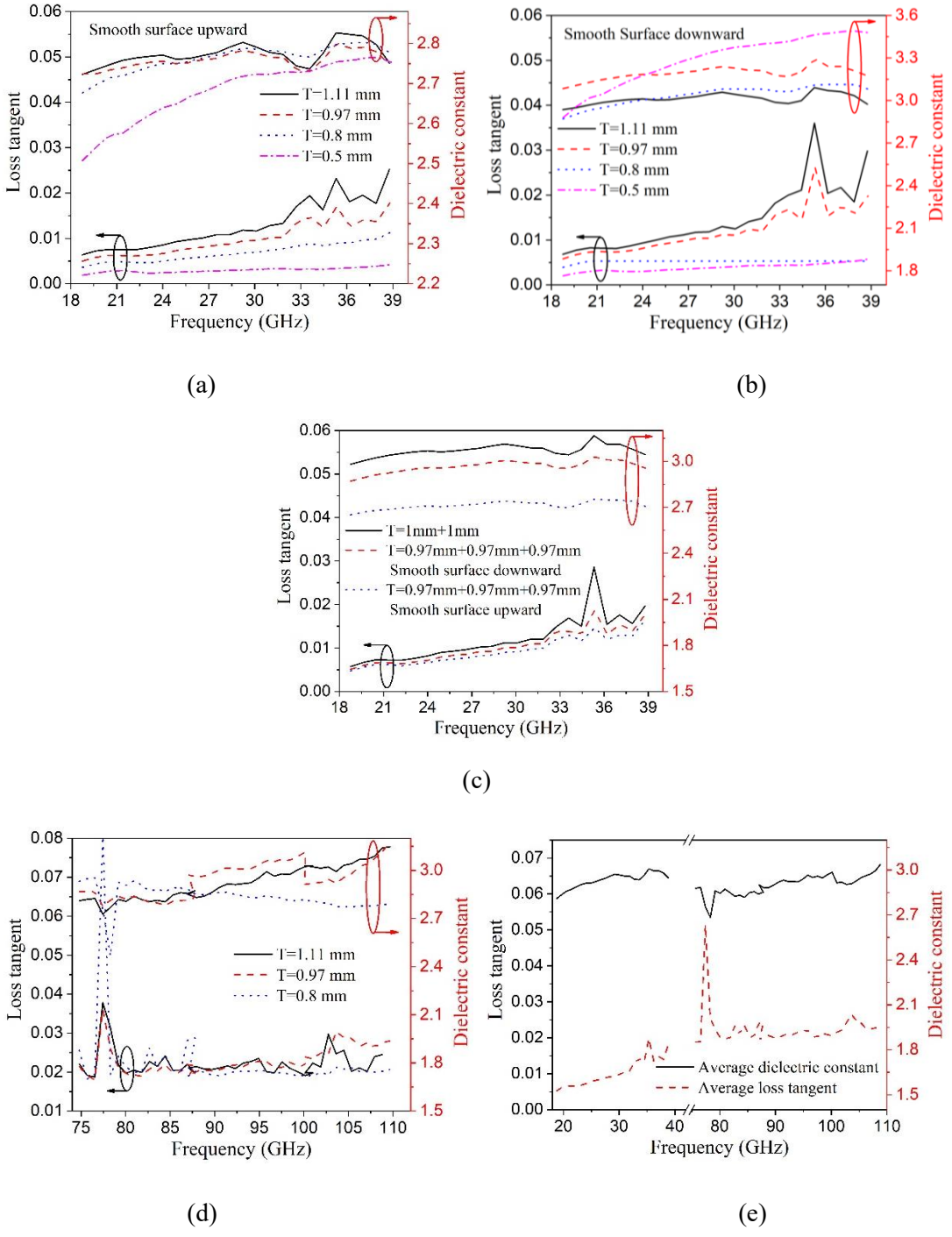

Fig. 3.7. Complex permittivity of the acrylates samples used by the 3D printing system with different thicknesses T under the conditions of (a) the smoother surface upward and (b) downward, and (c) the complex permittivity of the multi-stacked acrylates samples operating

from 18 to 40 GHz. (d) The complex permittivity of the acrylates samples with different thicknesses T is operating from 74 to 108 GHz. (e) The average complex permittivity of the acrylates samples in 18 to 40 and 74 to 108 GHz.

Fig. 3.7 gives the measured dielectric constant and loss tangent of the 3D printing acrylates material used by this system. The sample has the same diameter as the plane mirror. Due to gravity, the bottom surface of the sample in contact with the platform is smoother than the upper surface of the sample. The samples with smoother surface to upward and downward are measured from 18 to 40 GHz, respectively. For the 3D printing material under test in this study, the temperature is set as 28 °C. Figs. 3.7(a) and (b) shows the dielectric constant and loss tangent of the samples with different thickness T under smooth surface upward and downward conditions, respectively. With the increase of operating frequency, the dielectric constant and loss tangent rise slightly. When the smooth surface is upward, the dielectric constant of samples with different T is almost kept unchanged besides T = 0.5 mm, which is thinner than the other samples. The loss tangent of the samples is developed with the increase of the thickness. When the smooth surface is downward, dielectric constants of samples with different T become varied and more significant than those under the condition of the smooth surface being upward. The loss tangent of samples with a smooth surface is downward is more significant than the smooth surface is upward.

To further investigate the material's complex permittivity, multi-samples are stacked together. As shown in Fig. 3.7(c), the dielectric constant of two stacked 1 mm samples is bigger than the one of three stacked 0.97 mm samples with smooth surfaces downward or upward, and the loss tangent of three stacked 0.97 mm samples with smooth surfaces downward is bigger than the one with smooth surfaces upward. However, the loss tangent of two stacked 1 mm samples and one of three stacked 0.97 mm samples with smooth surfaces upward or downward are almost equivalent. The electrical characteristics of the acrylates materials up 40 GHz are measured as well. As shown in Fig. 3.7(d), the loss tangent of the samples with different thicknesses T from 0.8 mm to 1.1 mm is about 0.02 during the operational frequency from 74 to 108 GHz,

while the dielectric constant varies from 2.8 to 3.15.

To obtain reliable values of electrical characteristics, the average dielectric constant and loss tangent of the acrylates materials during the operational frequency range of 18 to 40 GHz and 74 to 108 GHz have been calculated and depicted in Fig. 3.7(e). It is evident in Fig. 3.7(e) that the average values of loss tangent and dielectric constant gradually increase from 0.006 to 0.019 and 2.8 to 3.0 with the development of frequency during 18 to 40 GHz, respectively. Meanwhile, in 74 to 108 GHz, the values of average loss tangent increases from 0.02 to 0.026, and the average dielectric constant varies from 2.7 to 3.15.

3.3 Design of 3D-Printed Transmission lines and Low-Profile Single-Substrate Multi-Metal Layer Antennas and Array

3.3.1 3D-Printed Microstrip Transmission Lines

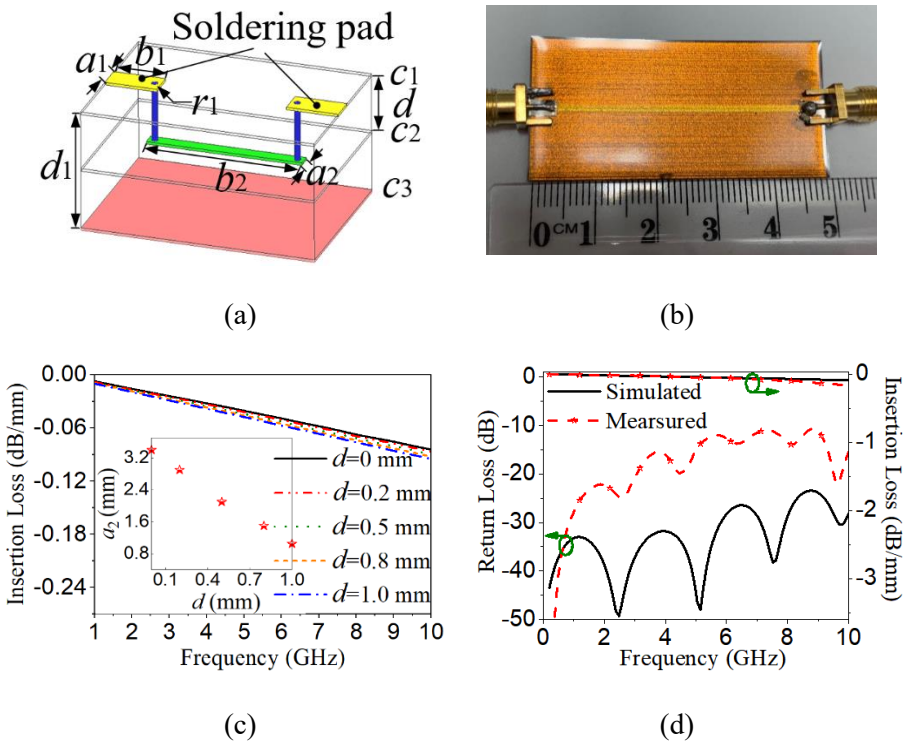

Fig. 3.8. Layout of embedded TL, (b) Photograph of fabricated embedded TL, (c) Transmission coefficients of the embedded TL with varying d; the inset figure shows the values of a2 and d to keep a 50 Ω characteristic impedance. (d) Simulated and measured insertion loss and return

loss for embedded TL. For a_1= 2.6, a_2=1.1, b_1=3, b_2=44, c_1=c_2=c_3 =0.02, d=0.5, d_1= 1, r_1=0.25 (Unit: mm).

To investigate the electrical properties of the 3D printing dielectric materials for loss analysis, an embedded TL with acrylate as the substrate material is analyzed and discussed. As shown in Fig. 3.8(a), the conductive metal for signal transmission is embedded in the dielectric medium, and a_1, a_2, and b_1, b_2 denote the widths and lengths of the surface soldering pad and embedded TL, respectively. In addition, the surface soldering pad and embedded TL are connected by vias, the radius of which is r_1, c_1, c_2, and c_3 are the thicknesses of metal layers, d represents the depth of the transmission line embedded in the acrylate substrate, and d_1 is the thickness of the dielectric substrate. The photograph of the fabricated TL model is depicted in Fig. 3.8(b). As Fig. 3.8(c) shows, the transmission coefficient tends to degrade slightly as the embedded line is pushed into the substrate further away from the top surface. In order to maintain the required impedance match, the embedded TLs are set at 50 Ω, which can be adjusted by the value of a_2, as shown in the inset of Fig. 3.8(c). Finally, a sample with d=1 mm is simulated, fabricated, and measured, as shown in Fig. 3.8(d). The TL printed in the depth of 1.0 mm reveals a maximum insertion loss of 0.03 dB/mm at 3.5 GHz and 0.09 dB/mm at 10 GHz. The differences between simulated and experimental results are due to the connection loss of the SMA connectors, of which the cut-off frequency is lower than 10 GHz.

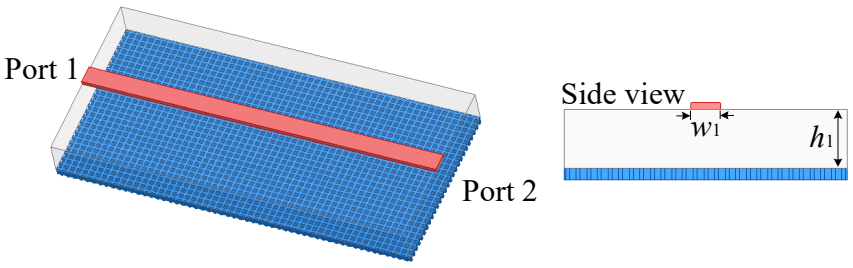

(a)

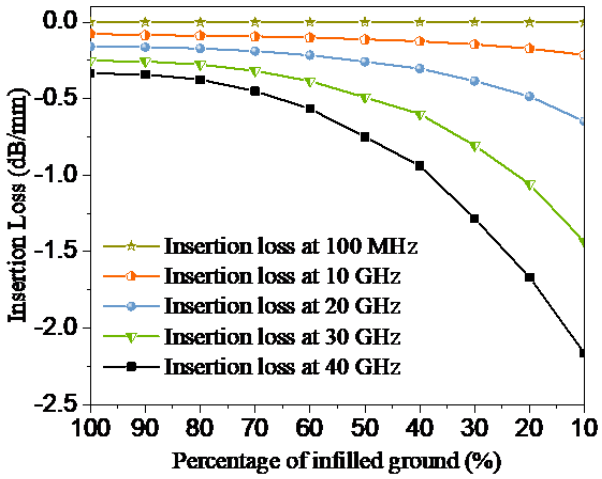

(b)

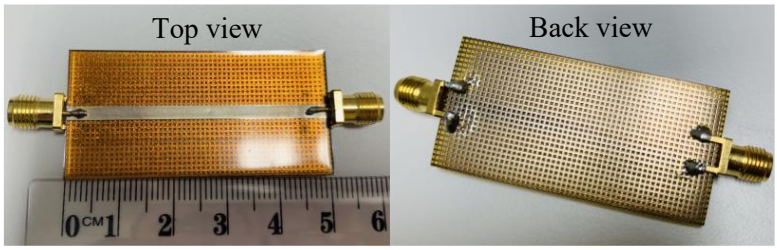

(c)

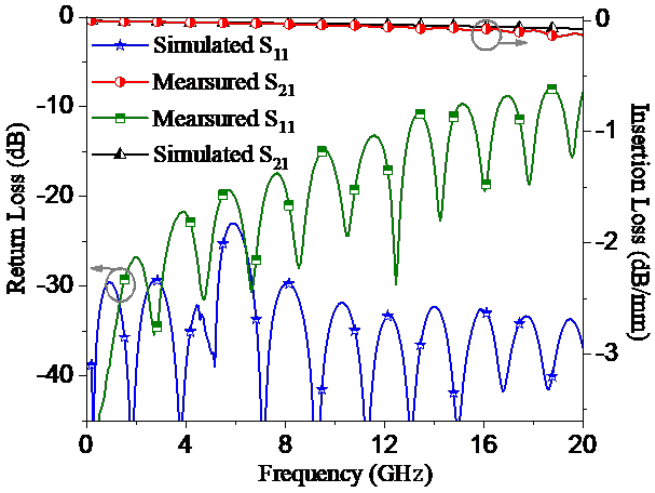

(d)

Fig. 3.9. (a) Construction of infilled-ground transmission line. (b) Simulated insertion loss varied percentage of infilled-ground at different frequencies. (c) Photograph of the infilled-ground transmission line model and its measured results of insertion and return loss. (w_1= 2.6 mm, h_1= 1 mm.)

In additive manufacturing, the cost of the fabrication is mainly dictated by the

consumption of the materials. Replacing a full metallic ground with an infilled one is an appropriate way to reduce the consumption of conductive ink. Therefore, an infilled-ground transmission line is designed, fabricated, and measured. Fig. 3.9(a) depicts the structure of the transmission line with an infilled-ground plane at the bottom. The total dimension of the transmission line is 24 mm × 50 mm× 1 mm with a percentage of infilled-ground. The thickness of each silver layer was set to 20 μm. As shown in Fig. 3.9(b), with the shrinking percentage of infilled-ground, the insertion loss increases gradually versus frequency. Furthermore, with the increase of frequency, the insertion loss resulting from the infilled-ground becomes greater. Therefore, a trade-off between the tolerance of insertion loss and the percentage of infilled-ground should be considered in the design. Finally, the transmission lines are fabricated. Fig. 3.9(c) shows the photographs of the top view and back view of the infilled-ground transmission line. The simulated and measured results are illustrated in Fig. 3.9(d). Good agreement can be achieved between the simulated and measured insertion loss. However, the simulated and measured return loss has some discrepancies, which may result from the connector issues. This situation can be improved by using the high-end SMA connectors with a stable performance up to 20 GHz.

3.3.2 Multi-Layer Linear Polarization Antenna and Antenna Array

3.3.2.1 Multi-layer Linear Polarization Antennas

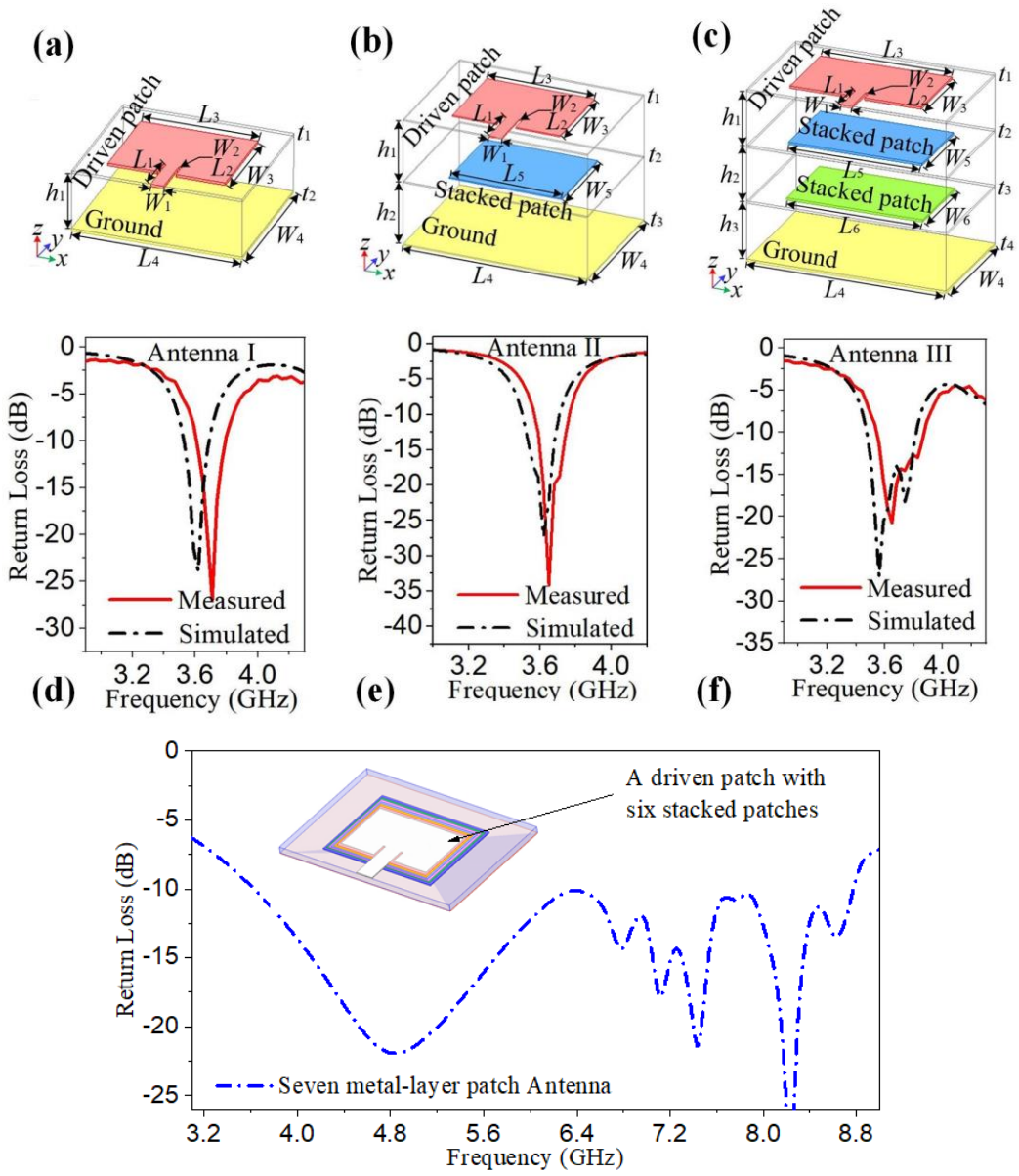

Fig. 3.10. Layouts of (a) Antenna I, (b) Antenna II, (c) Antenna III and the simulated and measured return loss of (d) Antenna I, (e) Antenna II, (f) Antenna. (g) Simulated return loss of seven-layer patch antenna with its layout embedded. (L_1=12, L_2=5, L_3=38, L_4=59, L_5=39, L_6=60, W_1=4.9, W=0.5, W_3=22.6, W_4=36.6, W_5=23.1, W_6=23.3, h_1=0.28, h_2=0.78, h_3=0.36, t_1 = t_2 = t_3 = t_4 = 0.02. (Unit: mm)).

Figs. 3.10(c) demonstrates the layout of Antenna III, which is a three-layer patch antenna consisting of a driven patch and two stacked patches. The analysis of Antenna III is performed with the following three steps:

a. First, a rectangular quarter-wave patch antenna is considered. [Antenna I, Fig. 3.10(a)]. Assume the patch is rectangular in shape with dimensions a and b, The resonance frequency of this quarter-wave patch antenna at the resonant frequencies can be calculated as [49]

$$f_{mn} = \frac{k_{\mathrm{mn}} c}{2\pi\sqrt{\varepsilon_{\mathrm{r}}}} \tag{3-11}$$

where $k_{\mathrm{mn}} = [(m\pi/a)^2 + (n\pi/b)^2]^{1/2}$, ε_{r} is the relative permittivity of the substrate. After optimization, the related parameters are determined and simulated and the measured return loss of Antenna I is given in Fig. 3.10(d).

b. Second, a staked patch is added under the driven patch of Antenna I to construct a double-layer patch antenna (Antenna II, Fig. 3.10(b)). The simulated and measured return loss of Antennas I is given in Fig. 3.10(e). It is noted that an additional resonant mode is introduced by adding the stacked patch.

c. Finally, two staked patches are added under the driven patch, leading to Antenna III [Fig. 3.10(c)]. At this stage, two additional resonant modes are introduced and by varying the value of the widths of patches W_3, W_5 and W_6, the resonate frequencies of Antenna III can be varied independently as shown in Fig. 3.11. Therefore, the final detailed dimensions of the Antenna III are determined after the three designing steps. Compared with Antenna I and II, antenna III has a wider operational band, the total -10 dB bandwidth rises from 5.9% of Antenna I to 10.6% of Antenna III, while the total thickness of the substrate remains unchanged.

Moreover, as shown in Fig. 3.10(g), when the number of stacked patches rises to six, the operational frequency band can increase to 5.14 GHz (3.63-8.77 GHz), achieving a bandwidth of 83%, with a peak gain of 1.45 dBi, while its total thickness remains at 1.5 mm. These results indicate that adding stacked patches generates additional resonant modes to enhance the operational bandwidth, while the total profile of the substrate remains unchanged, taking advantage of multi-mode resonant

characteristics. Fig. 3.10 gives the detailed dimensions of the three-layer patch antenna.

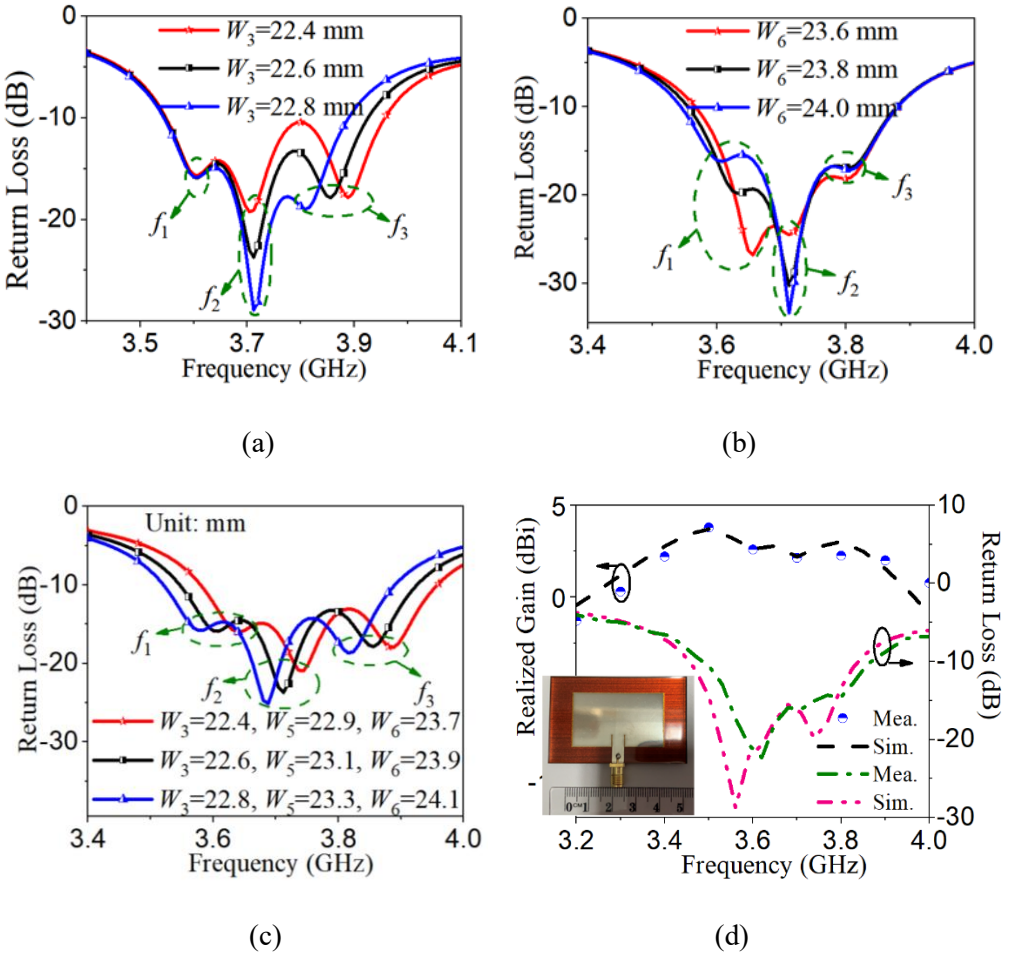

Fig. 3.11. Layouts The bandwidth of three-layer patch antenna varies against (a) W_3, (W_5=23.1, W_6=23.9) (b) W_6, (W_3=22.9, W_5=23.1), (c) W_3, W_5 and W_6 and (d) Measured and simulated gains and return loss of three-layer patch antenna as well as its photograph.

As mentioned above, these resonant modes excited by stacking patches can be adjusted. Taking the three-layer antenna as an example, three resonant modes, f_1, f_2, and f_3, can be independently controlled by tuning the width of driven and stacked patches. Fig. 3.11(a) reveals that, by raising W_3 from 22.4 to 22.8 mm, f_3 can be adjusted to a lower frequency while f_1 and f_2 remain unchanged. Fig. 3.11(b) shows that, by raising W_6 from 23.6 to 24 mm, f_2 and f_3 remain constant, while f_1 decreases gradually. When adjusting the widths W_3, W_5, and W_6, simultaneously, as shown in Fig. 3.11(c), the three resonant modes, f_1, f_2, and f_3 of the antenna can be shifted with a fixed absolute bandwidth. After optimization, Fig. 3.11(d) shows the fabricated three-layer patch

antenna with the antenna gains and return loss in the comparison between simulation and measurement. Good agreement can be obtained between the simulated and measured results. The measured peak gain is 3.8 dBi at 3.5 GHz. The measured return loss lower than -10 dB ranges from 3.5-3.89 GHz.

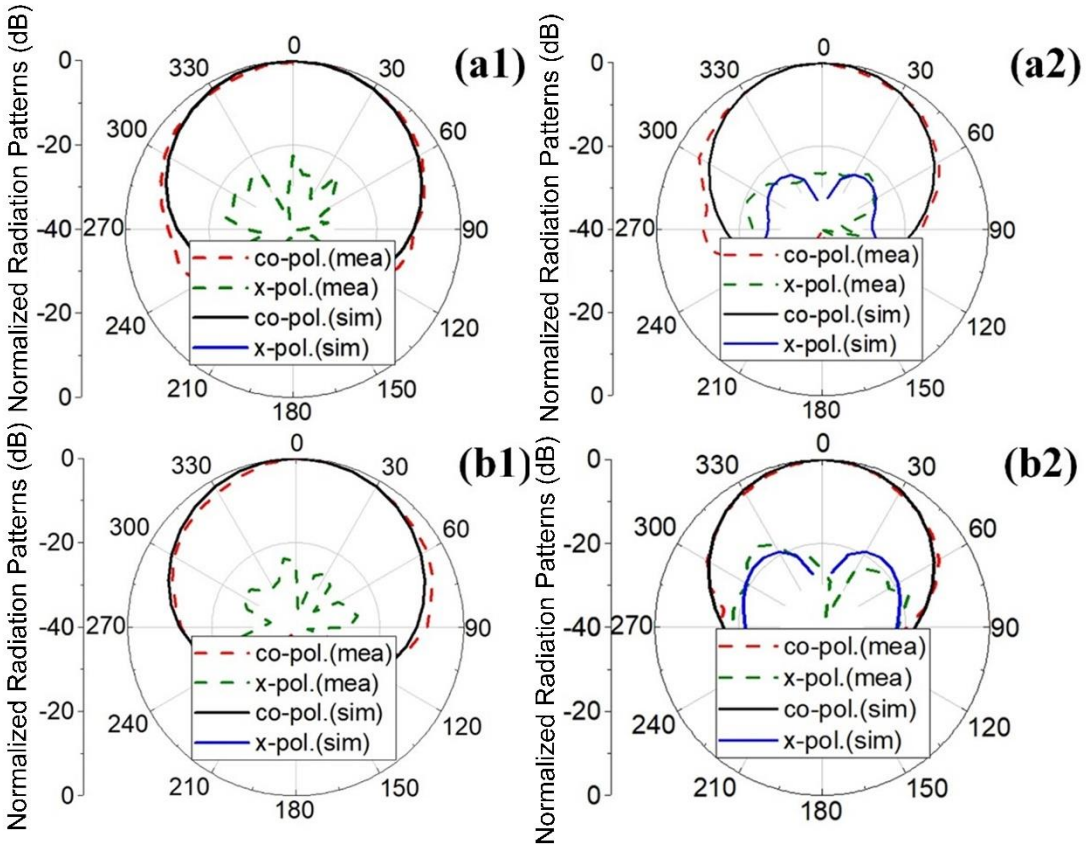

Fig. 3.12. Normalized radiation patterns of Antenna III. (a1) *YOZ*-plane at 3.5 GHz, (a2) *XOZ* -plane at 3.5 GHz, (b1) *YOZ* -plane at 3.6 GHz, (b2) *XOZ* -plane at 3.6 GHz.

In addition, the simulated and measured radiation patterns of Antenna III are presented at 3.5 and 3.6 GHz in the *YOZ*-plane and *XOZ*-plane, respectively, as shown in Fig. 3.12, which shows good matches between simulated and measured results.

Compared with previously reported 3D-printed patch antennas (see Table 3.1), the proposed three-layer antenna can provide wide operational bandwidth with an extremely low-profile. Moreover, since we use an integrated printing approach, no post-processing procedures are needed, which makes the design more reliable and robust.

TABLE 3.1 COMPARISON WITH PREVIOUSLY REPORTED 3D-PRINTED PATCH ANTENNAS

Ref.	Construction	Tan (δ)	ϵ'	$^{*}f_c$ (GHz)	Gain (dBi)	-10 dB bandwidth	Size (λ_g^2)	Thick-ness (λ_g)	Fabricating process

This work	Single element (Three- layer patches)	0.013	2.8	3.68	3.8	10.6%	0.478×0.821	0.031	Dielectric and conductive ink integrated printing
This work	2×2 array	0.013	1	3.63	7.7	12.7%	1.95×1.80	0.041	Dielectric and conductive ink integrated printing
[13]	4×3 array	0.07	35	2.45	0.86	10.1%	7.25×6.28	0.150	Cooper tape +paper for dielectric part
[14]	Single patch	0.02	5.05	2.4	/	3.3%	0.323×0.504	/	Meandered and flexible silicone + copper tape
[15]	Curved single patch	0.015	2.54	2.45	6.28	9%	0.294×0.612	0.129	Curved conductive copper tape + polymer
[16]	1×4 phased array	0.005	2.7	3.5	/	3.7%	1.63×3.685	0.403	Cooper tape + polymer substrate
[17]	2×2 patch antenna array	0.047	2.96	6	4.17	/	0.909×0.929	/	Liquid-Metal-Filled patches + polymer
[18]	Single patch	0.005	2.7	1.65-2.17	#0.5-4.5	/	0.186×0.186	0.08	Aluminum tape + polymer
[19]	Single patch	0.01	2.7	7.5	5.5	/	0.37×0.453	0.131	Metal wire mesh + polymer
[20]	Two stacked patches	0.0253	3.11	2.75/3.2	6.7/7.3	9.4%	0.615×0.615	0.089	Copper slices + polymer slices connected with screw
[21]	Honeycomb-inspired single patch antenna	0.02	3	2.4	8.1	8.3%	0.444×0.444	0.069	Inkjet-Printed both metallic and polymer part (separated steps)

*Center Frequency； #1.5 at 1.65 GHz to 4.5 at 2.17 GHz.

3.3.2.2 Multi-layer LP Antenna Array

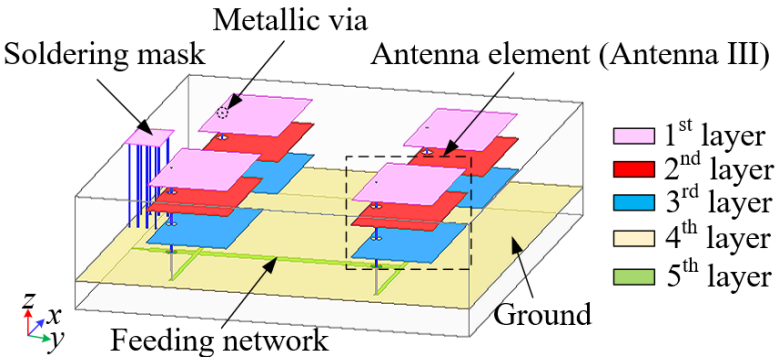

(a)

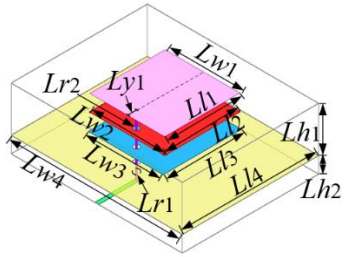

(b)

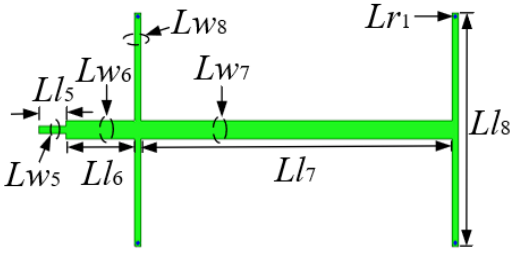

(c)

Fig. 3.13. Layouts of (a) Multi-layer antenna array and detail dimensions of its (b) Antenna element and (c) Feeding network. (Ll_1=22.6, Ll_2=22.9, Ll_3=23.3, Ll_4=39.3, Ll_5=5, Ll_6=12.9, Ll_7=50, Ll_8=57, Lw_1=38, Lw_2=39, Lw_3=40, Lw_4=70, Lw_5=1.2, Lw_6=Lw_7=3.3, Lw_8=1.2, Ly_1=1.05,

Lr_1=0.3, Lr_2=0.5, Lh_1=1.5, Lh_2=0.5. (Unit: mm)).

Based on the 3D-printed three-layer antenna, a multi-layer LP antenna array is proposed. As shown in Fig. 3.13(a), configuring the multi-layer LP antenna includes five conductive layers (three layers for antenna elements, one layer for ground, and one layer for feeding network), and the thickness of each conductive layer is set at 20 μm. The top three conductor layers consist of four antenna elements. The feeding network is located at the substrate's bottom layer. A ground layer is printed between the antenna element and the feeding network. The shape and location of the feeding network have no effect on the antenna array elements on the other side of the ground, which increases the design freedom. Four metallic vias going through the stacked patches (the second and third layers) and ground layer (the fourth layer) are introduced to connect the driven patch (the top layer) and the feeding network (the fifth layer). In addition, on the top layer, a soldering mask (10 mm × 15 mm) for welding is connected to the ground layer by eight metallic vias, whose radius is 0.3 mm. The detailed dimensions of the antenna element and feeding line are shown in Figs. 3.13(b) and (c).

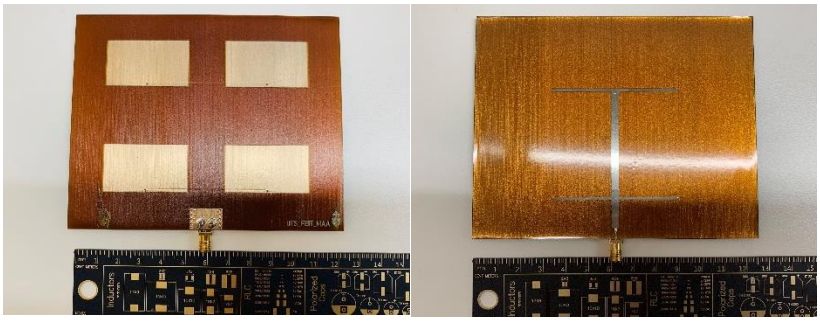

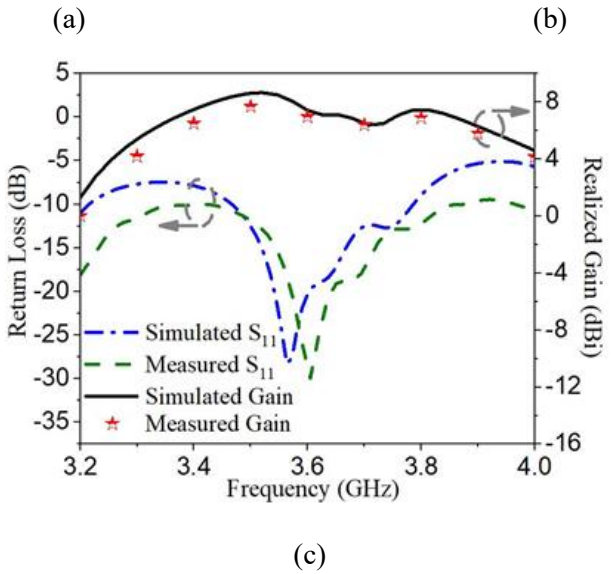

(c)

Fig. 3.14. Prototypes of (a) Top view and (b) Bottom view of the multi-layer antenna array. (c) Measured and simulated gains and return loss.

The Vector Network Analyzer (VNA) used in the measurement is a Keysight PNA N5225B, and the simulation analysis software, ANSYS High-Frequency Structure Simulator (HFSS), is utilized in the simulation. The simulated and measured results show good agreement. Fig. 3.14(a) and (b) show the top and bottom views of the fabricated antenna array. Fig. 3.14(c) depicts the simulated and measured realized gains and return loss of the multi-layer antenna array. The measured peak gain is 7.7 dBi at 3.5 GHz. The measured frequency range lower than -10 dB is from 3.46-3.93 GHz. The simulated antenna efficiency is 45%. Fig. 3.15 highlights the simulated and measured radiation patterns of the multi-layer antenna array at 3.5 GHz and 3.6 GHz in the *E*-plane and *H*-plane, respectively.

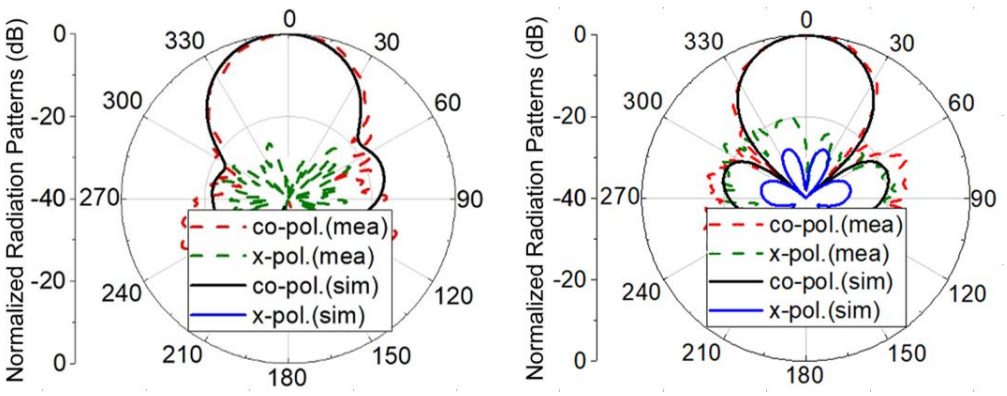

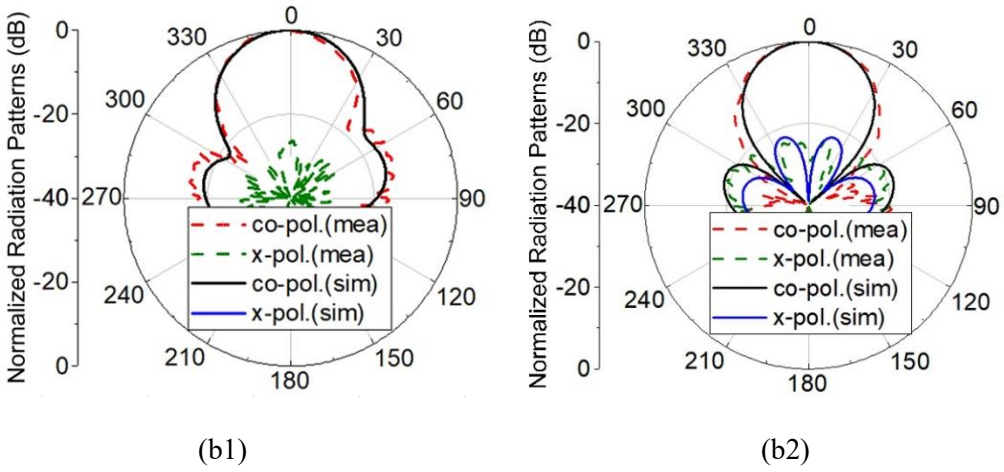

Fig. 3.15. Normalized radiation patterns of multi-layer antenna array. (a1) *YOZ*-plane at 3.5 GHz, (a2) *XOZ*-plane at 3.5 GHz, (b1) *YOZ*-plane at 3.6 GHz, (b2) *XOZ* -plane at 3.6 GHz.

3.3.3 Multi-Layer Circular Polarization Antenna and Antenna Array

3.3.3.1 Multi-layer Circular Polarization Antennas

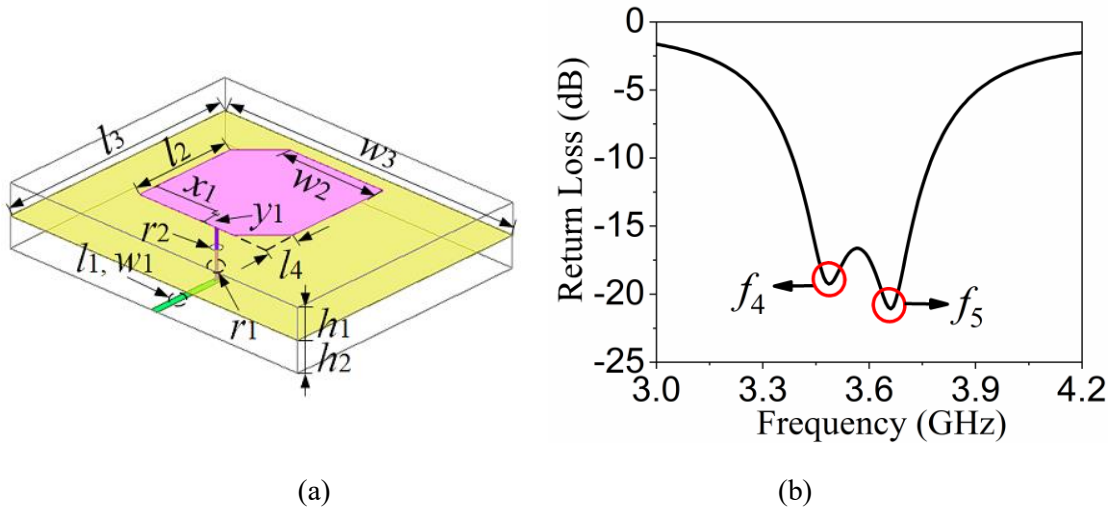

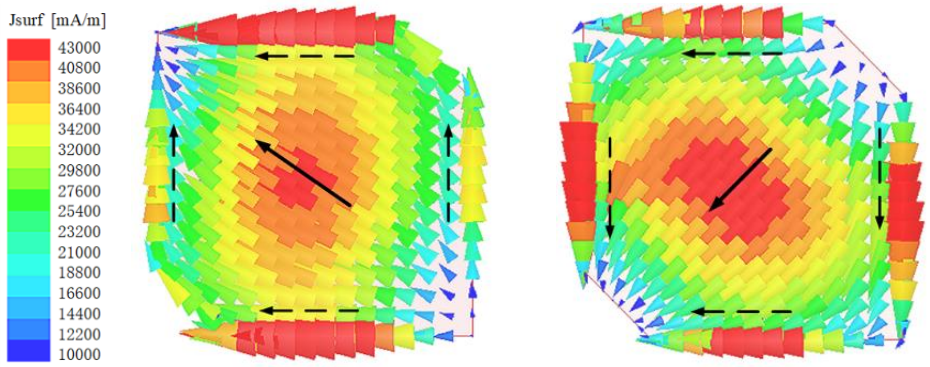

(c) (d)

Fig. 3.16. Layouts of single layer CP antenna and its (b) simulated return loss, as well as the current distribution over the antenna patch at (c) 3.48 GHz and (d) 3.66 GHz. (l_1=13, l_2=19, l_3=42.4, l_4=5.2, w_1=1.2, w_2=18.4, w_3=53.3, x_1= 11.8, y_1=3.3, r_1=0.3, r_2=0.6, h_1=1.5, h_2=0.5. (unit: mm)).

The circular polarization (CP) can be obtained by implementing two orthogonal modes. A common way to achieve CP is to trim the ends of two opposite corners of a square patch. As shown in Fig. 3.16(a), a single-layer microstrip square-patch antenna with truncated corners is depicted, and its detailed parameters are given in the index. Fig. 3.16(b) shows the simulated return loss of the single-layer CP antenna, where the excited two orthogonal modes are located at f_1 and f_2. Figs. 3.16(c) and (d) give the current distribution over the square patch of the CP antenna at these two orthogonal modes, f_3 and f_4, respectively. As can be seen in Fig. 3.16(c), the direction of the current at f_3 is top left, while the direction of the current at f_4 is bottom left, as shown in Fig. 3.16(d). It verifies that introducing truncated corners on a patch antenna can help to generate two orthogonal modes, which are vertical to each other.

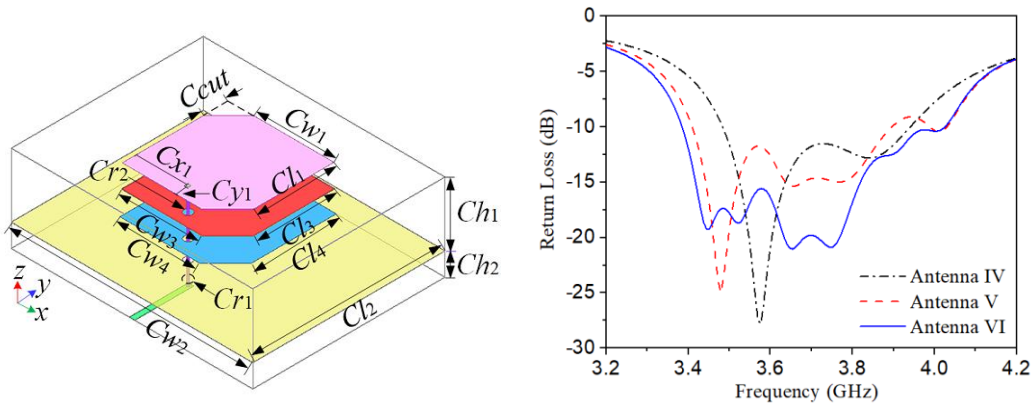

(a) (b)

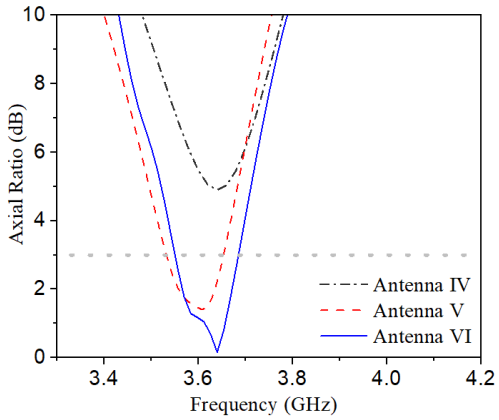

(c)

Fig. 3.17. Layouts of (a) Three-layer patch antenna consisting of a driven patch and two stacked patches with truncated corners as well as (b) Simulated return loss and (c) Axial ratio of Antenna IV, Antenna V and Antenna VI. (Cl_1=17.8, Cl_2= 43.2, Cl_3= 18, Cl_4=18.8, Cw_1=17.6, Cw_2=53.8, Cw_3=17.9, Cw_4=17.7, Cx_1=11.6, Cy_1=2.9, Cr_1=0.3, Cr_2=0.6. Ch_1=1.5, Ch_2=0.5, $Ccut$=5.6. (unit: mm)).

To further investigate this theory about multi-layer patch antennas, based on the traditional single-layer CP antenna (Antenna IV), stacked patches are added to construct the double-layer (Antenna V) and three-layer (Antenna VI) CP patch antennas. Fig. 3.17(a) demonstrates the layout of the three-layer patch antenna consisting of a driven patch and two stacked patches with truncated corners. Distance between the driven patch, the first added stacked patch, the second added stacked patch, and the top of the substrate are 0 mm, 0.3 mm and 1.1 mm, respectively. Fig. 3.17(b) depicts the simulated return loss of these three CP antennas. Obviously, with the increase in the amounts of stacked patches from 0 to 2, the number of resonant modes improved from 2 to 6, which matches that every metal patch of the multi-layer CP antenna can excite two orthogonal modes. Furthermore, the axial ratio can also be improved with increased amounts of stacked patches. As shown in Fig. 3.17(c), from Antenna IV to Antenna VI, the minimal axial ratio is decreased from 4.9 dB to 0.16 dB. The frequency range below 3-dB axial ratio is improved from none to 126 MHz (3.556 GHz to 3.682 GHz)

3.3.3.2 Multi-layer Circular Polarization Antenna Array

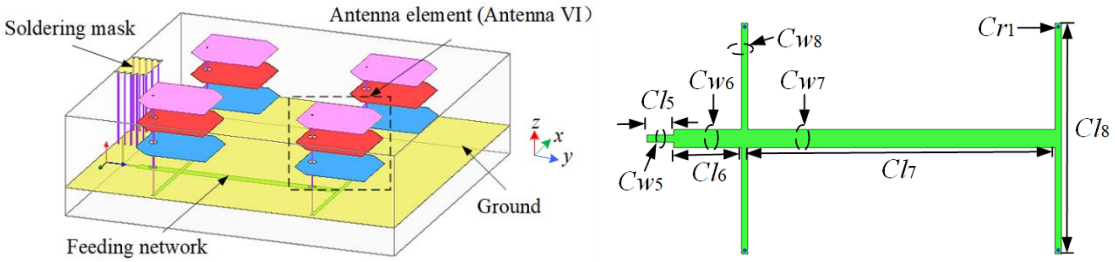

(a) (b)

Fig. 3.18 Layouts of (a) CP multi-layer antenna array and detail dimensions of its (b) Feeding network. (Cl_5=5, Cl_6=12, Cl_7=50, Cl_8=51.5, Cw_5=1.2, Cw_6=Cw_7=3.3, Cw_8=1.2, Cr_1=0.3. (unit: mm)).

A CP multi-layer antenna array is proposed based on the 3D-printed three-layer antenna (Antenna VI), as shown in Fig. 3.18(a). Like the LP multi-layer antenna array, five metal layers are introduced to construct the CP multi-layer antenna array. The thickness of the metal layer is 20 μm. The detailed dimensions of these four antenna elements are the same as the Antenna VI. The feeding network is printed on the bottom surface of the substrate connected to the first patch (driven patch) of Antenna VI with metallic vias. A 10 mm × 15 mm rectangular metal mask connecting to the ground layer is designed on the top surface of the substrate for soldering. Fig. 3.18(b) highlights the detailed dimensions of the feeding network of the proposed multi-layer CP antenna array.

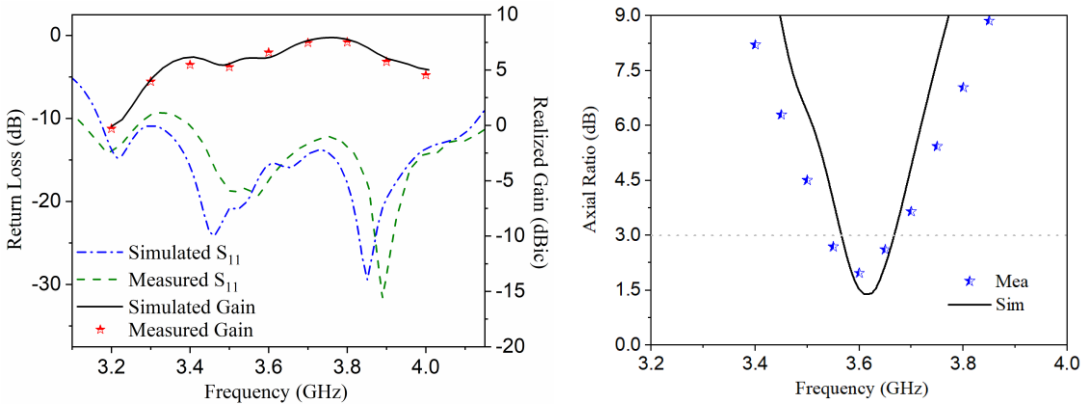

(a) (b)

Fig. 3.19 (a) Realized gain and return loss of proposed CP multi-layer antenna array. (b) Simulated and measured axial ratio of multi-layer CP antenna array.

Finally, a good agreement is reached between the simulated and measured results. As seen from Fig. 3.19(a), which shows the simulated and measured realized gain and return loss from 3.2 GHz to 4 GHz of the multi-layer CP antenna array, the simulated peak gain is 7.6 dBic at 3.8 GHz. For the return loss, six resonant modes are achieved, and the frequency range lower than -8.8 dB ranges from 3.1-4.17 GHz. In Fig. 3.19(b), the minimal measured axial ratio of the multi-layer CP antenna array is 1.97 dB at 3.6 GHz, and the operational range where the simulated AR is lower than 3-dBi can reach 140 MHz (3.54 GHz to 3.68 GHz). Fig. 3.20 is a photograph seen from the top and back view of the printed CP antenna array. The simulated and measured radiation patterns of the CP multi-layer antenna array at 3.6 and 3.65 GHz in the *YOZ*-plane and *XOZ*-plane are presented in Figs. 3.21(a) and 3.21(b), respectively.

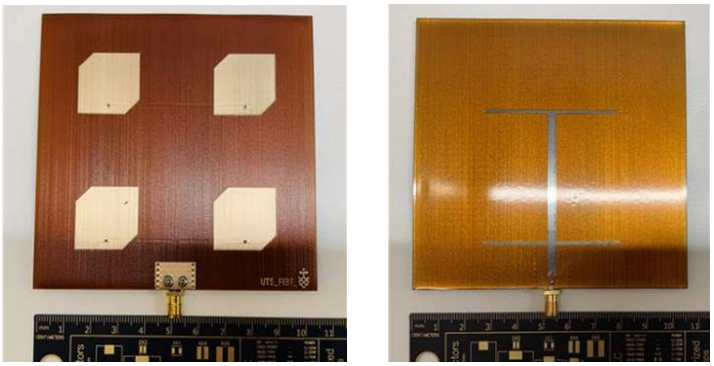

(a) (b)

Fig. 3.20 Photographs seen from (a) top view and (b) bottom view of the CP multi-layer antenna array prototype.

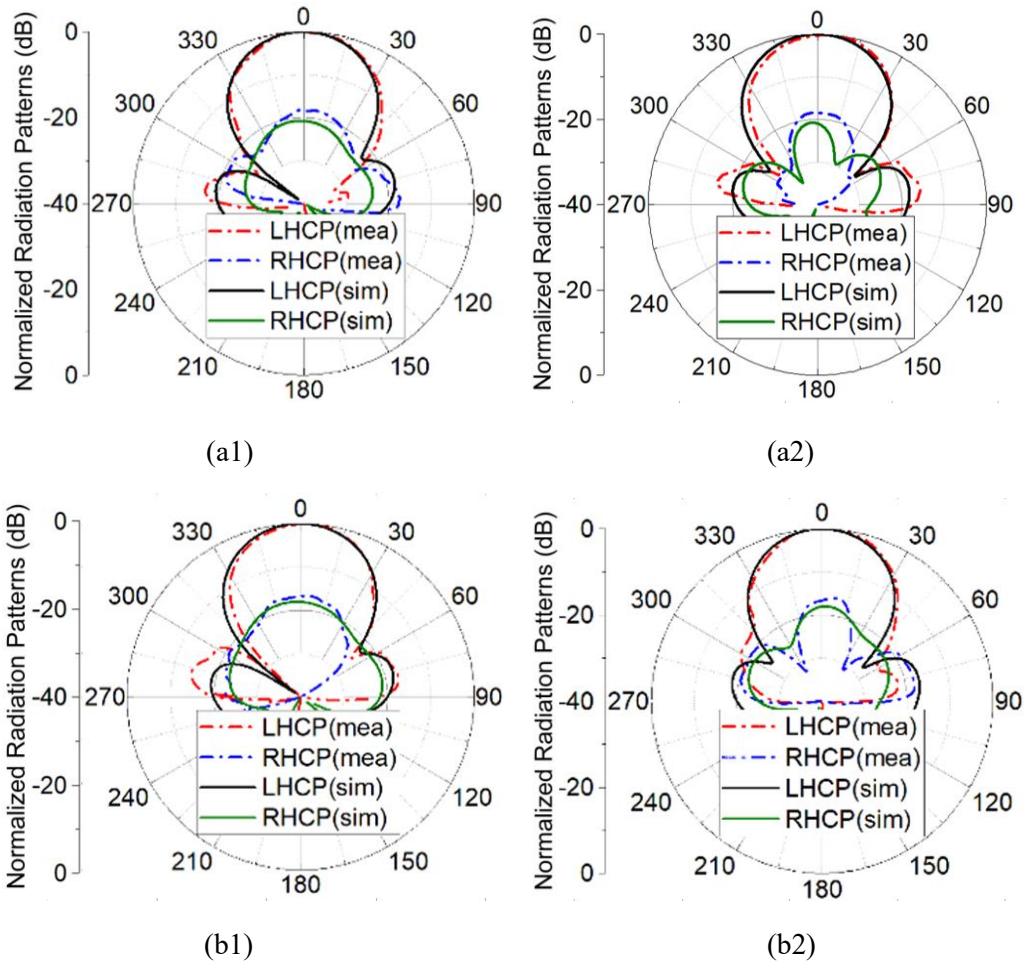

Fig. 3.21 Simulated and measured normalized radiation patterns of CP multi-layer antenna array. (a1) *YOZ*-plane at 3.6 GHz, (a2) *XOZ* -plane at 3.6GHz (b1) *YOZ*-plane at 3.65GHz, (b2) *XOZ* -plane at 3.65GHz.

3.4 Conclusion

To summarize this chapter, the RF characteristics of the dielectric material used in the 3D printing system were characterized up to 110 GHz. Considering its low loss, the cavity resonant method with the highest possible accuracy of measurement is used to measure the complex permittivity of dielectric material, which is categorized as the closed-cavity and open-cavity methods. A dielectric and conductor 3D printing system is used for developing the multi-modes patch antennas, where a surface-driven patch and embedded stacked patch are co-designed. An embedded transmission line is investigated for loss analysis and performance verification. The characterization of the

dielectric properties is examined for the desired frequency region.

A bandwidth improvement thanks to multi-mode stacked patches can be achieved, taking advantage of the three-dimensional design capability without requiring an additional substrate or affecting the in-plane dimensions of the prototype. Adjustable bandwidth and central frequency can be realized by tuning the width of driven and stacked patches. Following that, multi-layer CP antennas, as well as LP and CP antenna arrays, are designed and fabricated. Feeding networks are printed under the ground layer, improving the flexibility of the design and helping to reduce the footprint of the arrays. Devising a successful multi-layer and multi-mode patch antennas using AME technology proves that a low-cost, high-performance, time-saving manufacturing technique can be a revolutionary approach to producing 5G consumer mobile electronics.

3.5 References

[1] M. D'Auria, W. J. Otter, J. Hazell, B. T. W. Gillatt, C. L.-Collins, N. M. Ridler, and S. Lucyszyn, "3-D printed metal-pipe rectangular waveguides," *IEEE Trans. Compon. Packag. Manuf. Technol.*, vol. 5, no. 9, pp. 1339-1349, Sep. 2015.

[2] P. Nayeri, M. Liang, and R.A. Sabory-Garcia, et al., "3D printed dielectric reflectarrays: low-cost high-gain antennas at sub-millimeter waves," *IEEE Trans. Antennas Propag.,* vol. 62, no. 4, pp. 2000–2007, Oct. 2014.

[3] B. Li, P. F. Jing, L. Q. Sun, K. W. Leung and X. Lv, "3D printed OAM reflectarray using half-wavelength rectangular dielectric element," *IEEE Access*, vol. 8, pp. 142892-142899, 2020.

[4] J. Zhu, Y. Yang, D. McGloin, R. R. Unnithan, S. Li, S. Liao and Q. Xue, "3-D printed planar dielectric linear-to-circular polarization conversion and beam-shaping lenses using coding polarizer," *IEEE Trans. Ant. and Propag.,* vol. 68, no. 6, pp. 4332-4343, June 2020.

[5] A. Massaccesi, P. Pirinoli, V. Bertana, G. Scordo; S. L. Marasso, M. Cocuzza and G. Dassano, "3D-printable dielectric transmitarray with enhanced bandwidth at millimeter-waves," *IEEE Access,* vol. 6, pp. 46407-46418, 2018.

[6] B. Sanz-Izquierdo, and E. A Parker, "3-D printing of elements in frequency selective arrays," *IEEE Trans. Antennas Propag.,* vol. 62, no. 12, pp. 6060–6066, Dec. 2014.

[7] A. Shastri, B. Sanz-Izquierdo, E. A. Parker, S. Gao, P. Reynaert, Z. Chen and L. Winchester, "3D printing of millimetre wave and low-terahertz frequency selective surfaces using aerosol jet technology," *IEEE Access*, vol. 8, pp. 177341-177350, 2020.

[8] P.I. Deffenbaugh, T.M. Weller, and K.H. Church, "Fabrication and microwave characterization of 3-D printed transmission lines," *IEEE Microw. Wireless Compon. Lett.,* vol. 25, no. 12, pp. 823–825, Dec. 2015.

[9] F. Cai, Y. Chang, K. Wang, C. Zhang, B. Wang and J. Papapolymerou, "Low-loss 3-D multi-layer transmission lines and interconnects fabricated by additive manufacturing technologies," *IEEE Trans. Microw. Theory Techn.,* vol. 64, no. 10, pp. 3208–3216, Oct. 2016.

[10] A. Vallecchi, D. Cadman, W. G. Whittow, J. Vardaxoglou, E. Shamonina and C. J. Stevens, "3-D printed bandpass filters with coupled vertically extruded split ring resonators," *IEEE Trans. Microw. Theory Techn*., vol. 11, no. 67, pp. 4341-4352, Nov. 2019.

[11] A. Chauraya, W.G. Whittow, and J.C. Vardaxoglou, Y. Li, R.Torah, K. Yang, S. Beeby and J. Tudor, "Inkjet printed dipole antennas on textiles for wearable communications," *IEEE Microw. Antennas Propag.,* vol. 7, no. 9, pp. 760–767, Apr. 2013.

[12] B. S. Cook, and A. Shamim, "Inkjet printing of novel wideband and high gain antennas on low-cost paper substrate," *IEEE Trans. Antennas Propag.,* vol. 60, no. 9, pp. 4148–4156, Sep. 2012.

[13] S. Hong, Y. Kim, and C.W. Jung, "Transparent microstrip patch antennas with multi-layer and metal-mesh films," *IEEE Antennas Wirel. Propag. Lett.,* vol. 16, pp. 772–775, 2017.

[14] S. Kim, Y. Ren, H. Lee, A. Rida, S. Nikolaou and M. M. Tentzeris, "Monopole antenna with inkjet-printed EBG array on paper substrate for wearable applications," *IEEE Antennas Wirel. Propag. Lett.,* vol. 11, pp. 663–666, Jun. 2012.

[15] L. Catarinucci, F. P. Chietera and R. Colella, "Permittivity-customizable ceramic-doped silicone substrates shaped with 3-D-printed molds to design flexible and conformal antennas," *IEEE Antennas Wirel. Propag. Lett.,* vol. 68, no. 6, pp. 4967-4972, June 2020.

[16] G. Muntoni et al., "A curved 3-D printed microstrip patch antenna layout for bandwidth enhancement and size reduction," *IEEE Antennas Wirel. Propag. Lett.,* vol. 19, no. 7, pp. 1118-1122, July 2020.

[17] X. Yu, M. Liang, C. Shemelya, D. A. Roberson, R. Wicker, E. MacDonald and H. Xin, "3-D printed parts for a multi-layer phased array antenna system," *IEEE Antennas Wirel. Propag. Lett.,* vol. 17, no. 11, pp. 2150–2154, Nov. 2018.

[18] V. M. Pepino, A. F. da Mota, A. Martins and B. V. Borges, "3-D-printed dielectric metasurfaces for antenna gain improvement in the Ka-Band," *IEEE Antennas Wirel. Propag. Lett.,* vol. 17, no. 11, pp. 2133-2136, Nov. 2018.

[19] M. F. Farooqui and A. Kishk, "3-D-printed tunable circularly polarized microstrip patch antenna," *IEEE Antennas Wirel. Propag. Lett.,* vol. 18, no. 7, pp. 1429-1432, July 2019.

[20] M. Liang, C. Shemelya, E. MacDonald, R. Wicker and H. Xin, "3-D printed microwave patch antenna via fused deposition method and ultrasonic wire mesh embedding technique," *IEEE Antennas Wirel. Propag. Lett.,* vol. 14, pp. 1346-1349, 2015.

[21] S. Wang, L. Zhu and W. Wu, "3-D printed inhomogeneous substrate and superstrate for application in dual-band and dual-CP stacked patch antenna," *IEEE Trans. Antennas Propag.,* vol. 66, no. 5, pp. 2236-2244, May 2018.

[22] G. McKerricher, D. Titterington, and A. Shamim, "A fully inkjet-printed 3-D honeycomb-inspired patch antenna," *IEEE Antennas Wirel. Propag. Lett.,* vol. 15, pp. 544–547, 2016.

[23] T. Bhattacharjee, H. Jiang and N. Behdad, "A fluidically tunable, dual-band patch antenna with closely spaced bands of operation," *IEEE Antennas Wirel. Propag. Lett.,* vol. 15, pp. 118-121, 2016.

[24] J. Sun and K. Luk, "A circularly polarized water patch antenna," *IEEE Antennas Wirel. Propag. Lett.,* vol. 19, no. 6, pp. 926-929, June 2020.

[25] S. Wang, X. Zhang, L. Zhu and W. Wu, "Single-fed wide-beamwidth circularly polarized patch antenna using dual-function 3-D printed substrate," *IEEE Antennas Wirel. Propag. Lett.,* vol. 17, no. 4, pp. 649-653, April 2018.

[26] K. X. Wang and H. Wong, "A wideband millimeter-wave circularly polarized antenna with 3-D printed polarizer," *IEEE Antennas Wirel. Propag. Lett.,* vol. 65, no. 3, pp. 1038-1046, March 2017.

[27] V. Bharambe, D. P. Parekh, C. Ladd, K. Moussa, M. D. Dickey and J. J. Adams, "Liquid-metal-filled 3-D antenna array structure with an integrated feeding network," *IEEE Antennas Wirel. Propag. Lett.,* vol. 17, no. 5, pp. 739-742, May 2018.

[28] L. Song, W. Gao and Y. Rahmat-Samii, "3D printed microfluidics channelizing liquid metal for multi-polarization reconfigurable extended E-shaped patch antenna," *IEEE Antennas Wirel. Propag. Lett.,* early access, 2020.

[29] S. Moscato, R. Bahr, T. Le, M. Pasian, M. Bozzi, L. Perregrini and M. M. Tentzeris, "Infill-dependent 3-D-printed material based on ninjaFlex filament for antenna applications" *IEEE Antennas Wirel. Propag. Lett.,* vol. 15, pp. 1506–1509, 2016.

[30] S. Narke, S. Ananthakrishnan and C. Bhattacharya, "Enhancement of axial ratio-beamwidth of X-band composite microstrip patch antenna with conical ground plane," *Electron. Lett.,* vol. 56, no. 9, pp. 419-421, 30 4 2020.

[31] S. Jun, B. Sanz-Izquierdo, J. Heirons, C.X. Mao, S. Gao, D. Bird and A. McClelland, "Circular polarised antenna fabricated with low-cost 3D and inkjet printing equipment," *Electron. Lett.,* vol. 53, no. 6, pp. 370-371, 2017.

[32] S. M. Radha, G. Shin, P. Park and I. Yoon, "Realization of electrically small, low-profile quasi-isotropic antenna using 3D printing technology," *IEEE Access,* vol. 8, pp. 27067-27073, 2020,

[33] B. T. Malik, V. Doychinov, S. A. R. Zaidi, I. D. Robertson and N. Somjit, "Antenna gain enhancement by using low-infill 3D-printed dielectric lens antennas," *IEEE Access,* vol. 7, pp. 102467-102476, 2019.

[34] S. Alkaraki, Y. Gao, S. Stremsdoerfer, E. Gayets and C. G. Parini, "3D printed corrugated plate antennas with high aperture efficiency and high gain at X-Band and Ka-Band," *IEEE Access*, vol. 8, pp. 30643-30654, 2020.

[35] K. Johnson, M. Zemba, B. P. Conner, J. Walker, E. Burden, K. Rogers, K. R. Cwiok, E. Macdona. and P. Cortes, "Digital manufacturing of pathologically-complex 3D printed antennas," *IEEE Access*, vol. 7, pp. 39378-39389, 2019.

[36] T. Bharambe, J. Ma, M. D. Dickey and J. J. Adams, "Planar, multifunctional 3D printed antennas using liquid metal parasitics," *IEEE Access,* vol. 7, pp. 134245-134255, 2019.

[37] P. M. Njogu, B. Sanz-Izquierdo, S. Y. Jun, G. Kalman, S. Gao, A. Malas and G. J. Gibbons," Evaluation of planar inkjet-printed antennas on a low-cost origami flapping robot," *IEEE Access*, vol. 8, pp. 164103-164113, 2020.

[38] M. I. Magray, G. S. Karthikeya, K. Muzaffar, S. K. Koul and A. H. Moon, "Wideband asymmetric coplanar strip fed antennas with pattern diversity for mmWave 5G base stations," *IEEE Access*, vol. 8, pp. 77482-77489, 2020.

[39] K. Y. Kapusuz, S. Lemey, A. Petrocchi, P. Demeester, D. Schreurs and H. Rogier, "Polarization reconfigurable air-filled substrate integrated waveguide cavity-backed slot antenna," *IEEE Access*, vol. 7, pp. 102628-102643, 2019.

[40] S. Sarjoghian, M. H. Sagor, Y. Alfadhl and X. Chen, "A 3D-printed high-dielectric filled elliptical double-ridged horn antenna for biomedical monitoring applications," *IEEE Access,* vol. 7, pp. 94977-94985, 2019.

[41] X. Y. Liu, Y. Zhu, W. Xie, G. H. Peng and W. Wang, "Generation of plane spiral orbital angular momentum waves by microstrip yagi antenna array," *IEEE Access*, vol. 8, pp. 175688-175696, 2020.

[42] B. Urasinska-Wojcik, N. Chilton, P. Todd, C. Elsworthy, M. Bates, G. Roberts and G. J. Gibbons, "Integrated manufacture of polymer and conductive tracks for real-world applications," *Addit. Manuf.*, vol. 29, Oct. 2019.

[43] P. F. Flowers, C. Reyes, S. Ye, M. J. Kim, B. J. Wiley, "3D printing electronic components and circuits with conductive thermoplastic filament," *Addit. Manuf.*, vol. 18, pp. 156-163, Dec. 2017.

[44] J. Krupka, "Frequency domain complex permittivity measurements at microwave frequencies," *Meas. Sci. Technol.,* vol. 17, no. 6, pp. R55-R70, 2006.

[45] C. Yu, E. Li, and G. Guo, "Dielectric characterisation of small samples using broadband coaxial cavity," *Electron. Lett.*, vol. 53, no. 19, pp. 1316-1318, 2017.

[46] Y. Zhang, E. Li, J. Zhang, C. Yu, H. Zheng, and G. Guo, "A broadband variable-temperature test system for complex permittivity measurements of solid and powder materials." *Rev. Sci. Instrum*., vol. 89, no. 2, 024701, 2018.

[47] A. K. Jha, M. J. Akhtar, "A generalized rectangular cavity approach for determination of complex permittivity of materials," *IEEE Trans. Instrum. Meas.,* vol. 63, no. 11, pp. 2632-2641, 2014.

[48] T. M. Hirvonen, P. Vainikainen, A. Lozowski, and A. V. Raisanen. "Measurement of dielectrics at 100 GHz with an open resonator connected to a network analyzer," *IEEE Trans. Microw. Theory Techn.*, vol. 45, no. 4, pp. 780-786, 1996.

[49] K. -F. Lee and K. -F. Tong, "Microstrip patch antennas-basic characteristics and some recent advances," *Proceedings of the IEEE*, vol. 100, no. 7, pp. 2169-2180, July 2012.

Chapter 4 3D-Printed Compact Transmission Lines, and Multi-layer Bandpass Filters

4.1 Introduction

With the rapid advances being made in additive manufacturing technology, more and more multi-material 3D printers can fabricate conductive and dielectric materials simultaneously, demonstrating their capabilities in electronic device integration and 3D packaging [1]–[5]. However, it is still a challenge for these 3D printers to fabricate a seamless multi-metal layer in a single substrate. According to the open literature, multi-metal-layer technologies have an outstanding advantage in device minimization, such as low-temperature co-fired ceramic (LTCC) [6]–[10] or semiconductor technologies [11]–[13]. For example, Xu and Zhang [8] proposed a compact LTCC diplexer with high isolation. In [11], an on-chip miniaturized bandpass filter (BPF) is presented, which is based on a grounded center-tapped ring resonator with shunt capacitive loading. Although both designs demonstrated device minimization, these technologies are expensive and require complicated fabrication processes and longer production times. As an emerging technology, low-temperature additive manufacturing technologies have been applied in integrated electronic devices and packaging, such as electronic components [14], antenna arrays [15], terahertz lens [16], redistribution layers [17], combiner [18], transistors [19], and enzymatic biofuel [20].

In this chapter, a low-temperature additively manufactured electronics (AME) solution is introduced for BPF design, taking advantage of dual-materials (conductive and dielectric materials) printing, Nano Dimension's DragonFly LDM system is used for AME designs. This system simultaneously jets both dielectric and conductive inks, hence simultaneously creating multi-layer conductive structures within a single dielectric substrate. Compared with LTCC and semiconductor technologies, the AME solution is flexible on electronic device fabrication with design freedom adjusting the interlayer distance. The printing process is carried out at a typical temperature of 140 °C

in a standard ambient atmosphere. For proof-of-concept, a multi-layer BPF with vertically integrated capacitors and inductors has been designed, analyzed, fabricated, and measured. To improve the performance of the proposed BPF, a shorted stepped impedance stub is loaded at the zero-voltage point of the resonator to suppress the third harmonic mode. Therefore, the upper stopband of the BPF that is more than 20 dB rejection level from 16.65 to 39.89 GHz (1.90 f_0). In addition, in this chapter, a vertically integrated composite right/left-handed (CRLH) TL that has a compact size and the wide operational band is proposed as well. It has unique electromagnetic characteristics of negative permittivity and negative permeability. Based on this advanced vertically integrated CRLH structure, a BPF with wide band and great in-band flatness is proposed. In the designing of this BPF, broadside coupling is used to replace traditional edge coupling for stronger coupling capacitance and smaller size. For all the proposed devices in this chapter, finite element electromagnetic (EM) field simulation analysis software, ANSYS High-Frequency Structure Simulator (HFSS), is used in the simulation, and the vector network analyzer (VNA) used in the measurement is a Keysight PNA.

4.2 Bandpass Filters Based on a Second-Order Stub-Loaded Resonator Consisting of Multi-Metal Layer Components

The printed BPF is composed of the inductance and capacitance components. The proposed AME technique has the advantage of circuit miniaturization, which is demonstrated by using an inductor and a capacitor as examples.

4.2.1 3D-Printed Multi-Metal Layer Capacitors and Inductors

4.2.1.1 Miniaturized 3D Spiral Inductor

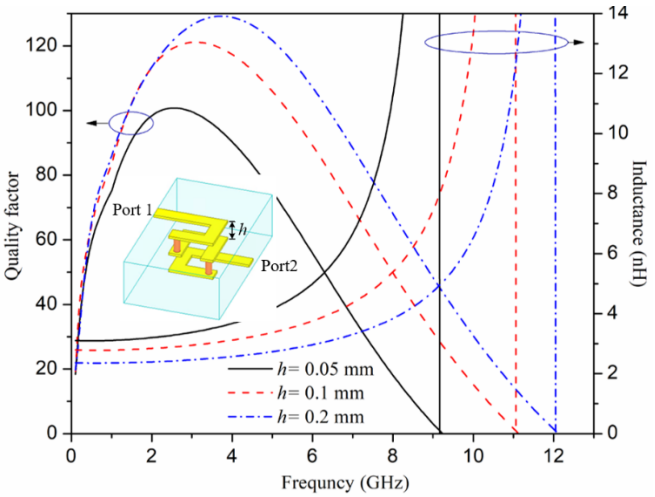

Fig. 4.1 Simulated inductances and quality factors of multi-layer spiral inductors with different dielectric-layer thicknesses (h).

For vertical spiral inductors, the inductance can be calculated by

$$L = K\frac{\mu_0\mu_r N^2 A_e}{H} \tag{4-1}$$

where μ_0 is the permeability of free space, μ_r is the relative permeability of the material, N is the total number of turns; H denotes the total height of coil, A_e stands for the section area of the coil, and K is a coefficient that depends on the ratio of r (radius of the coil) to H. To investigate the relationship between the L and H, Fig. 4.1 visually compares simulated inductances with different dielectric-layer thicknesses h. When h drops from 0.2 mm to 0.05 mm, the inductance increases gradually. As well, Fig. 4.1 shows the quality factor versus different values of h. With the decline of h, the inductance density increases, which means that a higher inductance value can be obtained with a lower profile and constant plane size. A drop in peak quality factor is observed because increasing inductance usually involves increasing magnetic layer thickness, which leads to higher eddy currents. The inductor has self-resonant characteristics when the peak magnetic and electric energies are equal. Three major parasitic capacitances in the multilayer spiral inductor determine characteristics of the inductor including self-

resonance frequency: the intermetal layer capacitance, the metal to substrate capacitance and the metal to underpass capacitance. For the spiral inductor, when *h* drops from 0.2 mm to 0.05 mm, the decrease of self-resonance frequency from 12.1 to 9.2 GHz is mainly due to the increased parasitic intermetal layer capacitance.

4.2.1.2 Miniaturized Capacitors with Reduced Interlayer Distance

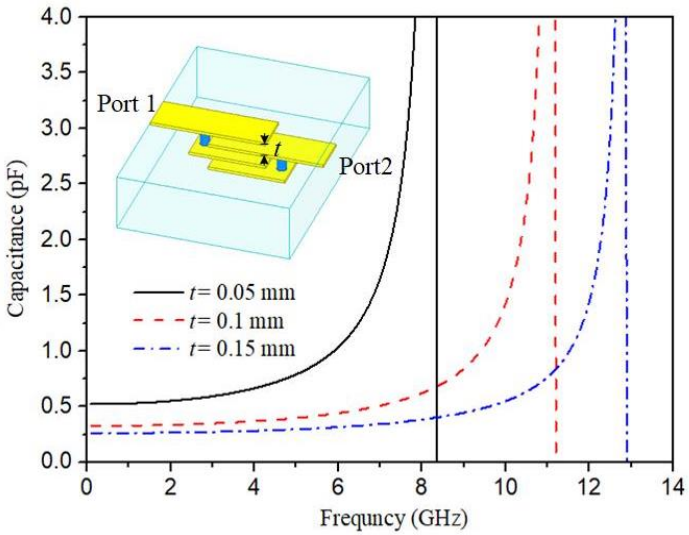

Fig. 4.2 Comparison of simulated capacitances of multi-layer capacitors with different dielectric-layer thickness *t*.

According to reference [21], for a multilayer capacitor, the capacitance "*C*" is given in the equation below:

$$C = \frac{\varepsilon_0 \varepsilon_s S(n-1)}{t} \tag{4-2}$$

where: ε_0 denotes the dielectric constant of free space, ε_s is the relative dielectric constant of the material, *S* represents the effective area of the inner electrode. *n* is the number of inner electrodes, and *t* is the thickness of the dielectric layer.

Obviously, with the increase in the number of inner electrodes or raising the inner electrode effective area, the capacitance will increase. That is also the most common method for designing a capacitor, as stated in the literature. However, in this thesis, the effect of the thickness of the dielectric layer is discussed. As shown in Fig. 4.2, with the reduction in dielectric-layer thickness *t* from 0.15 mm to 0.05 mm, capacitance increases significantly while the capacitor size keeps unchanged, consistent with

equation (4-2). In other words, the adjustable interlayer distance can contribute to a smaller plane size and lower profile. Meanwhile, when the dielectric-layer thickness *t* drops from 0.15 mm to 0.05 mm, the self-resonance frequency of the capacitor decreases from 12.9 to 8.3 GHz.

4.2.2 3D-Printed Multi-metal Layer Bandpass Filters and its Equivalent Circuits

4.2.2.1 Bandpass Filter Configuration

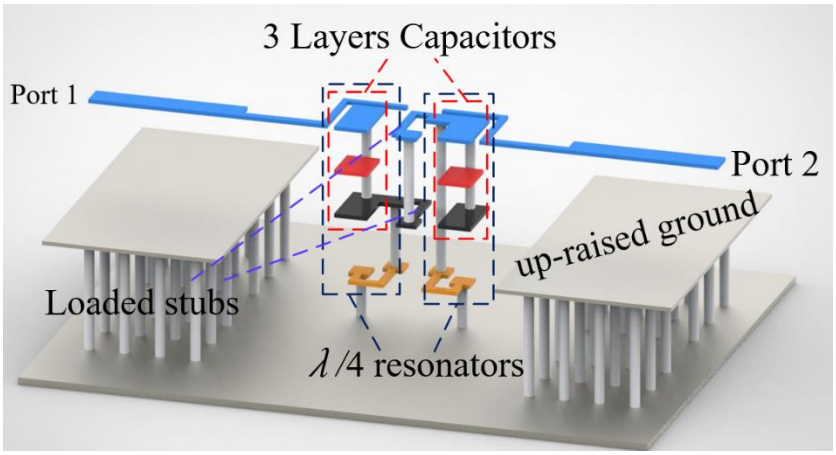

(a)

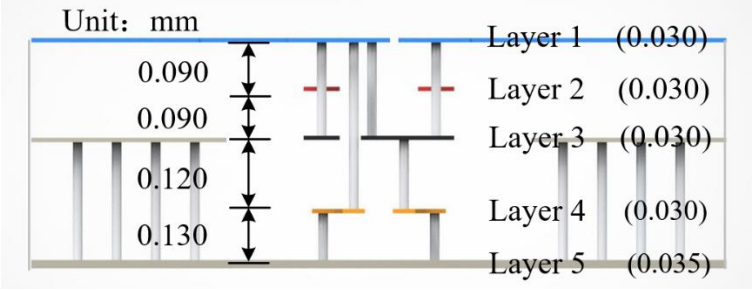

(b)

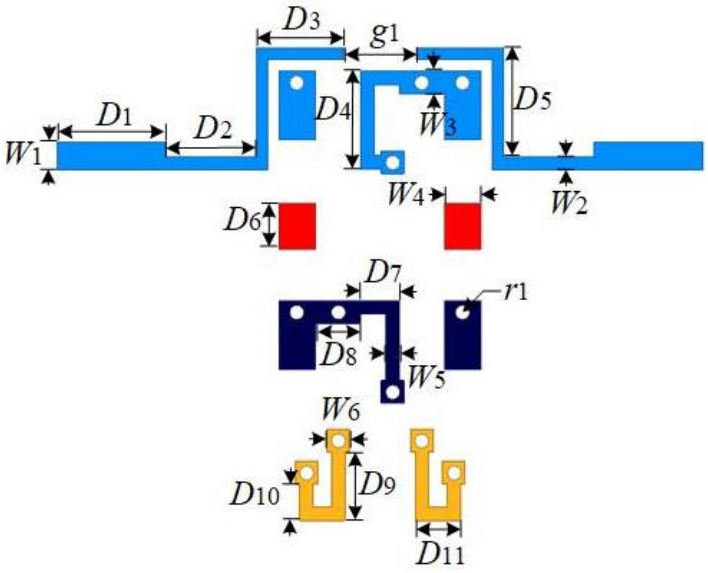

(c)

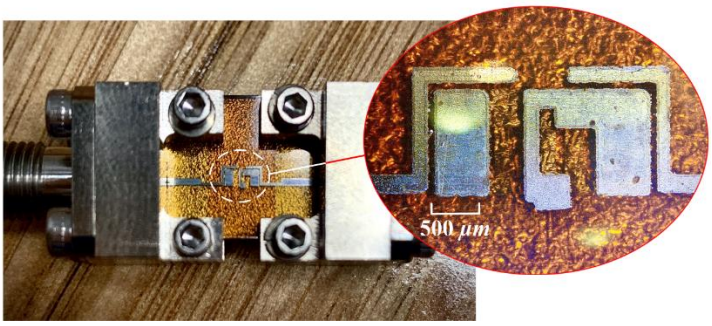

(d)

Fig. 4.3 3D view and (b) Side view, (c) Layout of each layer, (d) Photograph of the 3D-printed BPF with testing accessories and structural details of the filter under a microscope.

In Fig. 4.3(a), the 3D view of the proposed BPF is presented. Taking advantage of the proposed AME solution, the number of metal layers and the dielectric layer thickness among metal layers can be flexibly defined for circuit design. In this work, as shown in Fig. 4.3(b), five metal layers are employed to design the BPF, where layer 5 is used as the ground. The constructions of feeding lines and resonators are distributed from layer 1 to layer 4. The resonant part of the BPF consists of two λ/4 resonators, where three metal layers are stacked to form a compact capacitor. Two stepped-impedance stubs, located on layer 1 and layer 3, respectively, are loaded at the one-third point to improve the out-of-band suppression. Two up-raised grounds located at layer 3 are connected to the RF ground by 24 vias, respectively, to adjust the impedance

match. Fig. 4.3(c) depicts the layout of the metal layers. Parameters of the proposed BPF are determined as follows (all in mm): D_1=3.3, D_2=1.6, D_3=1.28, D_4=1.3, D_5=1.305, D_6=0.85, D_7=0.4, D_8=0.5, D_9=0.85, D_{10}=0.425, D_{11}=0.7, W_1=0.5, W_2=0.125, W_3=0.4, W_4=0.65, W_5=0.15, W_6=0.4, r_1=0.1, and g_1=0.7. The dimensions of BPF excluding feeding lines are 2.7 mm × 1.425 mm × 0.585 mm or 0.186 λg × 0.098 λg× 0.040 λg, where λg is the guided wavelength at the center frequency. In Fig. 4.3(d), the photograph shows an additively manufactured prototype with testing accessories and structural details of the filter under a microscope.

4.2.2.2 Equivalent Lumped Component Circuit

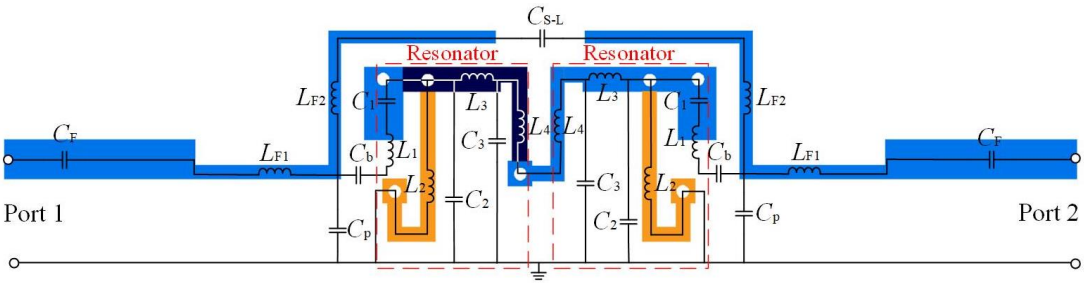

Fig. 4.4 Equivalent *LC*-circuit model based on the unfolded layout of the proposed BPF (Derived from Fig. 4.3(a) for illustration of the LC components).

To facilitate the analysis of the proposed multi-metal layers BPF, an equivalent circuit based on the unfolded layout of the BPF is presented and discussed. Fig. 4.4 presents the equivalent lumped component (*LC*)-circuit model of the presented EM structure, where inductors and capacitors represent the high-impedance lines and the capacitive couplings, respectively. L_{Fi} (i=1, 2) denotes the self-inductances of the feeding lines. C_F is the capacitive coupling between the soldering area of SMK connector and the ground. C_b represents the coupling capacitance between the feeding line and the resonator. C_p is the bypass capacitance of the feeding line to the ground. In addition, the source to load coupling is modeled by $C_{S\text{-}L}$. The inductors and capacitors of the resonators are L_1 and C_1, where L_1 and C_1 represent the parasitic inductor and the capacitance of this three-dimension interdigital capacitor, respectively. L_2 is the self-inductance of the quarter wavelength resonator. The loaded stepped-impedance is

represented by C_2, L_3 and C_3, L_4. C_2, L_3 denotes the low-impedance segment. The C_3 and L_4 denote the high-impedance segment.

4.2.2.3 Analysis of Equivalent LC-Circuit Model

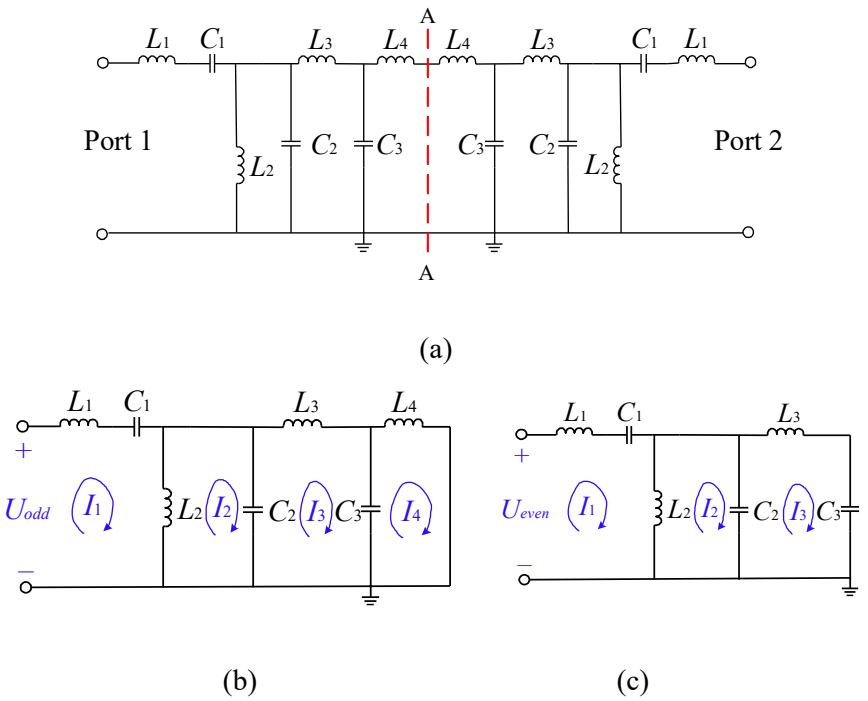

Fig. 4.5. (a) Equivalent circuit of the resonators and its (b) Odd- and (c) Even-mode equivalent circuits.

For circuit analysis, an equivalent *LC*-circuit of resonators is depicted in Fig. 4.5(a). Since the two resonators are symmetrical about AA′, odd- and even-mode circuits can be obtained, as shown in Figs. 4.5(b) and (c). The loop equation method is used for circuit analysis, of which the loop currents I_i (i=1, 2, 3, 4) are marked in Figs. 4.5(b) and (c). The expressions of input admittance are listed to calculate the resonant frequencies of transmission poles (TPs) and transmission zeros (TZs).

Applying Kirchhoff's voltage law (KVL) to the odd-mode equivalent circuit in Fig. 4.5(b), the voltage equations of the four loops are expressed as:

$$\frac{I_1}{sC_1}+sL_1I_1+sL_2(I_1-I_2)-U_{\text{odd}}=0 \tag{4-3}$$

$$\frac{(I_2-I_3)}{sC_2}+sL_2(I_2-I_1)=0 \tag{4-4}$$

$$\frac{(I_3-I_2)}{sC_2}+sL_3I_3+\frac{(I_3-I_4)}{sC_3}=0 \tag{4-5}$$

$$sL_4I_4+\frac{(I_4-I_3)}{sC_3}=0 \tag{4-6}$$

Similarly, applying KVL to the even-mode equivalent circuit in Fig. 4.5(c), the voltage equations of the three loops are expressed as:

$$\frac{I_1}{sC_1}+sL_1I_1+sL_2(I_1-I_2)-U_{\text{even}}=0 \tag{4-7}$$

$$\frac{(I_2-I_3)}{sC_2}+sL_2(I_2-I_1)=0 \tag{4-8}$$

$$\frac{(I_3-I_2)}{sC_2}+sL_3I_3+\frac{I_3}{sC_3}=0 \tag{4-9}$$

where U_{odd} and U_{even} denote the input voltages of odd- and even- mode circuits, respectively. s is a complex variable in proportion to angular frequency ω. Therefore, the relationships between input voltages and input admittances in Figs. 4.5(b) and (c) can be written as:

$$Y_{odd}(s)=\frac{I_{1\_odd}(s)}{U_{odd}(s)}=\frac{I_{1\_odd}(j\omega_{odd})}{U_{odd}(j\omega_{odd})} \tag{4-10}$$

$$Y_{even}(s)=\frac{I_{1\_even}(s)}{U_{even}(s)}=\frac{I_{1\_even}(j\omega_{even})}{U_{even}(j\omega_{even})} \tag{4-11}$$

$$Y_{odd}=\frac{C_1s(L_1+L_2+L_3+(L_2+L_3)C_2L_1s^2+(L_1+L_2)C_3L_3s^2+C_2C_3L_1L_2L_3s^4}{(L_1+L_2+L_3)(C_1L_4s^2+1)+(C_1+C_2)(L_2+L_3)L_1s^2+(L_1+L_2)C_3L_3s^2+(L_2C_2+L_3C_3+L_3C_2)C_1L_1L_4s^4+(L_1C_1+L_1C_2+L_4C_1)C_3L_2L_3s^4+C_1C_2C_3L_1L_2L_3L_4s^6} \tag{4-12}$$

$$Y_{even}=\frac{sC_1(C_2L_1s^2+C_3L_1s^2+C_3L_2s^2+C_2C_3L_1L_2s^4+1)}{(C_1+C_2+C_3)L_1s^2+C_1L_4s^2+C_3L_2s^2+(C_1+C_2)C_3L_1L_2s^4+(C_2+C_3)C_1L_1L_4s^4+C_1C_2C_3L_1L_2L_4s^6+1} \tag{4-13}$$

where ω denotes angular frequency, and j is a pure imaginary unit number.

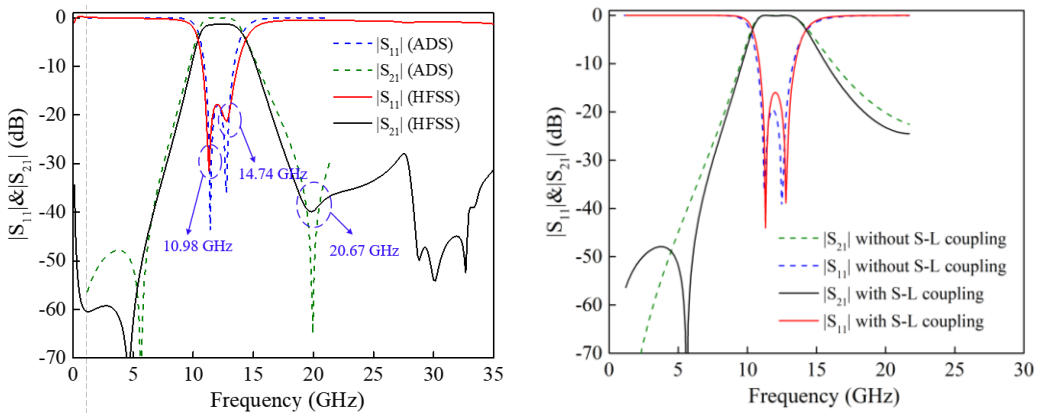

(a) (b)

Fig. 4.6. Simulated frequency responses of (a) the BPF (by HFSS) as well as the equivalent *LC*-circuit (by ADS) and (b) Simulated frequency responses of the BPF with or without S-L coupling.

Using MATLAB, the expression of input admittances consists of complex variable *s* and lumped *LC*- elements can be deduced by solving equations (4-2)-(4-11), shown as equations (4-12)-(4-13). Since ω=2π*f*, the frequencies f_{odd} and f_{even} (corresponding to odd- and even-mode) can be calculated when $Y_{odd}(j\omega) = 0$ and $Y_{even}(j\omega) = 0$, respectively. Meanwhile, the TZs can be determined when $Y_{odd}(j\omega) = Y_{even}(j\omega)$. For verification, the equivalent LC-circuit is optimized to match the finite element electromagnetic field simulation result of the EM structure. As shown in Fig. 4.6(a), the simulated results of equivalent LC-circuit carried by ADS are illustrated. Good agreement can be obtained between the calculated results of LC-circuit and simulated results of the EM structure. Substituting the obtained values of lumped elements in equivalent circuit: L_1= 0.016 nH, L_2=0.589 nH, L_3=0.725 nH, L_4=1.247 nH, C_1=0.345 pF, C_2=0.18 pF, C_3=0.11 pF into equations (12)-(13), one TZs f_{zi} (i=1) and two TPs f_{pi} (i=1,2) can be obtained in the frequency range of 0-35 GHz through the calculations. Finally, the estimated TZs and TPs are marked in Fig. 4.6(a) as well. Compared with the simulated results of TZs and TPs: f_{z1} =19.85 GHz, f_{p1} =11.31 GHz and f_{p2} =13.18 GHz, the calculated results agree well with the simulated ones. To improve the skirt selectivity, (source-load) S-L coupling is induced by adding a capacitor between two ports, as shown in Fig. 4.6(b). The locations of the TZs depend on the mixed electromagnetic (EM) coupling coefficient between the two resonators and the (source-load) S-L coupling construction.

Since these two resonators of the BPF are connected by via, the result is that the magnetic coupling is larger than the electric one. Therefore, a TZ would be excited at the upper (magnetic-dominant coupling) stopband (TZ_2).

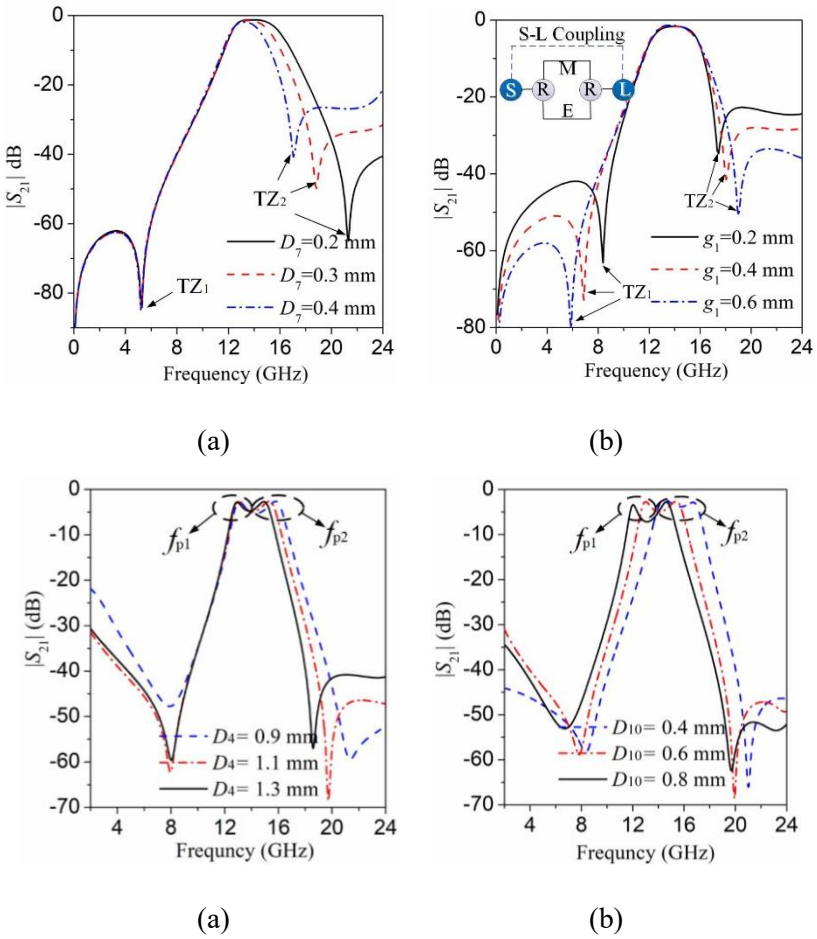

Fig. 4.7. Simulated frequency responses against (a) D_7, (b) g_1 with coupling topology inserted, (c) D_4 and (d) D_{10}.

As shown in Fig. 4.7(a), the frequency response of the coupled resonators against spacing D_7 is depicted, which shows the variation of the EM coupling between the two resonators. Lower-band TZ (TZ_1) and upper-band TZ (TZ_2) are marked in the picture. By tuning D_7, the location of the TZ_2 can be adjusted at the upper stopband, which significantly enhances the out-of-band attenuation of the proposed filter, while the TZ_1 remains unchanged. In addition, the simulated frequency response against g_1 is given for the TZ created in the low-band (TZ_1), as shown in Fig. 4.7(b). When g_1 decreases from 0.3 to 0.1 mm, the TZ_1 increases from 5.88 to 8.37 GHz, whereas the TZ_2 changes

slightly without affecting the filter bandwidth. The closer the TZs are to the passband, the better the frequency selectivity is achieved.

For the frequency response of the TPs, by solving $Y_{odd}(j\omega) = 0$ and $Y_{even}(j\omega) = 0$, it is evident that the even-mode resonant frequency f_{even} is the function of L_4, while f_{odd} is the function of both L_2 and L_4. L_2 and L_4 correspond to the length of D_4 and D_{10} in the EM structure, respectively. For validation, the simulated responses against D_4 and D_{10} are shown in Figs. 4.7(c) and (d). When D_4 rises from 0.9 mm to 1.3 mm, f_{p1} remains constant while f_{p2} falls away gradually. Besides, with the development of D_{10}, f_{p1} and f_{p2} decline simultaneously. The variations are consistent with the analysis and verify that the bandwidth and center frequency can be flexibly designed.

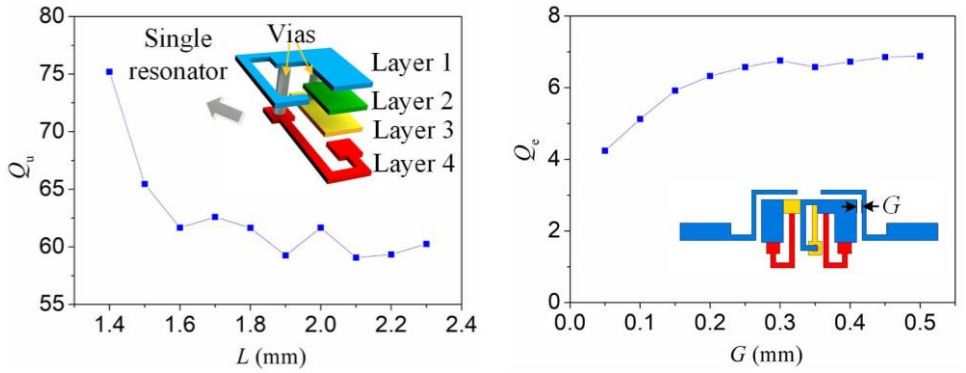

(a) (b)

Fig. 4.8. Simulated Unloaded Q_u of the proposed single resonator against a different L (b) and extracted external quality factors Q_e against a different coupling gap G.

The unloaded quality factor of the resonators is important for filter performance. In Fig. 4.8(a), for a single resonator used in the proposed BPF (center frequency = 12.25 GHz), the simulated unloaded Q-factor versus the length $L=D_9+D_{10}+D_{11}$ is presented. According to Fig. 4.8(a), when L increases, the unloaded Q_u decreases due to dielectric and conductor losses. As well as this, the external quality factor Q_e with varied coupling gap G is depicted in Fig. 4.8(b). When G increases from 0.05 to 0.5 mm, a higher Q_e of the filter can be obtained and this causes the bandwidth to decrease.

4.2.2.4 Suppression of the Third Harmonic and Wide Stopband

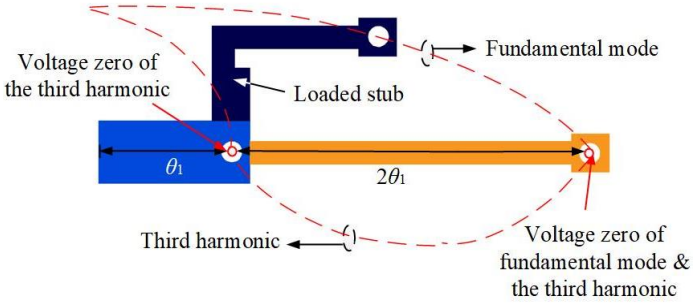

(a)

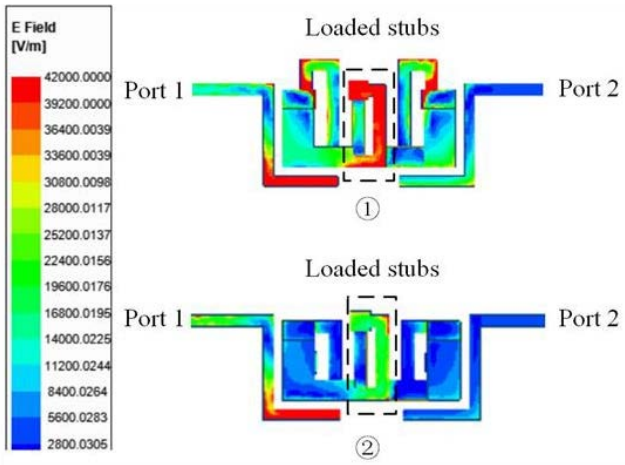

(b)

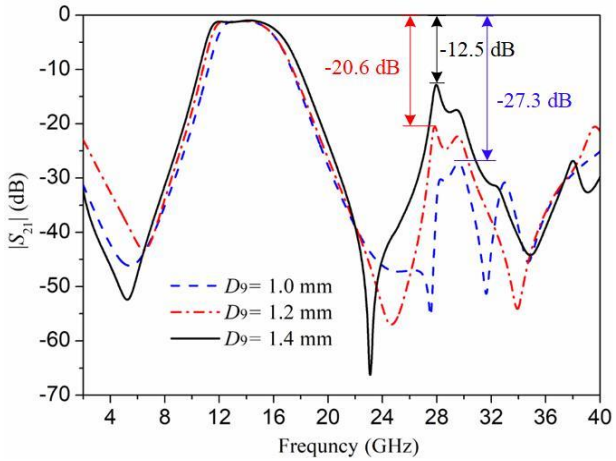

(c)

Fig. 4.9. (a) Voltage distribution of the quarter-wavelength resonator used in the proposed BPF (b) Electric field distribution of the proposed filter at the resonant frequency of third harmonic mode when ① D_9=1.4 mm and ② D_9=1 mm and (c) Simulated $|S_{21}|$ against D_9.

Fig. 4.9(a) reveals the structure of the quarter-wavelength resonator used in the proposed BPF. A short-circuited stepped impedance stub is loaded at the trisection point of this resonator near to the input terminal. The electrical lengths of the quarter-wavelength transmission line are referred to as θ_1 and $2\theta_1$, respectively. The short-circuited stub position can be defined by analyzing the voltage distributions of the fundamental mode and the third harmonic to improve the out-of-band suppression. It is obvious that the shorted terminal of the quarter-wavelength resonator is the common voltage zero point of the fundamental mode and the third harmonic mode, while the trisection point near the input terminal is the zero-voltage point only for third harmonic modes. When the shorted stub is located at the zero-voltage point of the third harmonic mode, the third harmonic mode signal will not get through the resonator, as shown in Fig. 4.9(b). Thus, out-of-band suppression can be developed by adjusting the location of the loaded stub. In Fig. 4.9(c), with the decrease of D_9 from 1.3 mm to 1 mm, the loaded stub approaches the zero-voltage point of the third harmonic mode gradually, and the out-of-band suppression is improved from 12.5 dB to 27.3 dB.

4.2.2.5 Measurement Results

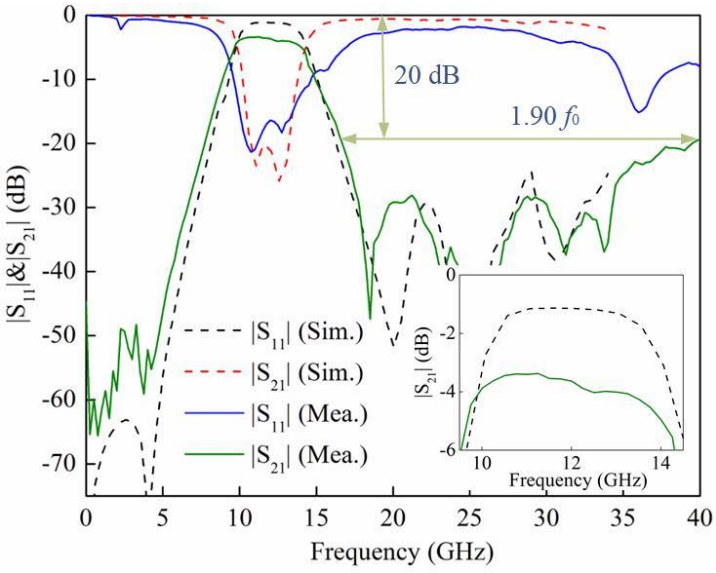

Fig. 4.10. Simulated and measured frequency response with a zoom-in view of the passband insert loss of the AME printed BPF.

The performance of the designed BPF is measured from 1 GHz up to 35 GHz. Good agreement between the simulated and measured results can be observed in Fig. 4.10. Dielectric constant and loss tangent of the additively manufactured substrate are 2.8, and 0.013, respectively. The conductivity of the silver film is 3.15×10^6 - 2.52×10^7 σ (S/m) at 20 °C. As demonstrated in Fig. 4.10, compared with the simulated results achieved by HFSS, the measured insertion loss and return loss are 3.42 dB and 16.65 dB at the center of 12.25 GHz, respectively. In the measurement, the connection between the SMK connector and the filter will cause inter-connection loss, which will lead to a deteriorated insertion loss. At the same time, the error of the thickness in the manufacturing process explains the deteriorated insertion loss. A 3-dB bandwidth is achieved from 9.58 GHz to 14.57 GHz with an FBW of 40.8%. Two TZs located at 3.51 and 18.51 GHz that can improve the selectivity are generated. In addition, due to the loaded short-circuited stepped impedance stub, the upper stopband with more than 20 dB rejection level is extended to 23.24 GHz (from 16.65 to 39.89 GHz) or 1.90 f_0. As can be seen, the designed BPF working at 12.25 GHz has the merits of multiple transmission zeros and poles, a compact size, and a wide stopband that can be assigned to television programs or utilized in radar detection and satellite communications.

Table 4.1 summarizes the comparison of the proposed BPF with other state-of-the-art BPFs fabricated with alternative fabricated processes. Compared with [2], the BPF proposed in our work has a larger FBW, two flexibly designed transmission zeros, a wider stopband, and a smaller size. Compared with traditional multi-layer processes, such as CMOS and LTCC technology, the proposed BPF has a good FBW, high-band and low-band TZs, a good stopband, and a competitive footprint. Furthermore, AME solution used in this thesis has the advantages of a low-cost and short processing cycle.

TABLE 4.1 COMPARISON WITH SOME OTHER BPFS

Ref.	f_0 (GHz)	Insertion Loss (dB)	*FBW (%)	Number of TZs	Filter order	Stopband (GHz)	$\varepsilon_r/\tan\delta$	Size (mm^2)/ (λ_g^2)	Thickness (mm)/ (λ_g)	Fabricated process
[2]	1.6	1	22	0	4	0.25 f_0 (20dB)	2.75/0.015	20×83/0.177 ×0.735	3.6/0.032	Additive manufacturing
	2.45	2	12	0	4	0.16 f_0 (20dB)	2.35/0.02	11.15×50/0.1 40×0.626	3.6/0.045	
[11]	33	2.6	42.4	0	1	1.58 f_0 (20dB)	N.A.	0.11×0.28/N. A.	N.A.	0.13-μm (Bi)-CMOS
[12]	59.5	3.3	21.68	2	2	N.A.	N.A.	0.240×0.225/ 0.144×0.135	N.A.	0.18-μm CMOS
[24]	4.3	1.1	44.2	1	3	2.6 f_0 (20dB)	5.9/N.A.	12×6 /0.418×0.020 9	1/0.035	LTCC
This wor k	12.25	3.42	40.8	2	2	1.9 f_0 (20dB)	2.8/0.013	2.7×1.425/0. 186×0.098	0.508/0.04	AME solution

*FBW= fractional Bandwidth

4.3 Vertically Integrated Multi-Layer Composite Right/ Left-Handed Broadband Devices

The current 5G rollout race is driving revolutionary fabrication methods that can construct electronics with high accuracy, low cost and involve only a short production circle. In particular, additive manufacturing technology is knocking on the door, ready to change the way we fabricate electronics with advanced design capability. Moreover, with the development of technology, multi-material additive manufacturing solutions that can fabricate conductive and dielectric materials simultaneously, have been widely used in the fabrication of electronics. Examples are components [24-26], transmission lines [27-30], bandpass filters [31-33], antennas [34-38], lens [39], and metasurfaces [40]. Multi-material additive manufacturing solutions can accurately print specific metal shapes at the target position without size and position errors and can simplify the fabrication process. Especially, an additively manufactured electronics solution that can fabricate seamless multi-metal-layer in a single substrate is introduced to fabricate microwave components [32-33], [37-40]. However, it is still a challenge to utilize this solution to fabricate microwave devices with low insertion loss due to the high loss tangent of the dielectric material used by this printing system.

Left-handed (LH) material is a kind of metamaterial with simultaneously negative permittivity (ε) and permeability (μ). In general, the composite right/left-handed (CRLH) structure represents the practical left-handed (LH) materials, which also

include right-handed (RH) effects that occur naturally. Recently, the CRLH transmission line (TL) has become a ‘hot spot’ in the design of novel and compact microwave devices because of its unique dispersion characteristic and advantages of wide bandwidth and low loss. According to current literature, CRLH structures have been applied in the design of transmission lines [41-42], power dividers [43-44], resonators [45-46], couplers [47-48], antennas [49-50], and power amplifiers [51]. In particular, multi-layer CRLH devices using different fabrication methods have been proposed to further reduce the size of metamaterial circuits [52-55]. For example, in [52], a multi-layer fully integrated solid-state CRLH metamaterial transmission line medium is presented with super compactness, which makes it well suited for Si RF/MMIC applications. Reference [53] proposed a diplexer composed of two super-compact multi-layered CRLH TLs, which presents the advantage of providing a large electrical length over an extremely short TL length and small transverse footprint.

This section describes the operating and design principles for vertically integrated multi-layer CRLH broadband transmission lines (TLs), and bandpass filters and couplers based on these vertically integrated CRLH TLs are designed and proposed. Good performance of the proposed devices with low loss and broad operational band can be obtained.

4.3.1 Vertically Integrated Composite Right/ Left-Handed Broadband Transmission Lines

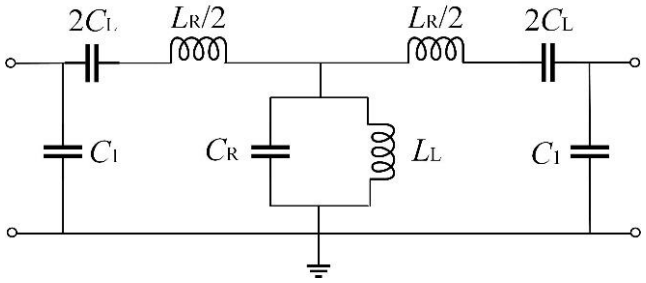

(a)

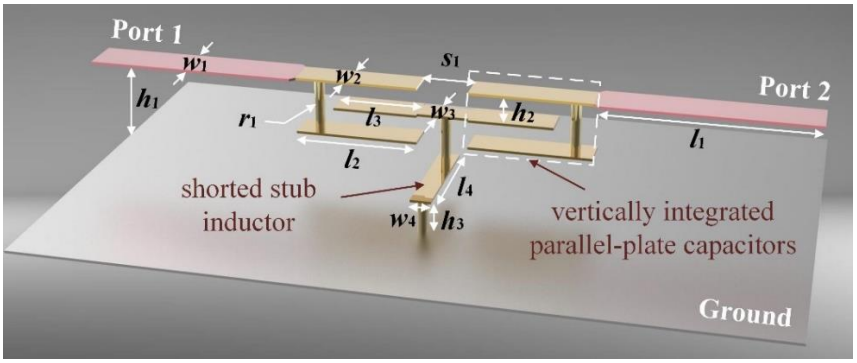

(b)

4.11. (a) Equivalent circuit model of CRLH TL. (b) Structure of vertically integrated multi-layer CRLH TL.

As shown in Fig. 4.11(a), a vertically integrated multi-layer CRLH TL is proposed and simulated. Compared with traditional planar single-layer CRLH TL, the planar interdigital capacitor is replaced by vertically integrated parallel-plate capacitors to improve the coupling series capacitance values. By reducing the distance between parallel plates, constant capacitance can be realized in smaller sizes, and this contributes to a small-size LH structure. A shorted stub inductor is added to realize the LH shunt inductance. Advantages of compact size, low insertion loss and broad operational band can be obtained with this vertically integrated multi-layer CRLH TL structure. The structure dimensions are labeled in the figure caption, with the impedances of the input and output parts being both 50 Ω.

To confirm the viability of the concept, the equivalent circuit model of the proposed

vertically integrated multi-layer CRLH TL has been extracted in Fig. 4.11(b). As we know, the typical equivalent circuit model of a planar CRLH TL consists of left-handed series capacitances C_L, left-handed shunt inductances L_L, right-handed series inductances L_R and right-handed shunt capacitances C_R [30]. However, the equivalent circuit model of the proposed vertically integrated multi-layer CRLH TL has extra shunt capacitances C_1, which represents the coupling between the parallel-plate capacitors and the ground layer.

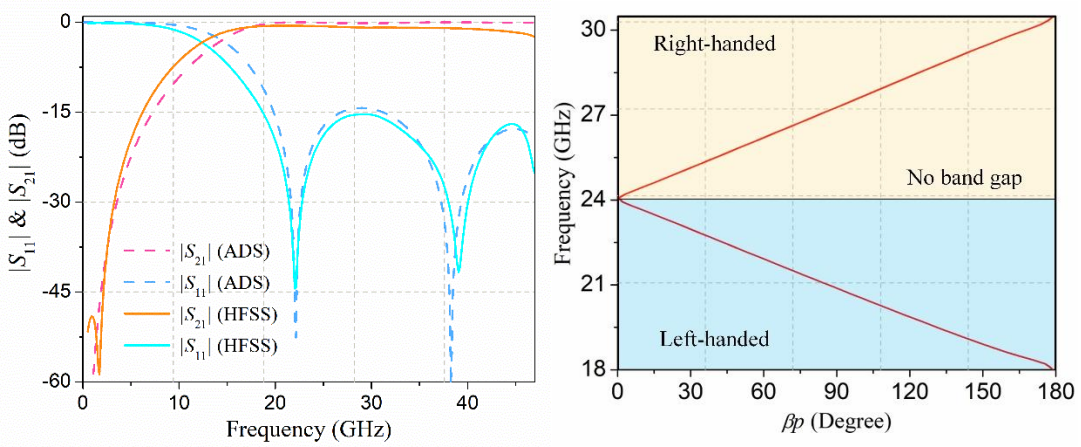

(a) (b)

Fig. 4.12. (a) Full-wave EM simulation frequency responses of the vertically integrated CRLH TL, compared with simulation frequency responses of equivalent circuit modal using ADS. (b) Dispersion diagram extracted by full-wave simulation.

In Fig. 4.12(a), the simulated frequency responses of the vertically integrated CRLH TL using finite element electromagnetic field simulation analysis software, ANSYS High-Frequency Structure Simulator (HFSS), have been illustrated. The equivalent LC-circuit is optimized to match the simulation result of the EM structure. Good agreement can be obtained between the simulated results of equivalent LC-circuit carried by ADS and the simulated results of the EM structure. The 1-dB bandwidth of the magnitude of the transmission coefficient S_{21} covers 14.9 GHz to 43.6 GHz and the 15 dB passband of the magnitude of the refraction coefficient S_{11} covers from 18.7-47.8 GHz with a dielectric loss tangent of 0.013. After optimization, the values of lumped elements in equivalent circuit can be obtained: L_L= 0.141 nH, L_R=0.354 nH, C_L=0.254

nH, C_R=0.248, nH, C_l=0.089 pF.

Fig. 4.12(b) illustrates the dispersion characteristics of the proposed vertically integrated multi-layer CRLH transmission line based on the simulated results, calculated by (with period p) [46]:

$$\beta p = \cos^{-1}\left[\frac{1-S_{11}S_{22}+S_{12}S_{21}}{2S_{21}}\right] \tag{4-14}$$

There is a seamless transition from LH to RH for dispersion characteristics of the transmission line. The balanced case exists because propagation constant γ is always purely imaginary. As a result, the balanced CRLH TL's dispersion curve does not have a stop-band. It can be seen that the structure exhibits a left-handed frequency bandwidth from 18 to 24 GHz.

4.3.2 Vertically Integrated Composite Right/ Left-Handed Broadband Bandpass Filter

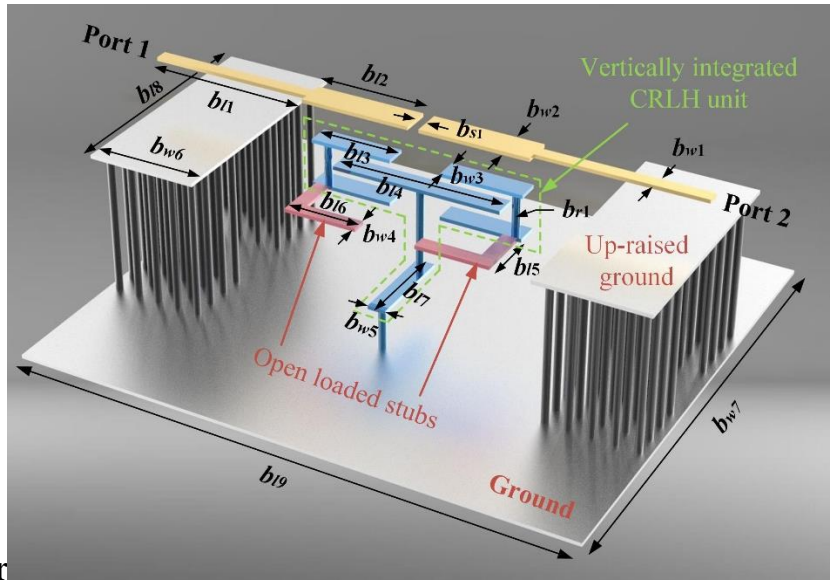

(a)

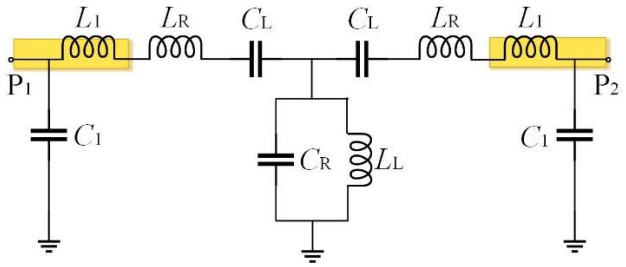

(b)

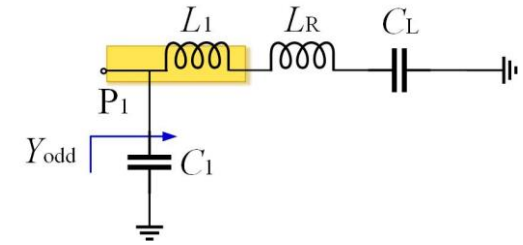

(c)

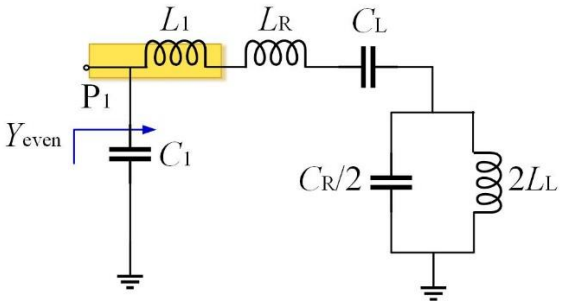

(d)

Fig. 4.13. (a) Schematic and equivalent circuit of the proposed CRLH resonator and its (b) Odd-mode equivalent circuit and (c) Even-mode equivalent circuit

Fig. 4.13(a) presents the 3D view of the proposed CRLH resonator. Four metal layers are employed to design the resonator, where the loaded stubs are located at the third layer. The resonator consists of two open-loaded stubs and a CRLH unit. L_1 and C_1 denote the impedance segment of the open loaded stub and the equivalent model of homogeneous CRLH TL is introduced to analyze the CRLH unit. Finally, Fig. 4.13(b) depicts the equivalent circuit of the proposed CRLH resonator. Odd- and even-mode method is introduced to deduce the resonance properties of the three-dimension CRLH resonator due to its symmetrical construction. The location of the odd- and even-mode resonant frequencies can be obtained by analyzing the equivalent circuit of resonators. In the proposed design, the odd- and even-mode circuits can be obtained, as shown in Fig. 4.13(c) and (d). Judging by the equivalent circuits, the input admittance can be expressed as:

$$Y_{odd} = j\omega C_1 + \frac{j\omega C_L}{1-\omega^2(L_1+L_R)C_L} \tag{4-15}$$

$$Y_{even} = j\omega C_1 + \frac{j\omega C_L(1-\omega^2 C_R L_L)}{1-\omega^2 C_L[(L_1+L_R+2L_L-\omega^2 C_R L_L(L_1+L_R)]-\omega^2 C_R L_L} \quad (4\text{-}16)$$

As we know, the odd- and even-mode resonant frequencies are determined by

$$Y_{odd} = Y_{even} = 0 \quad (4\text{-}17)$$

Combining equations (1), (2), and (3), we can see that the odd-mode resonant frequency f_{odd} is the function of the C_1, L_1, L_R and C_L, which is equivalent to the loaded stubs and the interdigital structure of the CRLH unit. Meanwhile the even-mode resonant frequency f_{even} is the function of both C_1, L_1, L_R, C_L and L_L, C_R. Compared with the presented EM structure, C_1 and L_1 correspond to the physical length of l_4. L_R, C_L correspond to l_1. L_L and C_R correspond to l_5. Fig. 4.14 depicts the simulated responses against l_1, l_4 and l_5, respectively, under the weak coupling situation to validate the expression of f_{odd} and f_{even}. Thus, as observed in Figs. 4.14(a) and (b), when l_1 or l_4 is altered, both the f_{odd} and f_{even} changed. What is more, in Fig. 4.14(c), f_{even} can be regulated by tuning the value of l_5, whereas f_{odd} remains constant. These simulated responses are consistent with deducing the Odd- and even-mode method.

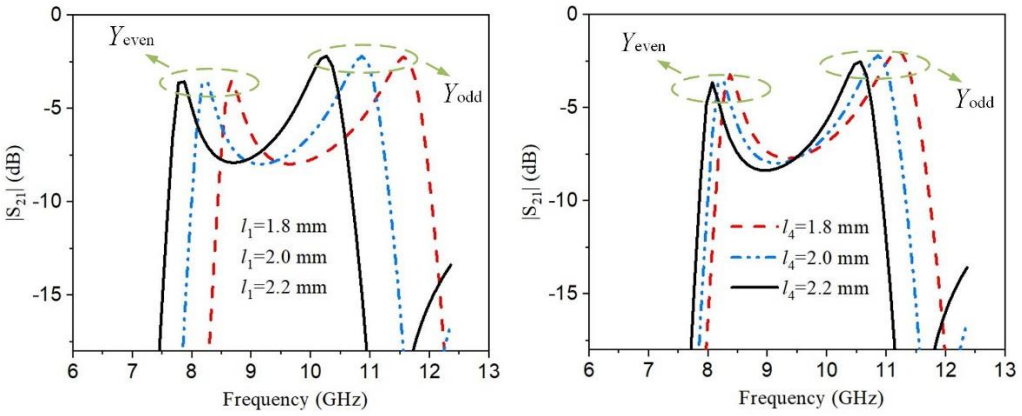

(a) (b)

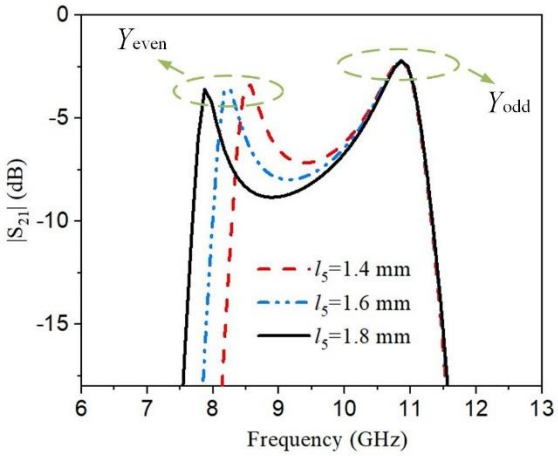

(c)

Fig. 4.14. Simulated responses against (a) l_1, (b) l_4 and (c) l_5.

After optimized, the parameters of the proposed resonator are determined as follows (all in mm): l_1=2.22, l_2=4.84, l_3=1.1, l_4=1.6, l_5=2.5, w_1=0.6, w_2=0.4, w_3=0.5, r_1=0.1. The dimension of BPF excluding feeding lines is 5.8 mm × 2.1 mm × 0.89 mm or 0.269λg × 0.097λg× 0.041λg, where λg is the guided wavelength at the center frequency.

(a)

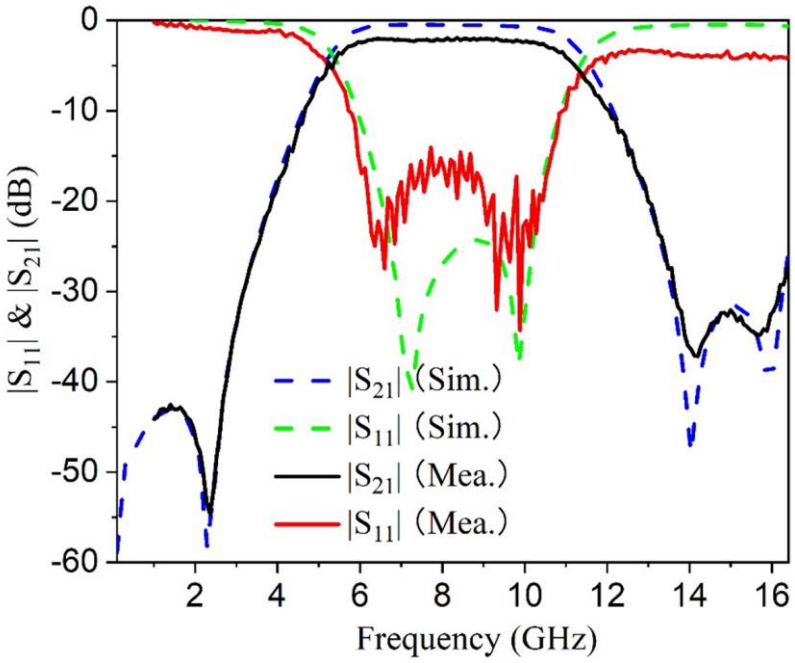

(b)

Fig. 4.15. (a) Photograph of the additively manufactured BPF and (b) the simulated and measured frequency response of the BPF.

Finally, Fig. 4.15(a) shows the photograph of an additively manufactured prototype with two up-raised grounds connected to the RF ground by 24 vias, respectively, to adjust the impedance match. The simulated and measured results of the proposed BPF are depicted in Fig. 4.15(b).

Two controllable resonant poles and three transmission zeros are excited. For the measurement result, the center frequency of the proposed BPF is 8.23 GHz and a 3-dB bandwidth is achieved from 5.14 GHz to 11.32 GHz with an FBW of 75.6%. Meanwhile, the measured insertion loss and return loss at the center frequency are 1.9 dB and 15.3 dB, respectively. The measured insertion loss is worse than the simulated one, which is mainly caused by the interconnection loss between the SMK connectors and the filter. In addition, the thickness errors in the manufacturing process contribute to a deteriorated insertion loss.

In our design, the dielectric constant of the additively manufactured substrate is 2.8, while the loss tangent is 0.013. However, the loss tangent of Rogers 5880, a commonly used dielectric material in traditional PCB processing, is only 0.0009. Compared with

the Rogers 5880, the value of loss tangent of the materials used in the AME solution is dozens of times Rogers 5880. The high loss tangent of the AME materials challenges us in designing the PCB board since lots of energy radiates to the substrate, especially in the design of the micro-strip electronic circuits, such as BPF, transmission lines, and couplers. For example, in this section, we use the broadside coupling to increase the Q value of a BPF and strengthen the coupling between the feed lines and the resonator. However, the performance of the BPF is still not competitive enough in the commercial market due to the high loss tangent of the dielectric material.

Therefore, the high loss tangent of AME dielectric materials needs to be improved urgently. I believe that if the loss tangent of the AME dielectric material can be reduced, then higher-frequency and feature-richer devices can be designed and fabricated with the AME solution. At that time, AME solutions will revolutionize the manufacturing method of electronic devices by taking advantage of flexible manufacturing freedom, low cost, time-saving, and good electrical performance.

4.4. Conclusion

In summary, a 3D-printed BPF based on multi-layer inductance and capacitance components is proposed in this chapter. Equivalent circuits and Kirchhoff's voltage law are used for analyzing the frequency response of the printed BPF. According to the measured results, it has outstanding stopband rejection, but the insertion loss and in-band flatness is not so competitive. Reducing the energy loss of the signal during propagation is always significant for electronics design. Especially for the AME solution, it is a challenge to reduce the loss with a high loss tangent of 0.013. For this reason, additively manufactured broadband vertically integrated CRLH TL and BPF are proposed in this chapter as well. This BPF has lower insertion loss and great in-band flatness compared with the BPF based on inductance and capacitance components. Odd-and even mode method is introduced to deduce the resonant frequencies of the BPF.To validate this, simulation of controllable response against related parameters is

shown as well. Finally, Good agreements can be observed between the EM simulated and measured results that validate the feasibility of the proposed 3D printing solution for manufacturing complex multilayer microwave devices in circuit-in-package applications.

4.5 References

[1] F. Cai, Y. Chang, K. Wang, C. Zhang, B. Wang and J. Papapolymerou, "Low-loss 3-D multilayer transmission lines and interconnects fabricated by additive manufacturing technologies," *IEEE Trans. Microw. Theory Techn.,* vol. 64, no. 10, pp. 3208–3216, Oct. 2016, doi: 10.1109/TMTT.2016.2601907.

[2] A. Vallecchi, D. Cadman, W. G. Whittow, J. Vardaxoglou, E. Shamonina and C. J. Stevens, "3-D printed bandpass filters with coupled vertically extruded split ring resonators," *IEEE Trans. Microw. Theory Techn.,* vol. 67, no. 11, pp. 4341-4352, Nov. 2019, doi: 10.1109/TMTT.2019.2934456.

[3] Y. Gu, D. Park, S. Gonya, J. Jendrisak, S. Das and D. R. Hines, "Direct-write printed broadband inductors," *Addit. Manuf.,* vol. 30, 100843, Dec. 2019, doi: 10.1016/j.addma.2019.100843.

[4] P.F. Flowers, C. Reyes, S. Ye, M. J. Kim and B. J. Wiley, "3D printing electronic components and circuits with conductive thermoplastic filament," *Addit. Manuf.,* vol. 18, pp. 156-163, Dec. 2017, doi: 10.1016/j.addma.2017.10.002.

[5] P. Pa, Z. Larimore, P. Parsons and M. Mirotznik, "Multi-material additive manufacturing of embedded low-profile antennas," *Electron. Lett.*, vol. 51, no. 20, pp. 1561-1562, 2015, doi: 10.1049/el.2015.2186.

[6] J. Zhu, Y. Yang, S. Li, S. Liao and Q. Xue, "Single-ended-fed high-gain LTCC planar aperture antenna for 60 GHz antenna-in-package applications," *IEEE Trans. Ant. and Propag.,* vol. 67, no. 8, pp. 5154-5162, Aug. 2019, doi: 10.1109/TAP.2019.2917591.

[7] Z. Chen, Y. P. Zhang, A. Bisognin, D. Titz, F. Ferrero and C. Luxey, "A 94-GHz dual-polarized microstrip mesh array antenna in LTCC technology," *IEEE Antennas Wirel. Propag. Lett.,* vol. 15, pp. 634-637, 2016, doi: 10.1109/LAWP.2015.2465842.

[8] J. Xu and X. Y. Zhang, "Compact high-isolation LTCC diplexer using common stub-loaded resonator with controllable frequencies and bandwidths," *IEEE Trans. Microw. Theory Techn.,* vol. 65, no. 11, pp. 4636-4644, Nov. 2017, doi: 10.1109/TMTT.2017.2697855.

[9] X. Dai, X. Y. Zhang, H. Kao, B. Wei, J. Xu and X. Li, "LTCC bandpass filter with wide stopband based on electric and magnetic coupling cancellation," *IEEE Trans. Compon. Packag. Manuf. Technol,* vol. 4, no. 10, pp. 1705-1713, Oct. 2014, doi: 10.1109/TCPMT.2014.2346240.

[10] B. Zhang, D. Titz, F. Ferrero, C. Luxey and Y. P. Zhang, "Integration of quadruple linearly-polarized microstrip grid array antennas for 60-GHz antenna-in-package applications," IEEE *Trans. Compon. Packag. Manuf. Technol.,* vol. 3, no. 8, pp. 1293-1300, Aug. 2013, doi: 10.1109/TCPMT.2013.2255333.

[11] Y. Yang, H. Liu, Z. J. Hou, X. Zhu, E. Dutkiewicz and Q. Xue, "Compact on-chip bandpass filter with improved in-band flatness and stopband attenuation in 0.13-μm (Bi)-CMOS technology*," IEEE Electron.Device Lett.,* vol. 38, no. 10, pp. 1359-1362, Oct. 2017, doi: 10.1109/LED.2017.2739186.

[12] A. S. El-Hameed, A. Barakat, A. B. Abdel-Rahman, A. Allam, and R. K. Pokharel, "Ultracompact 60-GHz CMOS BPF employing broadside-coupled open-loop resonators," *IEEE Microw. Wireless Compon. Lett.,* vol. 27, no. 9, pp. 818–820, Sep. 2017, doi: 10.1109/LMWC.2017.2734771.

[13] M. Li, Y. Yang, K. D. Xu, X. Zhu and S. W. Wong, "Microwave on-chip bandpass filter based on hybrid coupling technique," *IEEE Trans. Electron Devices,* vol. 65, no. 12, pp. 5453-5459, Dec. 2018, doi: 10.1109/LMWC.2017.2734771.

[14] V. F. Tseng and H. Xie, "Increased multilayer fabrication and RF characterization of a high-density stacked MIM capacitor based on elective etching," *IEEE Trans. Electron Devices,* vol. 61, no. 7, pp. 2302-2308, July 2014, doi: 10.1109/TED.2014.2325491.

[15] Y. Li, L. Ge, J. Wang, B. Ai, M. Chen, Z. Zhang, Z. Li, "A Ka-band 3-D-printed wideband stepped waveguide-fed magnetoelectric dipole antenna array," *IEEE Trans. Antennas Propag.,* vol. 68, no. 4, pp. 2724-2735, April 2020, doi: 10.1109/TAP.2019.2950868.

[16] G. Wu, Y. Zeng, K. F. Chan, S. Qu and C. H. Chan, "3-D printed circularly polarized modified Fresnel lens operating at terahertz *frequencies*," *IEEE Trans. Antennas Propag.,* vol. 67, no. 7, pp. 4429-4437, July 2019, doi: 10.1109/TAP.2019.2908110.

[17] M. Laurila, B. Khorramdel and M. Mäntysalo, "Combination of e-jet and inkjet printing for additive fabrication of multilayer high-density RDL of silicon interposer," *IEEE Trans. Electron Devices.,* vol. 64, no. 3, pp. 1217-1224, March 2017, doi: 10.1109/TED.2016.2644728.

[18] G. Huang, C. Han, W. Xu, T. Yuan and X. Zhang., "A compact 16-way high-power combiner implemented via 3-D metal printing technique for advanced radio-frequency electronics system applications" *IEEE Trans. Ind. Electron.*, vol. 66, no. 6, pp. 4767-4776, June 2019, doi: 10.1109/TIE.2018.2863219.

[19] S. Kyung, J. Kwon, Y. Kim and S. Jung, "Low-temperature, solution-processed, 3-D complementary organic FETs on flexible substrate," in *IEEE* Trans. *Electron Devices*, vol. 64, no. 5, pp. 1955-1959, May 2017, doi: 10.1109/TED.2017.2659741.

[20] P. Rewatkar and S. Goel, "Next-generation 3D printed microfluidic membraneless enzymatic biofuel cell: cost-effective and rapid approach," *IEEE Trans. Electron Devices.,* vol. 66, no. 8, pp. 3628-3635, Aug. 2019, doi: 10.1109/TED.2019.2922424.

[21] Y. Sakabe, M. Hayashi, T. Ozaki and J. P. Canner, "High frequency performance of multilayer ceramic capacitors," *1995 Proceedings. 45th Electronic Components and Technology Conference,* Las Vegas, NV, USA, 1995, pp. 234-240, doi: 10.1109/ECTC.1995.514390.

[22] M. Li, Y. *Yang*, F. Iacopi, J. Nulman and S. Chappel-Ram, "3D-printed low-profile single-substrate multi-metal layer antennas and array with bandwidth enhancement,"

IEEE Access, vol. 8, pp. 217370-217379, 2020. doi: 10.1109/ACCESS.2020.3041232.

[23] M. Li, Y. Yang, Y. Zhang, F. Iacopi, S. Ram, J. Nulman, "A fully integrated conductive and dielectric additive manufacturing technology for microwave circuits and antennas," *the 50th European Microwave Conference (EuMC),* accepted, 2020.

[24] X. J. Zhang, H. H. Zhang, and X. P. Ma, "Design of compact wideband LTCC filter using pentagonal-shaped SIR," Electron. Lett., vol. 47, no. 5, pp. 327–328, Mar. 2011.

[25] P. F. Flowers, C. Reyes, S. Ye, M. J. Kim and B. J. Wiley, "3D printing electronic components and circuits with conductive thermoplastic filament," *Addit. Manuf.*, vol. 18, pp. 156-163, Dec. 2017.

[26] Y. Gu, D. Park, S. Gonya, J. Jendrisak, S. Das and D. R. Hines, "Direct-write printed broadband inductors," *Addit. Manuf.*, vol. 30, Dec. 2019.

[27] F. Cai, Y. Chang, and K. Wang *et al.*, "Low-loss 3-D multilayer transmission lines and interconnects fabricated by additive manufacturing technologies," *IEEE Trans. Microw. Theory Techn.,* vol. 64, no. 10, pp. 3208–3216, Oct. 2016.

[28] M. Abt, A. Roch, J. A. Qayyum, et al., "Aerosol-printed highly conductive Ag transmission lines for flexible electronic devices," *IEEE Trans. Compon., Package., Manuf. Technol.,* vol. 8, no. 10, pp. 1838-1844, Oct. 2018.

[29] P. I. Deffenbaugh, T. M. Weller and K. H. Church, "Fabrication and Microwave Characterization of 3-D Printed Transmission Lines," *IEEE Microw. Wireless Compon. Lett.,* vol. 25, no. 12, pp. 823-825, Dec. 2015.

[30] B. Urasinska-Wojcik, N. Chilton, P. Todd, C. Elsworthy, M. Bates, G. Roberts and G. J. Gibbons, "Integrated manufacture of polymer and conductive tracks for real-world applications," *Addit. Manuf.*, vol. 29, Oct. 2019.

[31] A. Vallecchi, D. Cadman, W. G. Whittow, J. Vardaxoglou, E. Shamonina and C. J. Stevens, "3-D printed bandpass filters with coupled vertically extruded split ring resonators," *IEEE Trans. Microw. Theory Techn.,* vol. 67, no. 11, pp. 4341-4352, Nov. 2019.

[32] M. Li, Y. Yang, F. Iacopi, M. Yamada and J. Nulman, "Compact multi-layer bandpass filter using low-temperature additive manufacturing solution," *IEEE Trans. Electron. Devices,* vol. 68, no. 7, pp. 3163-3169, July 2021.

[33] M. Li, Y. Yang, Y. Zhang, F. Iacopi, S. Ram and J. Nulman, "A fully integrated conductive and dielectric additive manufacturing technology for microwave circuits and antennas," *50th European Microwave Conference (EuMC),* Utrecht, Netherlands, 2021, pp. 392-395.

[34] B. K. Tehrani, B. S. Cook and M. M. Tentzeris, "Inkjet printing of multilayer millimeter-wave Yagi-Uda antennas on flexible substrates," *IEEE Trans. Antennas Propag.,* vol. 15, pp. 143-146, 2016.

[35] M. Kacar, T. M. Weller and G. Mumcu, "3D printed wideband multilayered dual-polarized stacked patch antenna with integrated MMIC switch," *IEEE Open Journal Antennas Propag.,* vol. 2, pp. 38-48, 2021.

[36] T. P. Ketterl et al., "A 2.45 GHz phased array antenna unit cell fabricated using 3-D multi-layer direct digital manufacturing," *IEEE Trans. Microw. Theory Techn.,* vol. 63, no. 12, pp. 4382-4394, Dec. 2015.

[37] M. Li, Y. Yang, F. Iacopi, J. Nulman and S. Chappel-Ram, "3D-printed low-profile single-substrate multi-metal layer antennas and array with bandwidth enhancement," *IEEE Access*, vol. 8, pp. 217370-217379, 2020.

[38] J. Zhu, Y. Yang, M. Li; D. McGloin, S. Liao, J. Nulman, M. Yamada and F. Iacopi., "Additively manufactured millimeter-wave dual-band single-polarization shared aperture Fresnel zone plate metalens antenna," *IEEE Trans. Antennas Propag.,* vol. 69, no. 10, pp. 6261-6272, Oct. 2021.

[39] A. C. Paolella, C. D. Fisher, C. Corey, D. Foster and D. Silva-Saez, "3-D printed millimeter-wave lens systems at 39 GHz," *IEEE Microw. Wireless Compon. Lett.,* vol. 28, no. 6, pp. 464-466, June 2018.

[40] J. Zhu, Y. Yang, N. Hu, S. Liao, and J.Nulman, " Additively manufactured multi-material ultrathin metasurfaces for broadband circular polarization decoupled beams and orbital angular momentum generation," *ACS Applied Materials & Interfaces,* vol. 13, no. 49, pp. 59460-59470, 2021.

[41] A. Lai, T. Itoh and C. Caloz, "Composite right/left-handed transmission line metamaterials," *IEEE Microwave Magazine*, vol. 5, no. 3, pp. 34-50, Sept. 2004.

[42] C. Caloz and T. Itoh, "Transmission line approach of left-handed (LH) materials and microstrip implementation of an artificial LH transmission line," *IEEE Trans. Antennas Propag.,* vol. 52, no. 5, pp. 1159-1166, May 2004.

[43] X. Ren, K. Song, M. Fan, Y. Zhu and B. Hu, "Compact dual-band Gysel power divider based on composite right- and left-handed transmission lines," *IEEE Microw. Wireless Compon. Lett.,* vol. 25, no. 2, pp. 82-84, Feb. 2015.

[44] M. Bemani and S. Nikmehr, "Dual-band N-way series power divider using CRLH-TL metamaterials with application in feeding dual-band linear broadside array antenna with reduced beam squinting," *IEEE Trans. Circuits Syst. I, Reg. Papers.,* vol. 60, no. 12, pp. 3239-3246, Dec. 2013.

[45] Y. Kushiyama, T. Arima and T. Uno, "Differential-type CRLH leaky-wave antenna using stepped impedance resonators," *IEEE Antennas Wireless Propag. Lett.,* vol. 15, pp. 321-324, 2016.

[46] N. Amani and A. Jafargholi, "Zeroth-order and TM_{10} modes in one-unit cell CRLH mushroom resonator," *IEEE Antennas Wireless Propag. Lett.,* vol. 14, pp. 1396-1399, 2015.

[47] C. Caloz and T. Itoh, "A novel mixed conventional microstrip and composite right/left-handed backward-wave directional coupler with broadband and tight coupling characteristics," *IEEE Microw. Wireless Compon. Lett.,* vol. 14, no. 1, pp. 31-33, Jan. 2004.

[48] A. Hirota, Y. Tahara and N. Yoneda, "A compact forward coupler using coupled composite right/left-handed transmission lines," *IEEE Trans. Microw. Theory Techn.,* vol. 57, no. 12, pp. 3127-3133, Dec. 2009.

[49] B. Zong, G. Wang, Y. Wang, L. Geng and D. Wang, "Compact antenna using finger-connected interdigital capacitor-based composite right/left-handed transmission-line unit cell," *IEEE Trans. Antennas Propag.,* vol. 64, no. 5, pp. 1994-1999, May 2016.

[50] J. H. Choi and T. Itoh, "Dual-band composite right/left-handed (CRLH) phased-array antenna," *IEEE Antennas Wireless Propag. Lett.,* vol. 11, pp. 732-735, 2012.

[51] Q. Cai, W. Che, G. Shen and Q. Xue, "Wideband high-efficiency power amplifier using D/CRLH bandpass filtering matching topology," *IEEE Trans. Microw. Theory Techn.,* vol. 67, no. 6, pp. 2393-2405, June 2019.

[52] Z. Hu, P. D. Curtis and W. Tong, "A multilayer compact solid state composite right/left-handed metamaterial transmission line," *IEEE Electron Device Lett.,* vol. 29, no. 12, pp. 1383-1385, Dec. 2008.

[53] Y. Horii, C. Caloz and T. Itoh, "Super-compact multilayered left-handed transmission line and diplexer application;" *IEEE Trans. Microw. Theory Techn.,* vol. 53, no. 4, pp. 1527-1534, April 2005.

[54] Nasimuddin, Z. N. Chen and X. Qing, "Multilayered composite right/left-handed leaky-wave antenna with consistent gain," *IEEE Trans. Antennas Propag.,* vol. 60, no. 11, pp. 5056-5062, Nov. 2012.

[55] S. Gupta, D. L. Sounas, H. V. Nguyen, Q. Zhang and C. Caloz, "CRLH–CRLH C-section dispersive delay structures with enhanced group-delay swing for higher analog signal processing resolution," *IEEE Trans. Microw. Theory Techn.,* vol. 60, no. 12, pp. 3939-3949, Dec. 2012.

Chapter 5 3D-Printed Metasurfaces for Independent Manipulation of Broadband Orbital Angular Momentum

5.1 Introduction

Metamaterials for electromagnetic (EM) wave manipulation have attracted much attention for their unprecedented capabilities to achieve benefits beyond what is possible with conventional materials [1]. They are usually composed of subwavelength artificially engineered structures by periodic arrangements [2]. Metasurfaces, as a kind of planar version of metamaterial [3-6], are being widely investigated to manipulate the wavefront for polarization conversion,[7-9] beam deflection [10-12], beam splitting [13-15], beam shaping [16-17], vortex beam generation [18-22], absorption enhancement [23-26], holography [27-32], and reflectors [33]. Vortex beams have attracted much attention due to their excellent performance in high-speed wireless communications. Vortex beams are also called orbital angular momentum (OAM) beams. Their rotational phase front can create a vortex momentum along the beam axis.[21] Vortex beams with different OAM modes are orthogonal to each other. Thus, OAM technology can significantly improve the information capacity by allowing multiple beams with different modes to be multiplexed together and transmitted over the same channel with ultralow crosstalk.

Conventional metasurfaces usually have a single function and can only produce a single EM wave that can barely satisfy the requirements of next-generation wireless communication systems. Therefore, multifunctional metasurfaces have been pursued to enhance information capacity.[34-38] In addition, digital coding metasurface does connect physics and information science.[39-43] For example, a multifunctional digital coding metasurface can perform optical illusion, scattering reduction, and generation of orbital angular momentum within a shared aperture [39]. Three different elements are introduced to control the digital states of three frequency bands. The metasurface has different transmission routes at each working frequency, avoiding path

degradation and guaranteeing high-quality information transmission. However, since these three elements are fabricated in the same conductive layer using a shared aperture, there are restrictions on selecting the element shapes. It should be noted that avoiding overlaps in the conventional 2D spatial arrangement of the three elements is challenging. For this reason, multi-layer structures are more desirable when designing multifunctional metasurfaces. For example, a broadband achromatic transmission-reflection-integrated focusing metasurface is designed for transmission and reflection mode at different bands[40]. However, since the discussed sample[40] was layer fabricated through the standard printed-circuit-board (PCB) technique and assembled with teflon screws and nuts, the metasurface profile increases, and the manufacturing process becomes complicated. In recent years, additive manufacturing (AM) has been widely applied for designing metasurfaces[44-50], providing 3D customizable design flexibility, low-cost, fast-prototyping, and distributed production cycle in the telecommunication industry, and low profile even when multilayered.

Demonstrated here are two additively manufactured (AM) metasurfaces. A novel multi-material conductive and dielectric AM technology is introduced to fabricate the metasurface with an ultra-thin profile and multiple conductive metals (silver nanoparticle) layers in a single dielectric (acrylates) substrate. First, an AM multi-material conductive and dielectric multifunctional metasurface is presented, generating orbital angular momentum (OAM) states at two broad operational bands with different topological charges. Digitalization-coding of meta-atoms is realized in this metasurface to simplify the design and optimization procedures. Each meta-atom consists of four silver layers embedded in a dielectric substrate formed by acrylates. The silver patterns on the four layers correspond to two 3-bit coding cells (for higher and lower bands, respectively), a frequency selective surface (FSS), and a full ground.

The embedded FSS structure isolates the mutual coupling between the coding cells working at the lower and higher bands. Finally, a metasurface is additively manufactured using piezoelectric print head technology to realize two OAM states at V-band and W-band, respectively, for high-information capacity and high-security

applications. A reflective metasurface for pencil beam generation at two operational bands is designed and fabricated further to verify: firstly, the isolation effects of the FSS; and, secondly, the possibility of developing other functional devices with the proposed meta-atoms.

5.2 The Method for Dual-Broadband Metasurface with Simultaneous Functions

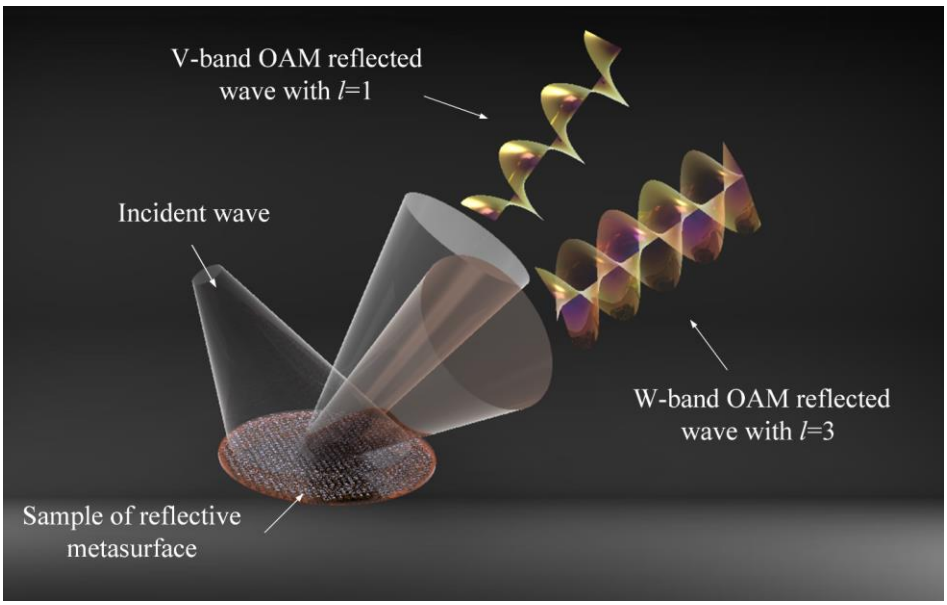

(a)

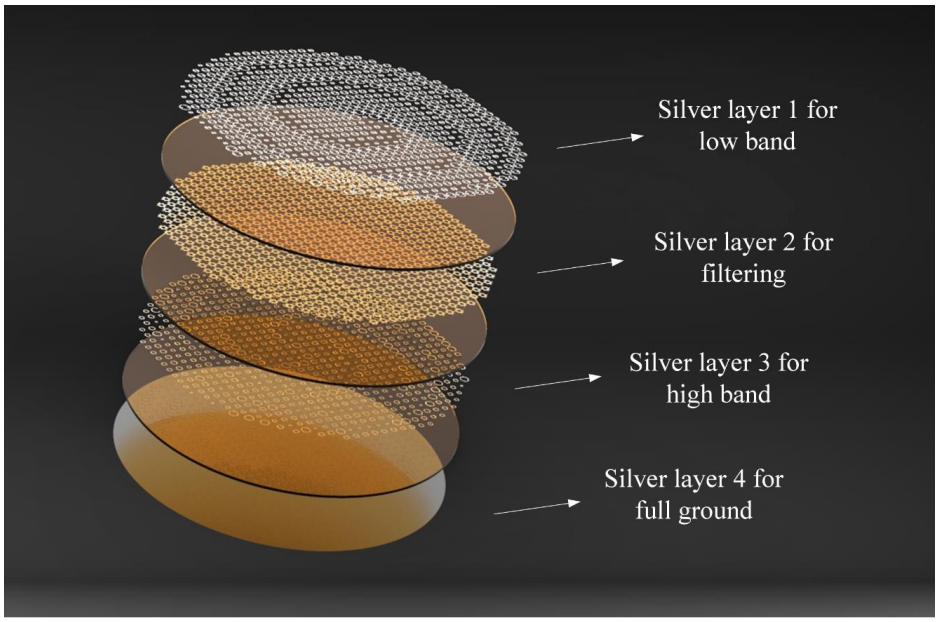

(b)

Fig. 5.1. Schematic image of the designed broadband multifunctional metasurface. (a) The concept for the multifunctional metasurface. (b) Construction of the multifunctional metasurface, done with four-silver-layer surfaces and three dielectric layers.

A dual-broadband multi-silver-layer metasurface with an ultra-thin profile operating at millimeter-wave, as shown in Fig. 5.1(a) is designed, fabricated, and tested. Two orbital angular momentum (OAM) states are simultaneously realized with this metasurface at two frequency bands, 62-72 GHz (V-band) and 81-92 GHz (W-band), respectively, when excited by a spherical incident wave. The topological charge of the V-band is l=1, and the topological charge of the W-band is l=3. Devices operating at V-band and W-band can be widely applied in inter-satellite communication, ground short-range 5G communication, radar, and missile guidance technology. The topological charge of the V-band is l=1, and the topological charge of the W-band is l=3.

The proposed method opens opportunities to improve the information capacity of the coding metasurface on millimeter-wave applications. In Fig. 5.1(b), four-silver-layer surfaces separated by three dielectric layers are employed to fabricate the metasurfaces. The cells at the first and third silver layers corresponding to specific phase delays are utilized to manipulate V-band and W-band EM wavefronts. Layer 2 is a frequency selective surface (FSS) that ensures the metasurface operates independently in both frequency bands. A full ground is located at the bottom of the metasurface to realize the reflection. Taking advantage of additive manufacturing technology, four different silver layers and three dielectric layers are fabricated in a single substrate with an ultra-thin profile. Since the FSS is able to realize suppressed mutual coupling features, the dual-frequency metasurface design can be simplified to two single-frequency metasurface designs. Dual-broadband performance with independent manipulation of EM wavefronts can be achieved by coding cells in different layers. According to Fermat's principle of equality of electrical path lengths of incoming EM waves, phase compensation for pencil beam operating at lower and

higher bands of each cell can be obtained as written below[51]:

$$\varphi_{low}(x,y) = \frac{2\pi}{\lambda_{01}}\left(\sqrt{\left(x^2+y^2+{D_1}^2\right)}-D_1\right)+\varphi_{01} \tag{5-1}$$

$$\varphi_{high}(x,y) = \frac{2\pi}{\lambda_{02}}\left(\sqrt{\left(x^2+y^2+{D_2}^2\right)}-D_2\right)+\varphi_{02} \tag{5-2}$$

where D is the focal length, λ_0 represents wavelength in free space, and φ_0 is the initial phase at the original point. To excite different OAM beam states at lower and higher bands, extra phase compensations for vortex beams with different topological charges are added to each cell in layers 1 and 3, respectively. Thus, the desired phase compensation for the OAM beam of each cell in layer 1 and layer 3 can be expressed as:

$$\varphi_{low}(x,y) = \begin{cases} \frac{2\pi}{\lambda_{01}}\left(\sqrt{\left(x^2+y^2+{D_1}^2\right)}-D_1\right)+\varphi_{01}+l_1\times\tan^{-1}\left(\frac{y}{x}\right) & y>0 \\ \frac{2\pi}{\lambda_{01}}\left(\sqrt{\left(x^2+y^2+{D_1}^2\right)}-D_1\right)+\varphi_{01}+l_1\times\left(\frac{\pi}{2}+\tan^{-1}\left(\frac{y}{x}\right)\right) & y<0 \end{cases} \tag{5-3}$$

$$\varphi_{high}(x,y) = \begin{cases} \frac{2\pi}{\lambda_{02}}\left(\sqrt{\left(x^2+y^2+{D_2}^2\right)}-D_2\right)+\varphi_{01}+l_2\times\tan^{-1}\left(\frac{y}{x}\right) & y>0 \\ \frac{2\pi}{\lambda_{02}}\left(\sqrt{\left(x^2+y^2+{D_2}^2\right)}-D_2\right)+\varphi_{01}+l_2\times\left(\frac{\pi}{2}+\tan^{-1}\left(\frac{y}{x}\right)\right) & y<0 \end{cases} \tag{5-4}$$

where l_1 and l_2 equal 1 and 3, respectively, to generate OAM beams with topological charges of 1 and 3.

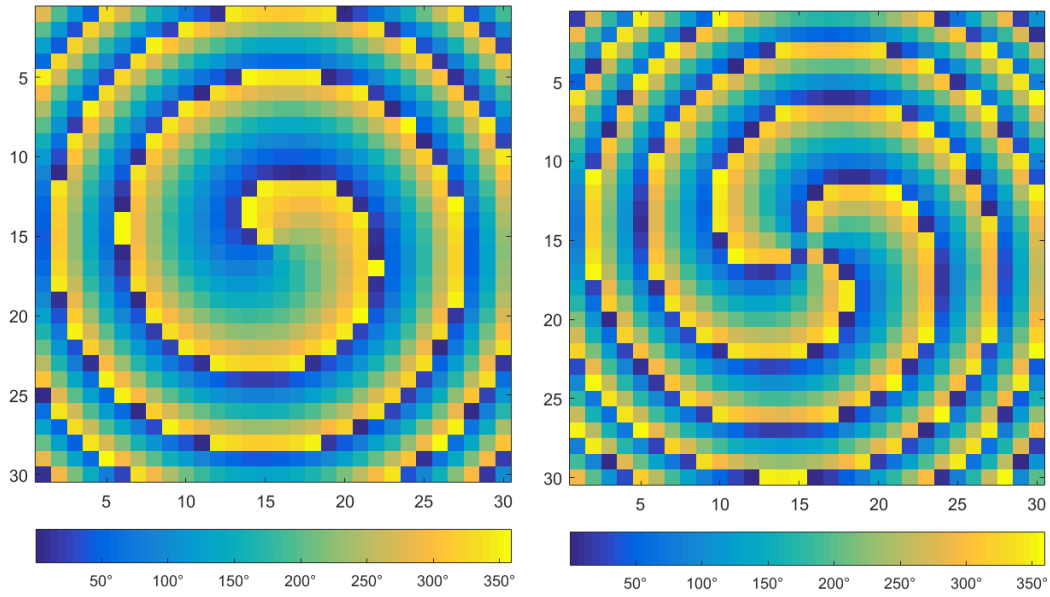

Fig. 5.2 (a) Compensating phase distribution at the metasurface aperture for layer 1 with a topological charge of 1 operating at V-band, and (b) Compensating phase distribution at the metasurface aperture for layer 3 with a topological charge of 3 operating at W-band. Every pixel on these distribution maps represents the required compensating phase delay with a focal length of 50 mm for the coding cell at this location. 30 × 30 coding cells are included in each map.

Figs. 5.2(a) and (b) show the obtained compensating phase at the metasurface apertures for layer 1 and layer 3, respectively. Then, they can be discretized by using coding cells that cover the 2π phase range. The aperture of the coding metasurface is set as a circular shape with a diameter of 70 mm. A standard WR12 rectangular waveguide is utilized to illuminate the reflective metasurface. The focal length is defined as 50 mm. Finally, the proposed metasurface can realize the independence of manipulating EM wavefronts for different OAM states with the proposed coding cells.

5.3 Design of the Dual Band Independent Controlled Coding Meta-Atom

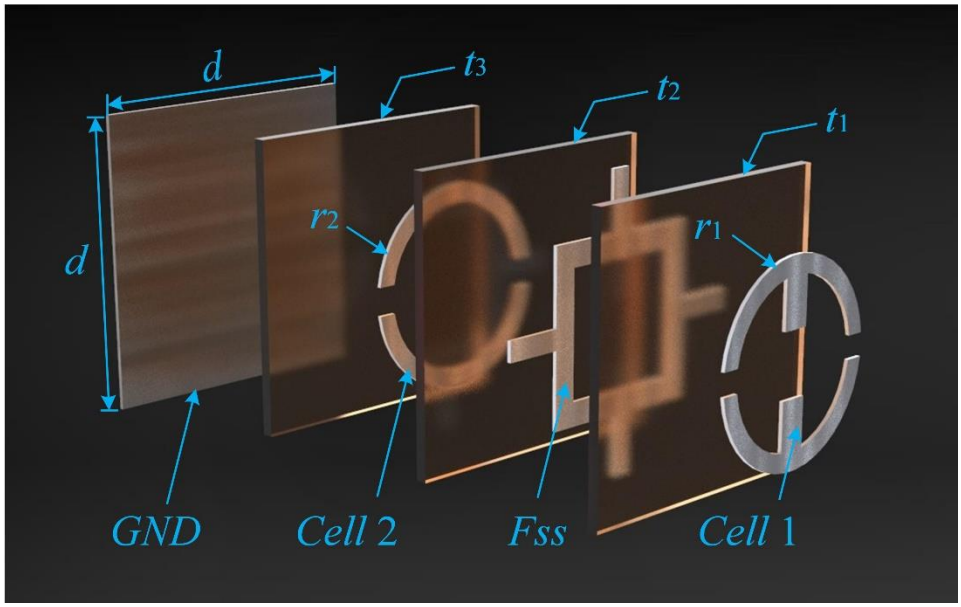

(a)

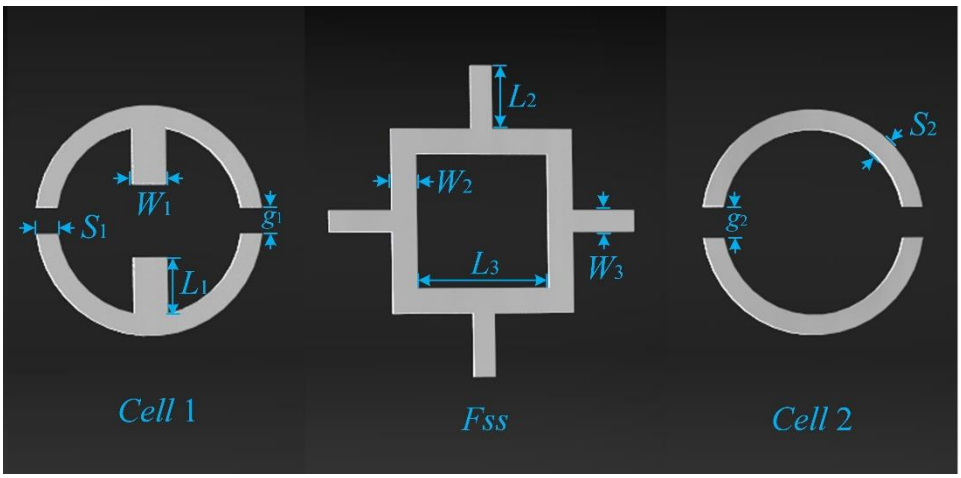

(b)

Fig. 5.3 (a) 3D view of the reflection coding meta-atoms sketch contains four silver-layer surfaces separated by three dielectric layers. (b) The detailed structure of the dual-band independent controlled coding meta-atoms. After optimization, the parameters are g_1=0.13 mm, g_2=0.2 mm, S_1=0.15 mm, S_2=0.15 mm, W_1=0.26 mm, W_2=0.21 mm, W_3=0.15 mm, L_1=0.44 mm, L_2=0.43 mm, L_3=0.92 mm, d = 2.2 mm.

Fig. 5.3(a) indicates the detailed structure of the dual-band independent controlled coding meta-atom composed of four silver layers separated by three dielectric layers. Cell 1 and 2 are the coding cells operating at V- and W- bands, respectively. Cell 1 is on the first silver layer, and cell 2 is on the third silver layer. The performance of EM waves is manipulated to realize functions at these two bands by varying the lengths of r_1 and r_2 of cell 1 and cell 2, respectively. The second silver layer is a frequency selective surface (FSS) consisting of a rectangular loop with four loaded stubs extended to the edge of the meta-atom, which can efficiently filter the transmitted EM waves. The fourth silver layer is full ground. To completely take the mutual coupling between the phasing cells and take the FSS structure into account in the cell design procedure, the period of cell 1, cell 2, and FSS structure are set as the same size (d = 2.2 mm). This way, all the possible phasing cell combinations can be simulated and analyzed. Spaces between adjacent silver layers are filled with dielectric material with relative permittivity of 2.8 and a loss tangent of 0.013[50]. As shown in Fig. 5.3(a), t_1= 0.33 mm, t_2=0.365 mm, and t_3=0.4 mm. The thickness of each silver layer is 0.035 mm. The total thickness of the proposed coding cell is 1.235 mm.

To better illustrate the reflective performance of the coding cell under the incident wave, we performed full-wave simulations using finite element electromagnetic field simulation analysis software, ANSYS High-Frequency Structure Simulator (HFSS), with master-slave boundary conditions. More details for the cells of the proposed meta-atom are displayed. As shown in Fig. 5.3(b), the layout of cell 1 consists of a ring with two gaps and two loaded stubs. Cell 2 consists of a ring with two gaps. FSS consists of a rectangular loop with four loaded stubs extended to the edge of the coding cell. Since the meta-atom is anisotropic along the x- and y-directions, phase responses of the coding cells with the x-and y-polarized incidences differ at the operating frequency bands. In this thesis, the x-polarized incidence is applied to illuminate the linear reflective cell. Loaded stubs of cell 1 are added to control the phase response in the direction of x-polarization. Finally, after optimization, the parameters are shown in Fig. 5.3(b).

(a)

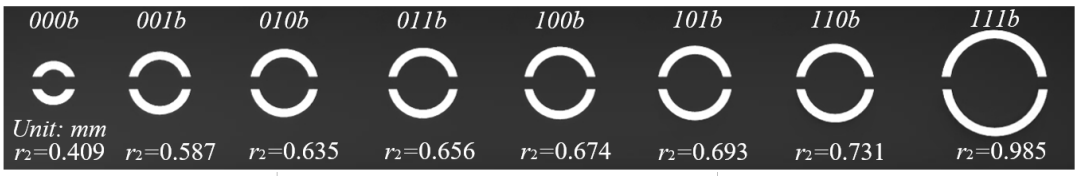

(b)

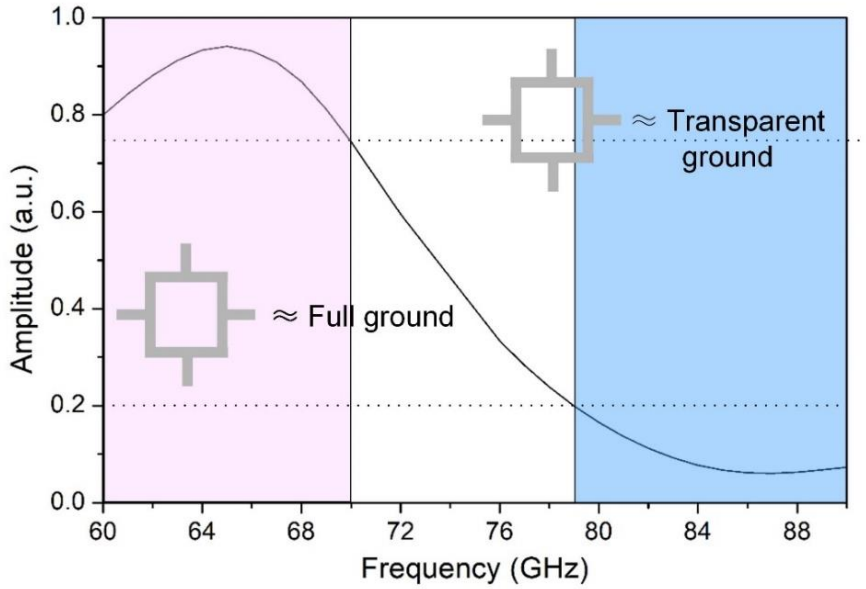

(c)

Fig. 5.4. (a) Configurations of the eight-level cells (3-bit phase quantization) for cell 1 operating at V-band. The lengths of r_1 are decided as 0.39, 0.543, 0.735, 0.811, 0.843, 0.874, 0.916, and 1.037 mm to reach around 45° phase difference to realize 3-bit digital states 000a, 001a, 010a, 011a, 100a, 101a, 110a, and 111a, respectively. (b) Configurations of the eight-level cells (3-bit phase quantization) for cell 2 operating at the W-band. The lengths of r_2 are 0.409, 0.587, 0.635, 0.656, 0.674, 0.693, 0.731, and 0.985 mm to reach around 45° phase difference. This can realize 3-bit digital states 000b, 001b, 010b, 011b, 100b, 101b, 110b, and 111b, respectively. (c) Simulated reflection amplitude of the proposed FSS structure.

To manipulate the wavefront of EM waves, a 2π phase modulation is needed. Therefore, two series of eight-level cells (3-bit phase quantization) for V- and W-bands (cell 1 and cell 2) are designed to implement the dual broadband metasurface. As shown in Figs. 5.4(a) and (b). The lengths of r_1 are decided as 0.39, 0.543, 0.735, 0.811, 0.843, 0.874, 0.916, and 1.037 mm to reach around 45° phase difference, which can realize 3-bit digital states 000a, 001a, 010a, 011a, 100a, 101a, 110a, and 111a, respectively. Similarly, the lengths of r_2 are 0.409, 0.587, 0.635, 0.656, 0.674, 0.693, 0.731, and 0.985 mm to reach around 45° phase difference. This can realize 3-bit digital states 000b, 001b, 010b, 011b, 100b, 101b, 110b, and 111b, respectively. Because of the FSS structure, mutual coupling between these two series of 3-bit cells in different bands can be inhibited. As shown in Fig. 5.4(c), the FSS has two functions in the proposed meta-atom. Firstly, when the meta-atom is operating at V-band from 60 - 70 GHz, the FSS on the second layer is to serve as the ground plane for cell 1 with the simulated reflection amplitude responses higher than 0.75. Secondly, and on the other hand, when the meta-atom operates at the W-band from 79 - 90 GHz, the FSS should be transparent for cell 2 with the simulated reflection amplitude responses lower than 0.2. Thus, the FSS functions well for the dual-band reflectarray design.

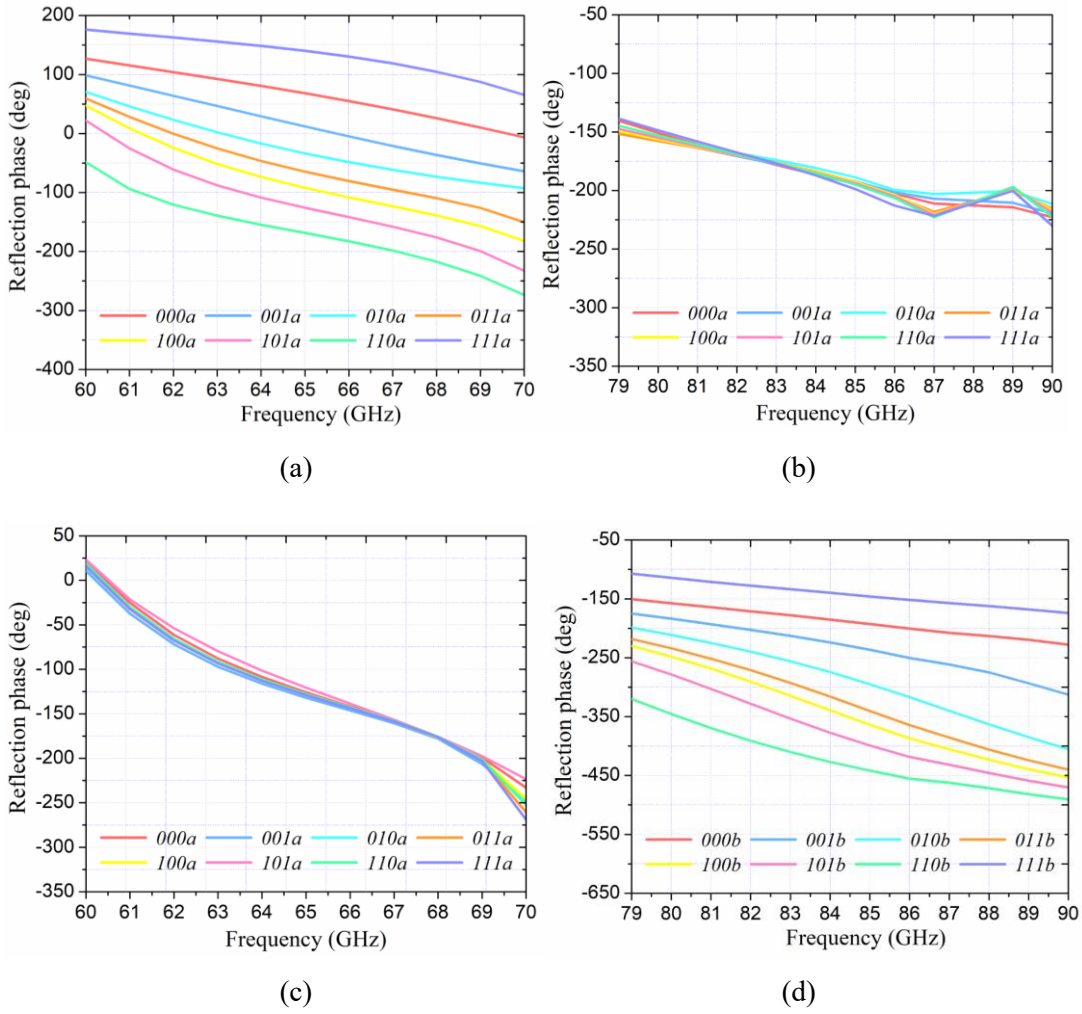

Fig. 5.5. (a) Transmission phase for cell 1 of 3-bit digital states 000a, 001a, 010a, 011a, 100a, 101a, 110a, and 111a from 60-70 GHz, while cell 2 remains constant. (b) Transmission phase for cell 1 of 3-bit digital states 000a, 001a, 010a, 011a, 100a, 101a, 110a, and 111a from 79-90 GHz, while cell 2 keeps constant. (c) Transmission phase for cell 2 of 3-bit digital states 000b, 001b, 010b, 011b, 100b, 101b, 110b, and 111b from 60-70 GHz, while cell 1 keeps constant. (d) Transmission phase for cell 2 of 3-bit digital states 000b, 001b, 010b, 011b, 100b, 101b, 110b, and 111b from 79-90 GHz, while cell 1 remains constant.

Figs. 5.5(a)-(d) reveal the reflection phases delay of the meta-atoms with different 3-bit coding cells**.** In Figs. 5.5(a) and (b), when r_2 is constant, the 3-bit coding cells for cell 1 can cover the 2π range during the lower band from 60-70 GHz while remaining virtually unchanged during the higher band from 79-90 GHz. Meanwhile, in Figs. 5.5(c) and (d), the situation is contrary. When r_1 keeps constant, the 3-bit

coding cells for cell 2 can cover the 2π range during the entire higher- band from 79-90 GHz while keeping steady during the lower band from 60-70 GHz. The phase difference of adjacent coding states for cell 1 and cell 2 are almost 45° during their operational frequency band, proving good phase control performance of the designed coding cells. Therefore, phase delays of the reflection for the lower and higher- bands can be independently controlled by changing the lengths of r_1 and r_2, respectively.

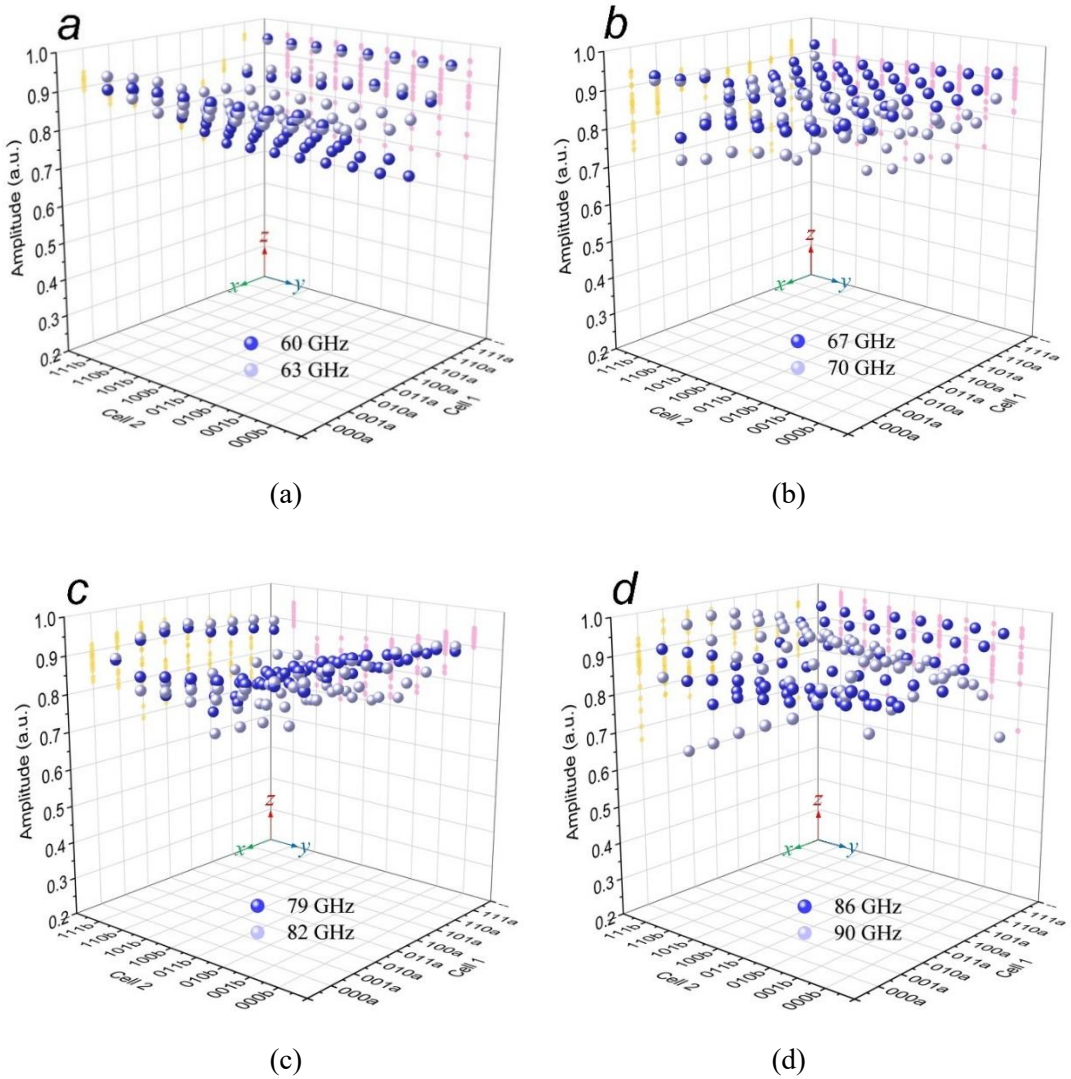

(a) (b)

(c) (d)

Fig. 5.6. Transmission magnitudes of the 3-bit digital states for cell 1: 000a, 001a, 010a, 011a, 100a, 101a, 110a, and 111a and the 3-bit digital states for cell 2: 000b, 001b, 010b, 011b, 100b, 101b, 110b, and 111b with all possible combinations at V-band of (a) 60 and 63 GHz (magnitudes between 0.68 and 0.97), (b) 67 and 70 GHz (magnitudes between 0.63 and 0.95). Transmission magnitudes of the 3-bit digital states for cell 1: 000a, 001a, 010a, 011a, 100a,

101a, 110a, and 111a and the 3-bit digital states for cell 2: 000b, 001b, 010b, 011b, 100b, 101b, 110b, and 111b with all possible combinations at W-band of (c) 79 GHz, 82GHz (magnitudes between 0.69 and 0.96), d) 86 GHz, 90 GHz (magnitudes between 0.67 and 0.98).

In terms of transmission magnitudes of the proposed meta-atom, coding cells of cells 1 and 2 contribute to it simultaneously. Figs. 5.6(a) and (b) show the transmission magnitudes of arbitrary combinations of cells 1 and 2 at the lower band from 60-70 GHz. The projection of every point on the *xoy*-plane represents different combination methods of cells 1 and 2 (e.g., 000a & 000b or 000a & 001b, etc.). As well the projection of every point in the *z*-axis direction represents its transmission magnitudes. To show the values more clearly, the transmission magnitude of every point is projected to the *xoz*- and *yoz*- planes. For example, taking 60 GHz, 63 GHz, 67 GHz, and 70 GHz, the magnitudes of the meta-atoms are between 0.65 and 0.97 at V-band. Fig. 5.6(c) and (d) show the transmission magnitudes at the higher band from 79-90 GHz. For example, taking 79 GHz, 82 GHz, 86 GHz, and 90GHz, the magnitude of the meta-atoms are between 0.7 and 0.98 at W-band. Fig. 5.6 demonstrates the high transmission efficiency at the lower and higher frequency band. It is worth noting that the loss tangent of the printed dielectric material used by the metasurface is 0.013, which is relatively lossy. Thus, a portion of the energy is dissipated into the dielectric material. Assuming the dielectric material has no loss, the transmission magnitudes can be improved by around 0.13 on average.

In conclusion, the design details of the reflective metasurface are performed with the following five steps:

a. Firstly, a coding cell operation at V band from 60-70GHz is designed and optimized. Making sure that a continuous phase variation that covers 2π is realized by tuning a specific parameter and eight-level cells (3-bit phase quantization) for V- band are designed to reach around 45° phase difference realizing 2π phase modulation.
b. Secondly, a coding cell operation at W-band from 79-90GHz is designed and optimized as the same way. 3-bit phase quantization for W- band that has around

45° phase difference between each cell is defined as well.

c. Thirdly, a FSS structure is designed to inhibited mutual coupling between these two series of 3-bit phase quantization in different bands.
d. Fourthly, coding compensating phase at the metasurface apertures for V- and W-bands by using MATLAB, respectively. Then, they can be discretized by using the two series of 3-bit coding cells, respectively.
e. Finally, combing two series of 3-bit coding cells and the FSS structure together to construct the meta-atom for the reflective metasurface, and ensure the reflective magnitude of each meta-atom is higher than 0.7 during the operational frequency range by optimizing the interlayer distance.

5.4 Reflective Metasurface for the Pencil Beam Generation in Two Operational Bands

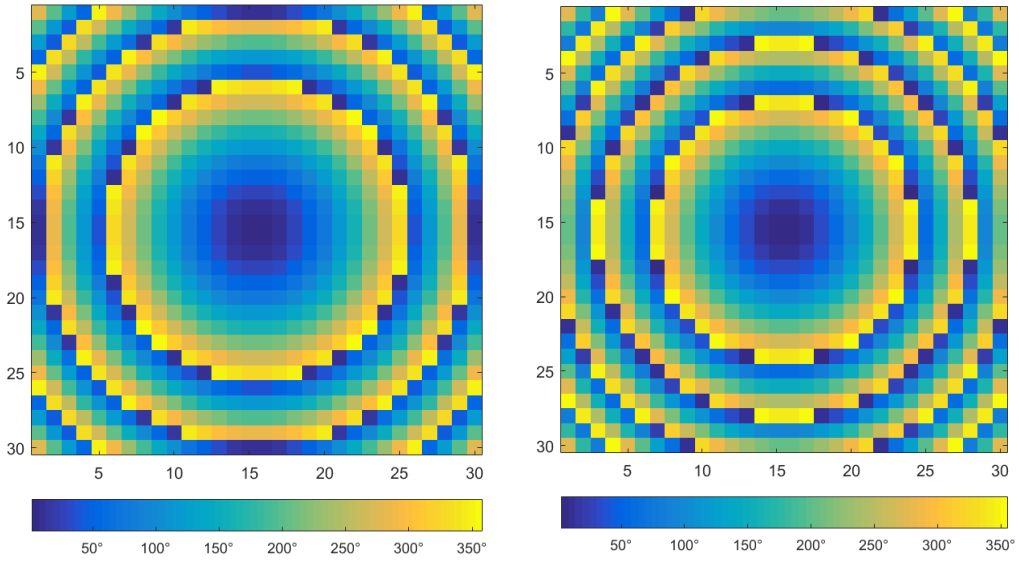

(a) (b)

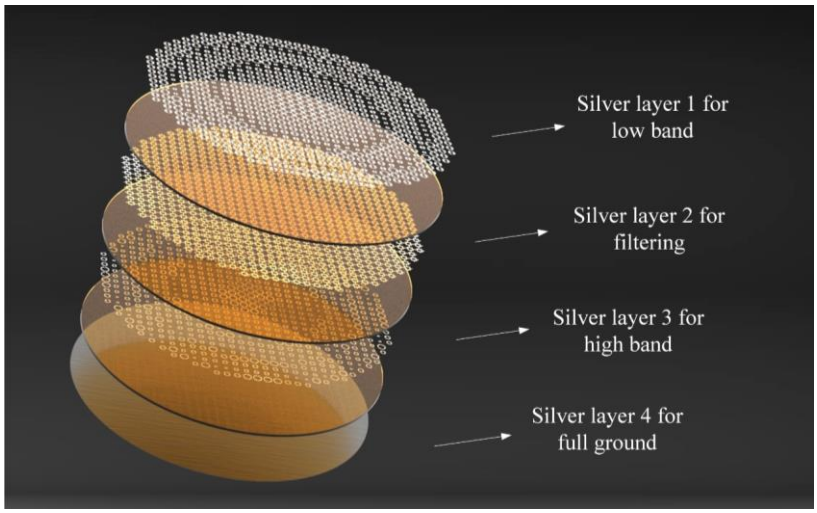

(c)

Fig. 5.7 (a) Compensating phase distribution at the metasurface aperture for layer 1 to generate pencil beam operating at V-band, (b) Compensating phase distribution at the metasurface aperture for layer 1 to generate pencil beam operating at W-band, and (c) Construction of the dual-band metasurface for generating pencil beams.

To verify the effectiveness of the proposed FSS, a finite element electromagnetic

field simulation analysis software, ANSYS High-Frequency Structure Simulator (HFSS), is introduced to conduct a set of full-wave simulations of the proposed metasurface to generate a pencil beam. The aperture for numerical simulation and the feeding waveguide are set as the same as the OAM setting. To mitigate the feed blockage, the feeding waveguide is center-fed and shifted to 15°. By coding cell 1 and cell 2 according to equations (1) and (2), two independent pencil beams operating at 60-70 GHz and 79-90 GHz are generated separately. Figs. 5.7(a) and (b) show the compensating phase at the apertures for layer 1 and layer 3, respectively. Every pixel on these distribution maps represents the required compensating phase delay for the coding cell at this location. 30 × 30 coding cells are included in each map. MATLAB generates the compensating phase distribution maps. Fig. 5.7(c) shows the construction of the dual-band metasurface for generating pencil beams. Then, the reflective metasurface with the entire configuration, including the FSS (4 silver layers) and the one without the FSS (3 silver layers), are simulated and analyzed.

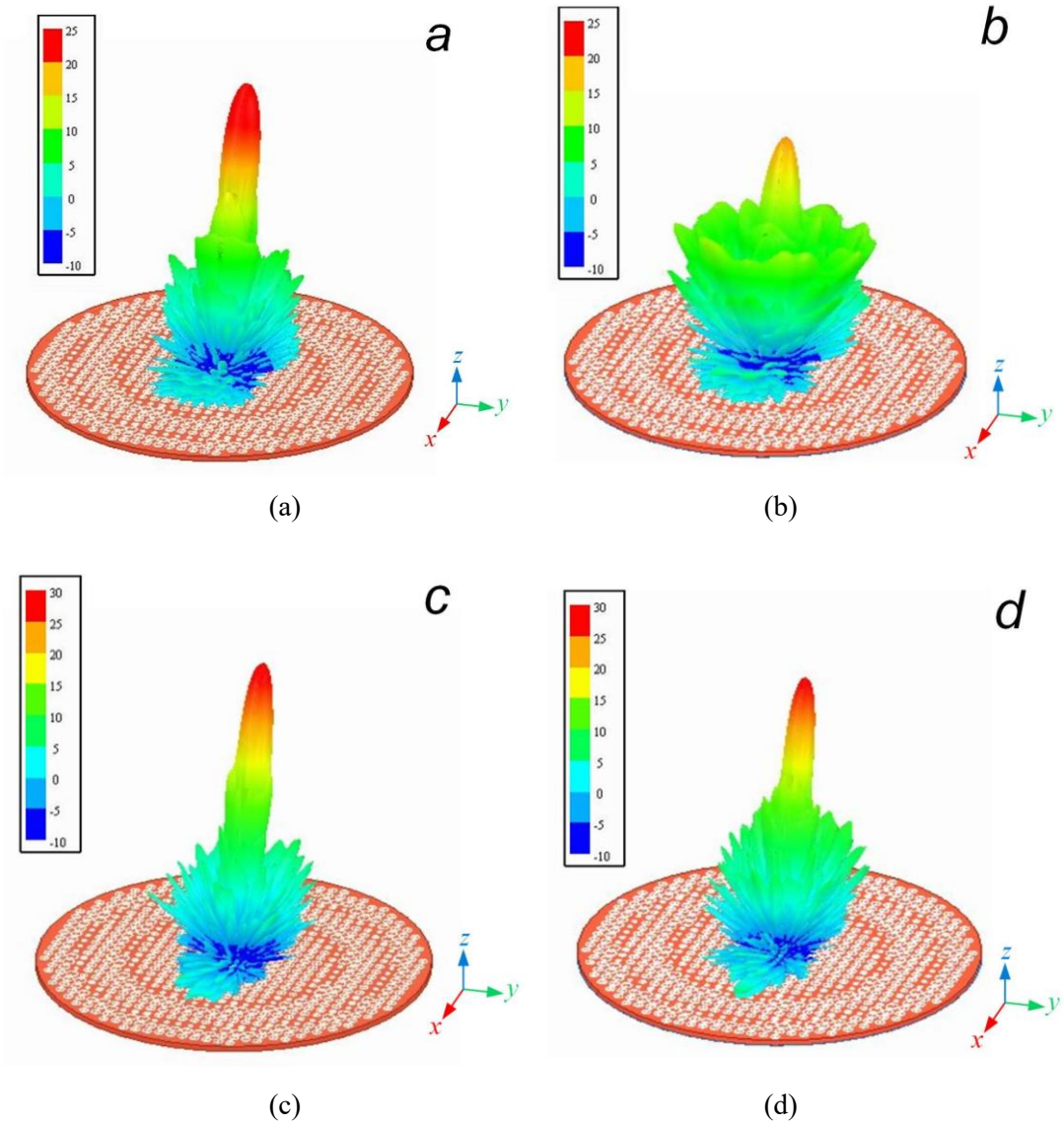

(a) (b)

(c) (d)

Fig. 5.8 (a) Simulated 3D radiation patterns at 64 GHz with the FSS serve as the ground plane for cell 1 under a feeding waveguide center-fed and shifted to 15° (b) Simulated 3D radiation patterns at 64 GHz without FSS under a feeding waveguide center-fed and shifted to 15°. (c) Simulated 3D radiation patterns at 82 GHz with the FSS transparent for cell 2 under a feeding waveguide center-fed and shifted by 15°. (d) Simulated 3D radiation patterns at 82 GHz without FSS under a feeding waveguide center-fed and shifted by 15°.

As shown in Fig. 5.8, the simulated 3D radiation patterns with/without FSS are depicted. Since the FSS serves as the ground plane for cell 1 at V-band from 60 - 70 GHz, as shown in Figs. 5.8(a) and (b), the effect of FSS on the radiation performance at the V-band (taking 64 GHz as an example) is significantly decreased from 24.9

to16.4 dBi by removing FSS. However, the FSS is transparent for cell 2 at W-band from 79 - 90 GHz. As shown in Figs. 5.8(c) and (d), the effect of FSS on the radiation performance at the higher band (taking 82 GHz as an example) drops slightly from 26.4 GHz to 24.8 GHz. Based on these results, we demonstrate the effectiveness of the FSS in improving the gain and efficiency of the dual-band metasurface successfully.

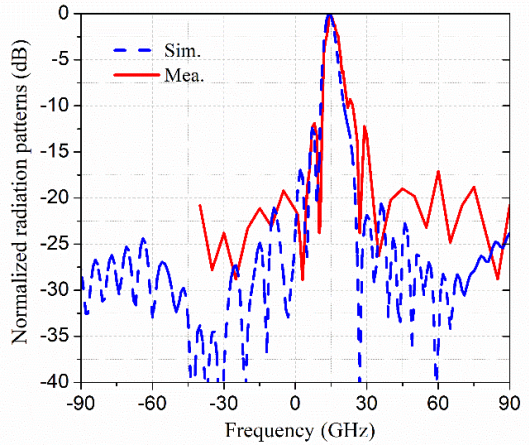

(a)

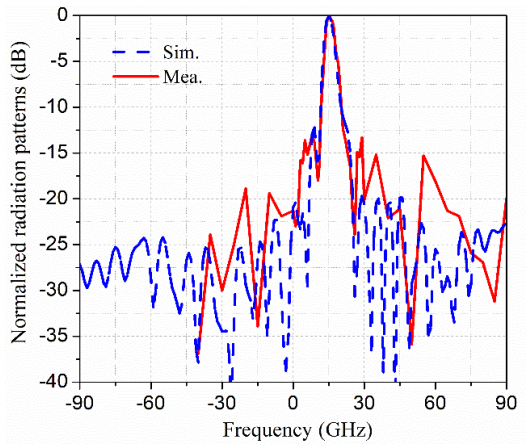

(b)

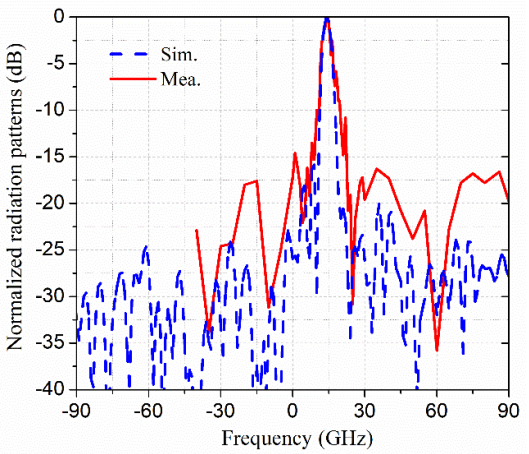

(a)

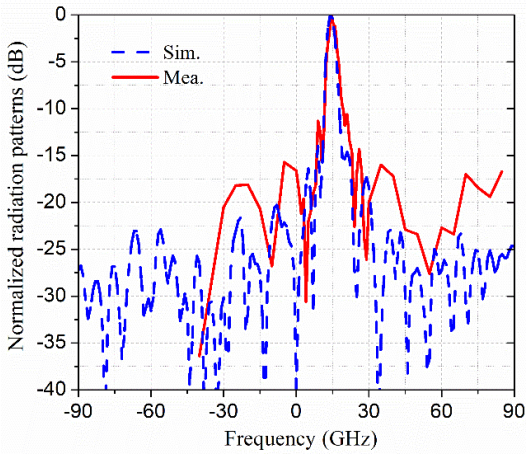

(b)

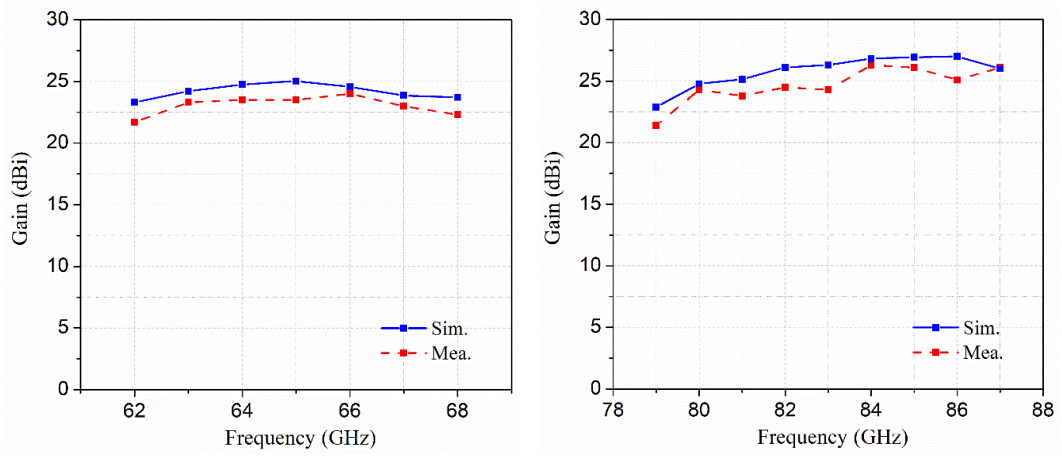

Fig. 5.9. Simulated and measured radiation patterns of pencil beams on the xoz-plane at (a) 64 GHz, (b) 67 GHz, (c) 82 GHz, and (d) 86 GHz. (e) Simulated and measured gains of pencil beams at the V- band from 62-68 GHz and (f) Simulated and measured gains at the W- band from 79-87 GHz.

Fig.5.8(a) and (c) depicts the simulated 3D radiation patterns of reflective metrasurface with FSS. And its measured and simulated 2D radiation patterns at 64, 67, 82, and 86 GHz are shown in Figs. 5.9(a) to (d). It is observed that the pencil beams with high directivity are obtained at both bands simultaneously, and the sidelobe levels of the beams are kept well below -15 dB. The gains in performance across the dual operational frequency bands are also measured in Figs. 5.9(e) and (f). In the lower band, the simulated gains are from 22.9 to 25.1 dBi, and the measurement gains are from 21.8 to 24.0 dBi from 62 to 68 GHz. In the higher- band, simulated gains are from 22.6 to 27.0 dBi, and the measured gains are from 21.4 to 26.5 dBi from 79 to 86 GHz. The simulated radiation patterns and gains agree well with the measured ones, which verifies that metasurfaces for independent manipulation of dual-band electromagnetic waves can be realized with the proposed meta-atom in this thesis.

5.5 Multifunctional OAM Metasurface

5.5.1 Experimental Verification

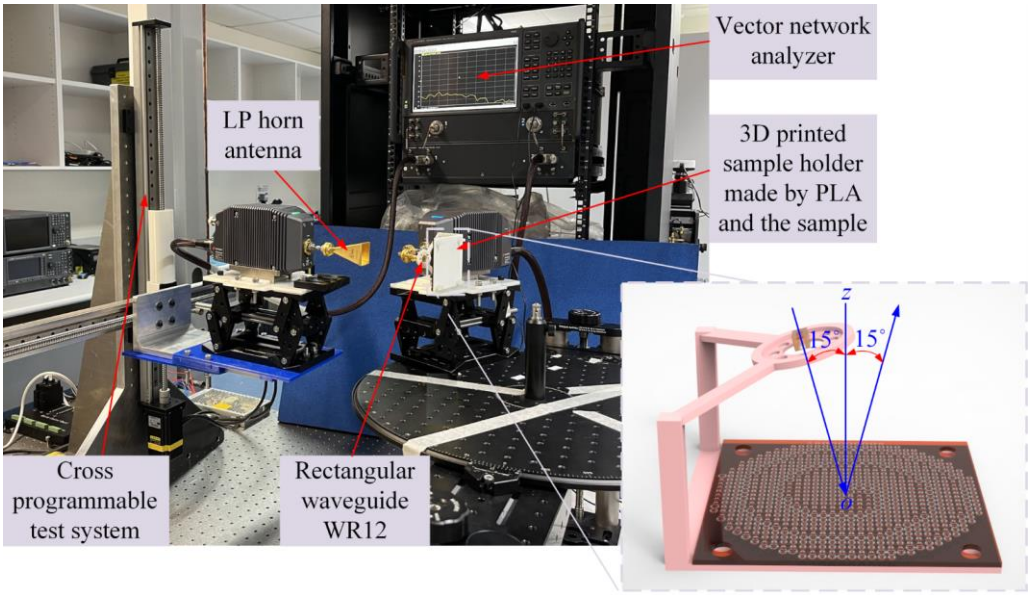

(a)

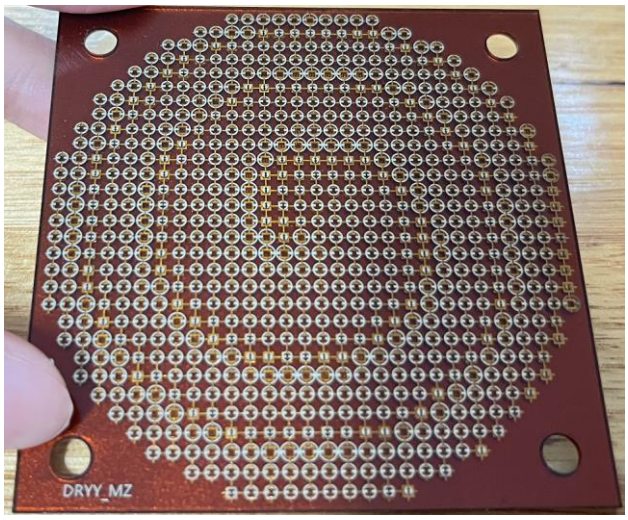

(b)

Fig. 5.10 (a) Experimental setup of the cross-programmable test system for the near-field plane scanning measurement, and (b) the photograph of additively manufactured multi-material metasurface.

We fabricated a sample of the proposed metasurface to experimentally validate

the designed dual-broadband multifunctional metasurfaces with two different OAM states. We measured the performance of vortex beams in different operational frequency bands by a near-field planar scanning technique. Additive manufacturing technology that can fabricate both conductive and dielectric materials is applied to fabricate the metasurface structure in this thesis. This low-cost, time-saving, and flexible 3D printing technology allows four silver and three dielectric layers to be fabricated in a single substrate with an ultra-thin profile (1.235 mm) with a circular-shaped aperture of 70 mm. A specific dielectric material is used in the fabrication process with relative permittivity of 2.8 and a loss tangent of 0.013.

As shown in Fig. 5.10(a), the near-field planar scanning technique is realized by a cross-shaped programmable test system. A rectangular waveguide WR12 is located at the sample's focal point to illuminate the metasurface and shifted by 15˚ to reduce the feed blockage. According to the aperture size and the feeding source, the focal length is defined as 50 mm. Thus, the ratio of focal length to aperture size (i.e., f/D ratio) is 0.7, helping to provide a proper –10 dB edge taper and maximize the aperture efficiency. 3D-printed support inserted in Fig. 10(a) fabricated by polylactic acid (PLA) is designed to ensure the location of the WR12 and the direction of the incident wave are correct. Two motors control the horizontal and vertical movement of the receiving antenna on the near-field plane, respectively. The distance and step of movement can be accurately controlled by programming. The scanning plane is 110 mm away from the sample and parallel to the sample, with an area of 100 mm × 100 mm. The scanning steps along the x and y-directions are set as 3.3 mm. A standard E-band linear polarized (LP) horn antenna is utilized to receive the intensity and phase of the near electric field at each sampled point. Photographs of the proposed additively manufactured multi-material metasurface are shown in Fig. 10(b).

5.5.2 Results Discussion

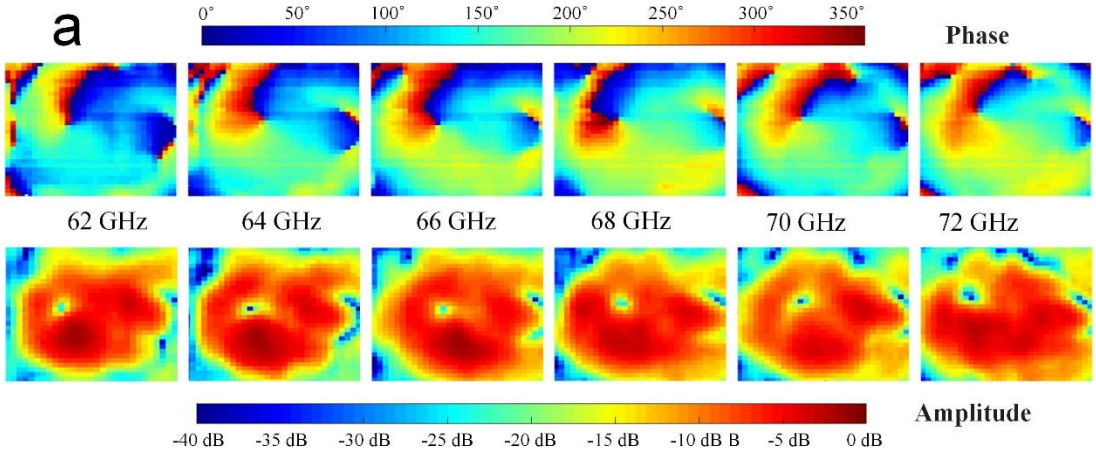

(a)

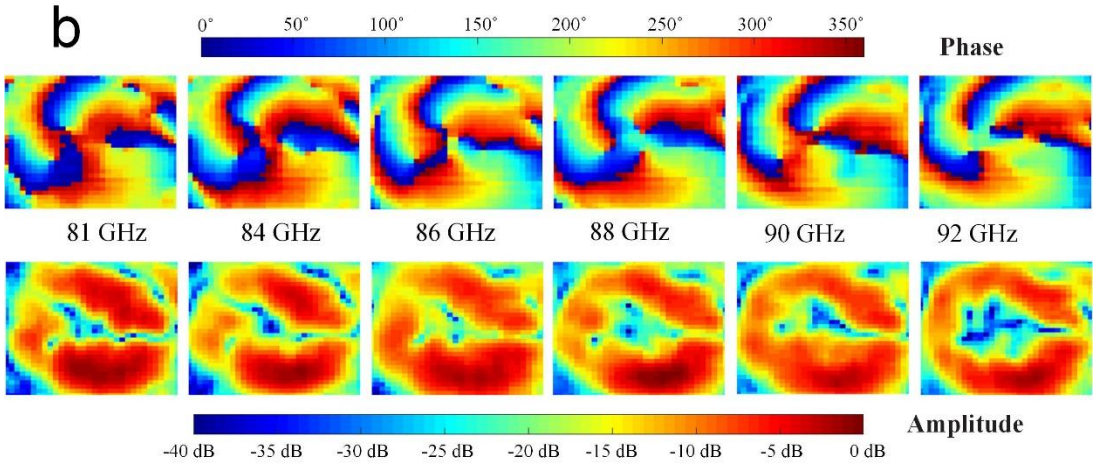

(b)

Fig. 5.11 (a) Measured electric field phase distribution and measured field intensity distribution for the metasurface with an OAM topological charge $l = 1$ at V-band from 62-72 GHz. (b) Measured electric field phase distribution and measured field intensity distribution for the metasurface with an OAM topological charge $l = 3$ at W-band from 81-92 GHz.

Finally, the measured electric field phase and field intensity distribution for the metasurface with different OAM topological charges at two separate operational bands is plotted in Figs. 5.11(a) and (b), respectively. The intensity profiles have doughnut shapes for the lower band, whose operational bandwidth is achieved from 62 GHz to 72 GHz. The spiral phase distributions clearly show vortex beams carrying

OAM with a topological charge of $l = 1$. For the higher- band from 81 GHz to 92 GHz, the intensity profiles have ring shapes, and the spiral phase distributions clearly show vortex beams carrying OAM with a topological charge of $l = 3$. All those measured results verify that the proposed multifunctional OAM metasurface can realize excellent performances of vortex beams with different topological charges of $l = 1$ and $l = 3$ in two operational broadbands, respectively.

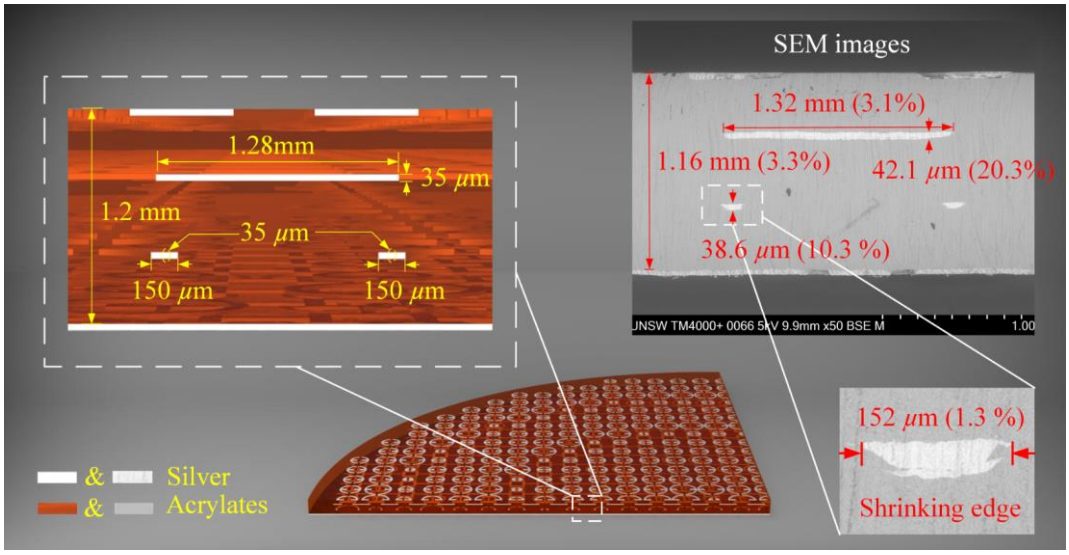

Fig. 5.12. Dimension comparisons of the simulated model and the designed one embedded with a photograph of the printed substrate – cross-section view under an electron microscope.

Compared with the simulated results, the measured results have an error of 2 GHz shift, around 2.9% for the V-band from 62-72 GHz and 2.3% for the W-band from 81-92 GHz, respectively. To pursue the cause of the error, the dimensions of the simulated model and designed one are compared and discussed. In Fig. 5.12, the dimensions of the printed silver traces agree well with the simulated ones on the horizontal plane, whose fabrication errors range from 1.3% to 3.3%. However, in the vertical direction, the thickness of the silver layers is considerably thicker (10 - 20%) than the simulated ones, which may derive from the thickness calibration of the printing system. The thickness of the entire dielectric layer matches well with the designed value. In addition, due to the liquid surface tension of the silver ink during the printing process, most of the silver traces are printed with shrinking edges, which causes the printed

dimensions to be slightly smaller than the target values. In conclusion, the specification of the 3D printing system makes it possible for the machine to meet the demanding design and quality requirements of industries.

5.5.3 Fabrication Process

In this thesis, metasurfaces are fabricated using the conductor and dielectric multi-material-integrated additively manufactured electronics solution. Conductive and dielectric layers are printed using silver nanoparticles and acrylate inks. Each printing head of the 3D printing system comprises 512 piezoelectric-based nozzles connecting to the chambers filled with inks. A 395 nm UV lamp is used to cure acrylate inks through a piezoelectric printing system. For conductive patterns, a 0.75−1.4 μm near-infrared radiation lamp is used for sintering the silver nanoparticle inks with temperatures ranging from 140 to 170 ºC. The multi-material-integrated additive manufacturing process flow chart has been discussed [50]. According to the predesigned patterns, dielectric and conductive inks are printed layer by layer.

5.6. Conclusion

In summary, we have proposed an approach to simultaneously achieve excellent performances of vortex beams with different topological charges of $l = 1$ and $l = 3$ in two operational broadbands with a multifunctional OAM metasurface. In our approach, two series of eight-level (3-bit) coding cells for 2π phase modulation operating at the V-band and W-band are designed to manipulate the EM waves. Due to the FSS structure, mutual coupling between these two series of 3-bit meta-atoms working at different bands can be inhibited. Thus, the dual-frequency metasurface design can be simplified into two single-frequency metasurface designs. Thus, a meta-atom consisting of two series of coding cells, an FSS, and a whole ground, is proposed. Digitalization-coding of meta-atoms is utilized to simplify the design and optimization procedures of the metasurface. In addition, a multi-material conductive

and dielectric additive manufacturing technology is applied to fabricate the models of the proposed metasurface with good advantages of time-saving, low-cost, and flexible designing. Four silver and three dielectric layers of the proposed metasurface can be fabricated in a single substrate with an ultra-thin profile. Finally, an integrated reflective multifunctional metasurface is proposed, fabricated, and measured. Excellent performances of vortex beams with a topological charge of l = 1 are observed from 62-72 GHz (fractional bandwidth is about 14.9%), and vortex beams with a topological charge of l = 3 are observed from 81-92 GHz (fractional bandwidth is about 12.7%). The error of the measured results and fabrication specifications are discussed as well. We believe that the proposed robust methodology with superior performance can improve the information capacity of the coding metasurface on millimeter-wave applications.

5.7 References

[1] J. B. Pendry, D. Schurig, D. R. Smith, “Controlling electromagnetic fields,” *Science,* vol. 312, no. 5781, pp. 1780–1782, June 2006.

[2] D. R. Smith, W. J. Padilla, D. C. Vier, S. C. Nemat-Nasser, S. Schultz,“Composite medium with simultaneously negative permeability and permittivity,”.*Phys. Rev. Lett.,* vol. 84, no. 18, pp. 4184–4191, May 2000.

[3] A. Leitis, A. Heßler, S. Wahl, M. Wuttig, T., Taubner, A. Tittl, H. Altug, “Huygens' Metasurfaces: All-Dielectric Programmable Huygens' Metasurfaces” *Adv. Funct. Mater.,* vol. 30, no. 19, pp. 2070122, May 2020.

[4] C. X. Huang, J. Zhang, Q. Cheng, T. J. Cui, “Polarization modulation for wireless communications based on metasurfaces.” *Adv. Funct. Mater.,* vol. 31, no. 36, pp. 2103379, 2021.

[5] D. S. Dong, J. Yang, Q. Cheng, J. Zhao, L.H. Gao, S.J. Ma, S. Liu, H.B. Chen, Q. He, W.W. Liu, Z. Fang, L. Zhou, and T.J. Cui, “Terahertz broadband low-reflection metasurface by controlling phase distributions,” *Adv. Opt. Mater.,* vol. 3, no. 10, pp. 1405-1410, 2015.

[6] A. V. Kildishev, A. Boltasseva, V. M. Shalaev, "Planar photonics with metasurfaces," *Science,* vol. 339, no. 6125, pp. 1232009, 2013.

[7] P. C. Wu, R. Sokhoyan, G. K. Shirmanesh, W.-H. Cheng, H. A. Atwater, "Near-infrared active metasurface for dynamic polarization conversion," *Adv. Opt. Mater.,* vol. 9, no. 16, pp. 2100230, 2021.

[8] Y. Zheng, Y. Zhou, J. Gao, X. Cao, H. Yang, S. Li, L. Xu, J. Lan, and L. Jidi, "Ultra-wideband polarization conversion metasurface and its application cases for antenna radiation enhancement and scattering suppression," *Sci. Rep.,* vol. 7, no. 1, pp. 1-12, 2017.

[9] L. B. Yan, W. M. Zhu, M. F. Karim, H. Cai, A. Y. D. Gu, Z. X. Shen, P. H. J. Chong, D. P. Tsai, D.-L. Kwong, C.-W. Qiu, A. Q. Liu, "Arbitrary and independent polarization control in situ via a single metasurface," *Adv. Opt. Mater.,* vol. 6, no. 21, pp. 1800728, 2018.

[10] H.-X. Xu, S. Tang, S. Ma, W. Luo, T. Cai, S. Sun, Q. He, L. Zhou, "Tunable microwave metasurfaces for high-performance operations: dispersion compensation and dynamical switch," *Sci. Rep.,* vol. 6, no. 1, pp. 1-10, 2016.

[11] L. B. Yan, W. M. Zhu, P. C. Wu, H. Cai, Y. D. Gu, L. K. Chin, Z. X. Shen, P. H. J. Chong, Z. C. Yang, W. Ser, D. P. Tsai, A. Q. Liu, "Adaptable metasurface for dynamic anomalous reflection," *Appl. Phys. Lett.,* vol. 110, no. 20, pp. 201904, 2017.

[12] C. Huang, C. Zhang, J. Yang, B. Sun, B. Zhao, X. Luo, "Reconfigurable metasurface for multifunctional control of electromagnetic waves," *Adv. Opt. Mater.,* vol. 5, no. 22, pp. 1700485, 2017.

[13] T. Cai, G. M. Wang, X. F. Zhang, J. G. Liang, Y. Q. Zhuang, D. Liu, H. X. Xu, "Ultra-thin polarization beam splitter using 2-D transmissive phase gradient metasurface," *IEEE Trans. Antennas Propag.,* vol. 63, no. 12, pp. 5629-5636, 2015.

[14] B. A. Slovick, Y. Zhou, Z. G. Yu, I. I. Kravchenko, D. P. Briggs, P. Moitra, S. Krishnamurthy, J. Valentine, Philos. "Metasurface polarization splitter," *Trans. R. Soc. A,* vol. 375, no. 2090, pp. 20160072, 2017.

[15] G. W. Ding, K. Chen, G. X. Qian, J. M. Zhao, T. Jiang, Y. J. Feng, Z. B. Wang,

"Independent energy allocation of dual-helical multi-beams with spin-selective transmissive metasurface," *Adv. Opt. Mater.,* vol. 8, no. 16, pp. 2000342, 2020.

[16] F. Qin, L. Ding, L. Zhang, F. Monticone, C. C. Chum, J. Deng, S. Mei, Y. Li, J. Teng, M. Hong, S. Zhang, A. Alù, and C.-W. Qiu, "Hybrid bilayer plasmonic metasurface efficiently manipulates visible light," *Sci. Adv.,* vol. 2, no. 1, pp. e1501168, 2016.

[17] J.-Y. Guo, X.-K. Wang, J.-W. He, H. Zhao, S.-F. Feng, P. Han, J.-S. Ye, W.-F. Sun, G.-H. Situ, Y. Zhang, "Generation of radial polarized Lorentz beam with single layer metasurface," *Adv. Opt. Mater.,* vol. 6, no. 1, pp. 1700925, 2018.

[18] E. Karimi, S. A. Schulz, I. D. leon, H. Qassim, J. Upham, R. W. Boyd, "Generating optical orbital angular momentum at visible wavelengths using a plasmonic metasurface," *Light: Sci. Appl.,* vol. 3, no. 5, pp. e167-e167, 2014.

[19] Q. Ma, C. B. Shi, G. D. Bai, T. Y. Chen, A. Noor, T. J. Cui, "Beam-editing coding metasurfaces based on polarization bit and orbital-angular-momentum-mode bit," *Adv. Opt. Mater.,* vol. 5, no. 23, pp. 1700548, 2017.

[20] S. Li, X. Li, L. Zhang, G. Wang, X. Ling, M. Liu, C. Zeng, L. Wang, Q. Sun, W. Zhao, W. Zhang, "Efficient optical angular momentum manipulation for compact multiplexing and demultiplexing using a dielectric metasurface," *Adv. Opt. Mater.,* vol. 8, no. 8, pp. 1901666, 2020.

[21] B. Liu, Y. He, S.-W. Wong, Y. Li, "Multifunctional vortex beam generation by a dynamic reflective metasurface," *Adv. Opt. Mater.,* vol. 9, no. 4, pp. 2001689, 2021.

[22] N. Yu, F. Capasso, "Flat optics with designer metasurfaces," *Nat. Mater.,* vol. 13, no. 2, pp. 139-150, 2014.

[23] H. Lv, Z. Yang, H. Xu, L. Wang, R. Wu, "An electrical switch-driven flexible electromagnetic absorber.," *Adv. Opt. Mater.,* vol. 30, no. 4, pp. 1907251, 2020.

[24] Y. Li, Z. Liu, H. Zhang, P. Tang, B. Wu, G. Liu, "Ultra-broadband perfect absorber utilizing refractory materials in metal-insulator composite multilayer stacks," *Opt. Express,* vol. 27, no. 8, pp. 11809-11818, 2019.

[25] M. F. Imani, D. R. Smith, del P. Hougne, "Perfect absorption in a disordered

medium with programmable meta-atom inclusions," *Adv. Opt. Mater.,* vol. 30, no. 52, pp. 2005310, 2020.

[26] X. Jiang, H. Yuan, D. B. Chen, Z. J. Zhang, T. Du, H. S. Ma, J. B. Yang, "Metasurface based on inverse design for maximizing solar spectral absorption," *Adv. Opt. Mater.,* vol. 9, no. 19, pp. 2100575, 2021.

[27] P. Xu, H. W. Tian, X. Cai, W. X. Jiang, T. J. Cui, "Radiation-type metasurfaces for advanced electromagnetic manipulation," *Adv. Funct. Mater.,* vol. 31, no. 25, pp. 2100569, 2021.

[28] Q. Xiao, Q. Ma, T. Yan, L. W. Wu, C. Liu, Z. X. Wang, X. Wan, Q. Cheng, T. J. Cui, "Orbital-angular-momentum-encrypted holography based on coding information metasurface," *Adv. Opt. Mater.,* vol. 9, no. 11, pp. 2002155, 2021.

[29] Z. Wang, X. Ding, K. Zhang, B. Ratni, S. N. Burokur, X. Gu, Q. Wu, "Huygens metasurface holograms with the modulation of focal energy distribution," *Adv. Opt. Mater.,* vol. 6, no. 12, pp. 1800121, 2018.

[30] H. Li, Y. B. Li, J. L. Shen, T. J. Cui, "Low-profile electromagnetic holography by using coding fabry–perot type metasurface with in-plane feeding," *Adv. Opt. Mater.,* vol. 8, no. 9, pp. 1902057, 2020.

[31] X. Xie, X. Li, M. Pu, X. Ma, K. Liu, Y. Guo, X. Luo, "Plasmonic metasurfaces for simultaneous thermal infrared invisibility and holographic illusion," *Adv. Funct. Mater.,* vol. 28, no. 14, pp. 1706673, 2018.

[32] N. Destouches, N. Sharma, M. Vangheluwe, N. Dalloz, F. Vocanson, M. Bugnet, M. Hébert, J. Siegel, "Laser-empowered random metasurfaces for white light printed image multiplexing," *Adv. Funct. Mater.,* vol. 31, no. 18, pp. 2010430, 2021.

[33] Y. Yao, W. Wu, "All-dielectric heterogeneous metasurface as an efficient ultra-broadband reflector," *Adv. Opt. Mater.,* vol. 5, no. 14, pp. 1700090, 2017.

[34] Y.B. Li, B.G. Cai, Q. Cheng, and T.J. Cui, "Isotropic holographic metasurfaces for dual-functional radiations without mutual interferences," *Adv. Funct. Mater.,* vol. 26, no. 1, pp. 29-35, 2016.

[35] C. Zhou, W.-B. Lee, C.-S. Park, S. Gao, D.-Y. Choi, S.-S. Lee, "Multifunctional beam manipulation at telecommunication wavelengths enabled by an all-dielectric metasurface doublet," *Adv. Opt. Mater.,* vol. 8, no. 15, pp. 2000645. 2020.

[36] Y. Huang, X. Xie, M. Pu, Y. Guo, M. Xu, X. Ma, X. Li, X. Luo, "Dual-functional metasurface toward giant linear and circular dichroism," *Adv. Opt. Mater.,* vol. 8, no. 11, pp. 1902061. 2020.

[37] D. Wen, J. J. Cadusch, J. Meng, K. B. Crozier, "Multifunctional dielectric metasurfaces consisting of color holograms encoded into color printed images," *Adv. Funct. Mater.,* vol. 30, no. 3, pp. 1906415, 2020.

[38] H. L. Wang, H. F. Ma, M. Chen, S. Sun, T. J. Cui, "A reconfigurable multifunctional metasurface for full-space control of electromagnetic waves," *Adv. Funct. Mater.,* vol. 31, no. 25, pp. 2100275, 2021.

[39] G. D. Bai, Q. Ma, S. Iqbal, L. Bao, H. B. Jing, L. Zhang, H. T. Wu, R. Y. Wu, H. C. Zhang, C. Yang, T. J. Cui, "Multitasking shared aperture enabled with multiband digital coding metasurface," *Adv. Opt. Mater.,* vol. 6, no. 21, pp. 1800657. 2018.

[40] Z. Zhang, J. Wang, M. Pu, X. Ma, C. Huang, Y. Guo, X. Luo, "Broadband achromatic transmission–reflection-integrated metasurface based on frequency multiplexing and dispersion engineering," *Adv. Opt. Mater.,* vol. 9, no. 7, pp. 2001736, 2021.

[41] L. Zhang, R. Y. Wu, G. D. Bai, H. T. Wu, Q. Ma, X. Q. Chen, T. J. Cui, "Transmission-reflection-integrated multifunctional coding metasurface for full-space controls of electromagnetic waves," *Adv. Funct. Mater.,* vol. 28, no. 33, pp. 1802205, 2018.

[42] T. J. Cui, M. Q. Qi, X. Wan, J. Zhao, Q. Cheng, "Coding metamaterials, digital metamaterials and programmable metamaterials," *Light: Sci. Appl.,* vol. 3, no. 10, pp. e218-e218, 2014.

[43] X. Wan, J. W. Wang, Z. A. Huang, B. Y. Li, Q. Xiao, T. J. Cui, "Space–time–frequency modulation mechanisms of monochromatic and nonmonochromatic electromagnetic waves on a digital programmable transmission metasurface," *Adv.*

Funct. Mater., vol. 32, no. 13, pp. 2107557, 2022.

[44] V. M. Pepino, A. F. da Mota, A. Martins and B. V. Borges, "A 3-D-printed W-band slotted waveguide array antenna optimized using machine learning," *IEEE Antennas Wireless Propag. Lett.,* vol. 17, no. 11, pp. 2008-2012, 2018.

[45] H. P. Li, G.-M. Wang, G. W. Hu, T. Cai, C.-W. Qiu, H.-X. Xu, "3D-printed curved metasurface with multifunctional wavefronts," *Adv. Opt. Mater.,* vol. 8, no. 15, pp. 2000129, 2020.

[46] X. Dong, J. Cheng, Y. Yuan, F. Fan, X. Wang and S. Chang, "An efficient bi-functional metagrating via asymmetric diffraction of terahertz beams," *IEEE Photon. Technol. Lett.,* vol. 33, no. 9, pp. 441-444, 2021.

[47] P. Xie, G. Wang, "An efficient bi-functional metagrating via asymmetric diffraction of terahertz beams," *Int. J. RF Microw. Comput. Aided Eng.,* vol. 31, no. 6, pp. e22657, 2021.

[48] A. Lalbakhsh, M.U. Afzal, T. Hayat, K. P. Esselle, and K. Mandal. "All-metal wideband metasurface for near-field transformation of medium-to-high gain electromagnetic sources," *Sci. Rep.,* vol. 11, no. 1, pp. 1-9. 2021

[49] H. Ren, X. Fang, J. Jang, J. Bürger, J. Rho, and S. A. Maier, "Complex-amplitude metasurface-based orbital angular momentum holography in momentum space," *Nat. Nanotechnol.,* vol. 15, no. 11, pp. 948–955. 2020.

[50] J. Zhu, Y. Yang, N. Hu, S. Liao, and J. Nulman, "Additively manufactured multi-material ultrathin metasurfaces for broadband circular polarization decoupled beams and orbital angular momentum generation," *ACS Appl. Mater. Interfaces,* vol. 13, no. 49, pp. 59460-59470. 2021.

[51] P. Nayeri, F. Yang, and A. Z. Elsherbeni, *Reflectarray Antennas*: *Theory, Designs, and Applications.* Wiley, Hoboken, NJ, USA: 2018.

Chapter 6 Conclusion and Future Work

6.1 Conclusion

Additive manufacturing technology is knocking on the door, ready to change our life. Many complex constructions, which are difficult to implement by means of conventional methods, can be prototyped and realized by 3D printing technology. In the field of electronic devices for microwave and millimeter-wave applications, the fifth-generation (5G) wireless system rollout has driven revolutionary fabrication methods that can construct electronics with high accuracy, low cost, and require only a short production circle.

Chapter 1 first introduces the details of multi-material integrated additively manufactured electronics solution, which plays an essential role in the fabrication of the designs.

Chapter 2 focuses on state-of-the-art works - from single-material to multi-material additive manufacturing technology, which introduces a background of the additive manufacturing technology based on the different types and amounts of materials used in the printing system. This introduction helps readers to understand the context or background of additive manufacturing technology. The relevant content entitled “Multi-material additive manufacturing - a further step from microwave to terahertz regime” has been accepted in *IEEE Microwave Magazine*.

Chapter 3 demonstrates a 3D-Printed low-profile single-substrate multi-metal layer antennas and array, where a surface-driven patch and embedded stacked patch are co-designed. A bandwidth improvement thanks to multi-mode stacked patches can be achieved, taking advantage of the three-dimensional design capability without requiring an additional substrate or affecting the in-plane dimensions of the prototype. After that, multi-layer CP antennas, as well as LP and CP antenna arrays, are designed and fabricated. Successfully devising multi-layer patch antennas proves that the AME solution can serve as a revolutionary approach to the increasing number of 5G consumer mobile electronics. The related content entitled “3D-printed low-profile single-

substrate multi-metal layer antennas and array with bandwidth enhancement" has been submitted to *IEEE Access*.

Chapter 4 focuses on 3D-printed multi-layer compact devices, including transmission lines, bandpass filters, and couplers. First, an additively manufactured bandpass filter (BPF) based on a second-order stub-loaded resonator consisting of multi-metal layer components is proposed. By reducing the interlayer distance, constant inductance and capacitance can be realized in smaller sizes, which helps to achieve device minimization. For verification, the frequency response of the circuit's mathematical model is calculated to compare with the electromagnetic simulation results. The related content entitled "Compact multi-layer bandpass filter using low-temperature additive manufacturing solution" has been published in *IEEE Transactions on Electron Devices*. Next, we proposed a novel compact vertically integrated multi-layer composite right/left-handed (CRLH) transmission line with good performance, including low loss and wide operational band. Vertically integrated multi-layer BPF and coupler are proposed based on the CRLH transmission line structure as well. The odd- and even-mode method is suggested to deduce the resonance properties of the three-dimension CRLH resonator due to its symmetrical construction. The related content entitled "Vertically integrated multi-layer composite right/ left-handed broadband devices using additively manufactured electronics solution" is being submitted to *IEEE Transactions on Microwave Theory and Techniques*.

Chapter 5 proposed a broadband coding metasurface to realize two different orbital angular momentum (OAM) states at V-band and W-band, respectively, for high-speed wireless communications. The metasurface is 3D-printed with silver nanoparticle and ultraviolet (UV) curable acrylates inks, which can generate two OAM beams with independently manipulated wavefronts, operating at 62-72 GHz and 81-92 GHz. The construction of the dual-band metasurface is organized in four different silver layers but fabricated in a single substrate with the merit of an ultra-thin planar profile. Furthermore, we design and fabricate a reflective metasurface for the pencil beam generation in two operational bands to verify the independent manipulation of the electromagnetic wavefronts to implement different functional devices. The proposed

metasurfaces can find applications in next-generation wireless communications. The related content has been submitted as a journal paper titled “3D printed multi-material conductive and dielectric metasurfaces for independent manipulation of broadband orbital angular momentum”. It is being submitted to *ACS Applied Materials & Interfaces*.

6.2 Future Work

The designs and principles demonstrated in the dissertation exhibit good performance by taking advantage of the novel AME solution. Multi-layer fabrication capability and strict tolerance and resolution enable the fabrication of devices scaled to higher frequencies. Thus, more studies and designs covered in this dissertation may be worthy of further investigation.

1. New mm-wave and THz beam shaping devices using integrated additively manufactured electronics (AME) technique. In Chapter 5, a broadband coding metasurface to realize two different OAM states at V-band and W-band, respectively, are fabricated using AME solution. Since the operational frequency bands have been very close to the THz, designing devices with smaller dimensions would be interesting. In addition, four metal layers have been introduced in the design of the reflectarray. Maybe more layers can be used in the future to realize more advanced functions.

2. Multi-layer composite right/ left-handed devices. Reducing the energy loss of the signal during the propagation is always significant for electronics design. Especially for the AME solution, it is a challenge to reduce the energy loss with a high loss tangent of 0.013. Therefore, the multi-layer composite right/ left-handed structure can be a good approach to designing devices with low loss and deserves considerable attention in future work. For example, a 3-dB CRLH coupler based on the vertically integrated CRLH structure is under investigation. It consists of two vertically integrated CRLH transmission lines located at the top and bottom sides of the substrate. Seven metal layers are utilized to fabricate the structure. The proposed vertically integrated CRLH structure has unique electromagnetic properties. It reveals negative permittivity and

negative permeability. In addition, due to the symmetrical structure of the proposed coupler, an outstanding magnitude and 90-degree phase balance can be observed in a wide fractional bandwidth and wide 15-dB matching bandwidth.

3. More compact multilayer microwave devices such as power dividers, baluns, diplexers, and delay lines. Based on the above research, we demonstrate the methods using up-raised ground connected to the RF ground by vias to adjust the impedance matching, using broadside coupling to replace edge coupling for stronger coupling capacitance with smaller size; and using the testing accessories to reduce the soldering and measurement errors. All these strategies can be applied to design compact multilayer microwave devices. The novel AME technique provides the designers with greater flexibility and a shorter product cycle.

Publications

Journal papers：

[1] **M. Li,** Y. Yang, L. Deng, X. He, F. Iacopi and J. Nulman, "3D printed multi-material conductive and dielectric metasurfaces for independent manipulation of broadband orbital angular momentum," *ACS Applied Materials & Interfaces.,* in submitting.

[2] M. Li, Y. Yang, F. Iacopi, M. Yamada, Y. Zhang, and J. Nulman, "Vertically integrated multi-layer composite right/ left-handed broadband devices using additively manufactured electronics solution," *IEEE Transactions on Microwave Theory and Techniques,* in submitting.

[3] **M. Li,** Y. Yang, "Multi-material additive manufacturing - a further step from microwave to terahertz regime," *IEEE Microwave Magazine*, vol. 24, no. 1, pp. 30-45, Jan. 2023.

[4] **M. Li**, Y. Yang, F. Iacopi, M. Yamada and J. Nulman, "Compact multilayer bandpass filter using low-temperature additive manufacturing solution," *IEEE Transactions on Electron Devices,* vol. 68, no. 7, pp. 3163-3169, July 2021. (**Published as journal front cover artwork**)

[5] **M. Li,** Y. Yang, F. Iacopi, J. Nulman and S. Chappel-Ram, "3D-printed low-profile single-substrate multi-metal layer antennas and array with bandwidth enhancement," *IEEE Access,* vol. 8, pp. 217370-217379, 2020.

Conference papers：

[1] **M. Li,** Y. Yang, Y. F. Iacopi and J. Nulman, "Additively manufactured multi-layer bandpass filter based on vertically integrated composite right and left handed resonator," *2021 IEEE Asia-Pacific Microwave Conference (APMC),* 2021, pp. 175-177, doi:

10.1109/APMC52720.2021.9661654.

[2] **M. Li**, Y. Yang, Y. Zhang, F. Iacopi, S. Ram and J. Nulman, "A fully integrated conductive and dielectric additive manufacturing technology for microwave circuits and antennas," *50th European Microwave Conference (EuMC),* Utrecht, Netherlands, 2021, pp. 392-395, doi: 10.23919/EuMC48046.2021.9338141.

[3] **M. Li,** Y. Yang, F. Iacopi and J. Nulman, "3D printed multilayer bandpass filter using additively manufactured electronics (AME) technology," *The 17th Australasian Symposium on Antennas*, accepted, February 2021.

[4] **M. Li,** Y. Yang, F. Iacopi and J. Nulman, "3D-printed single-substrate low-profile multi-metal layer antenna with bandwidth enhancement using fully-integrated dielectric and conductive inks," *The 17th Australasian Symposium on Antennas,* accepted February 2021.